Study of the Superconducting Medium Beta Cavity of the European Spallation Source

Pirani, Saeid

2020

Document Version:
Publisher's PDF, also known as Version of record

Study of the Superconducting Medium Beta Cavity of the European Spallation Source

SAEID PIRANI
DEPARTMENT OF PHYSICS | LUND UNIVERSITY

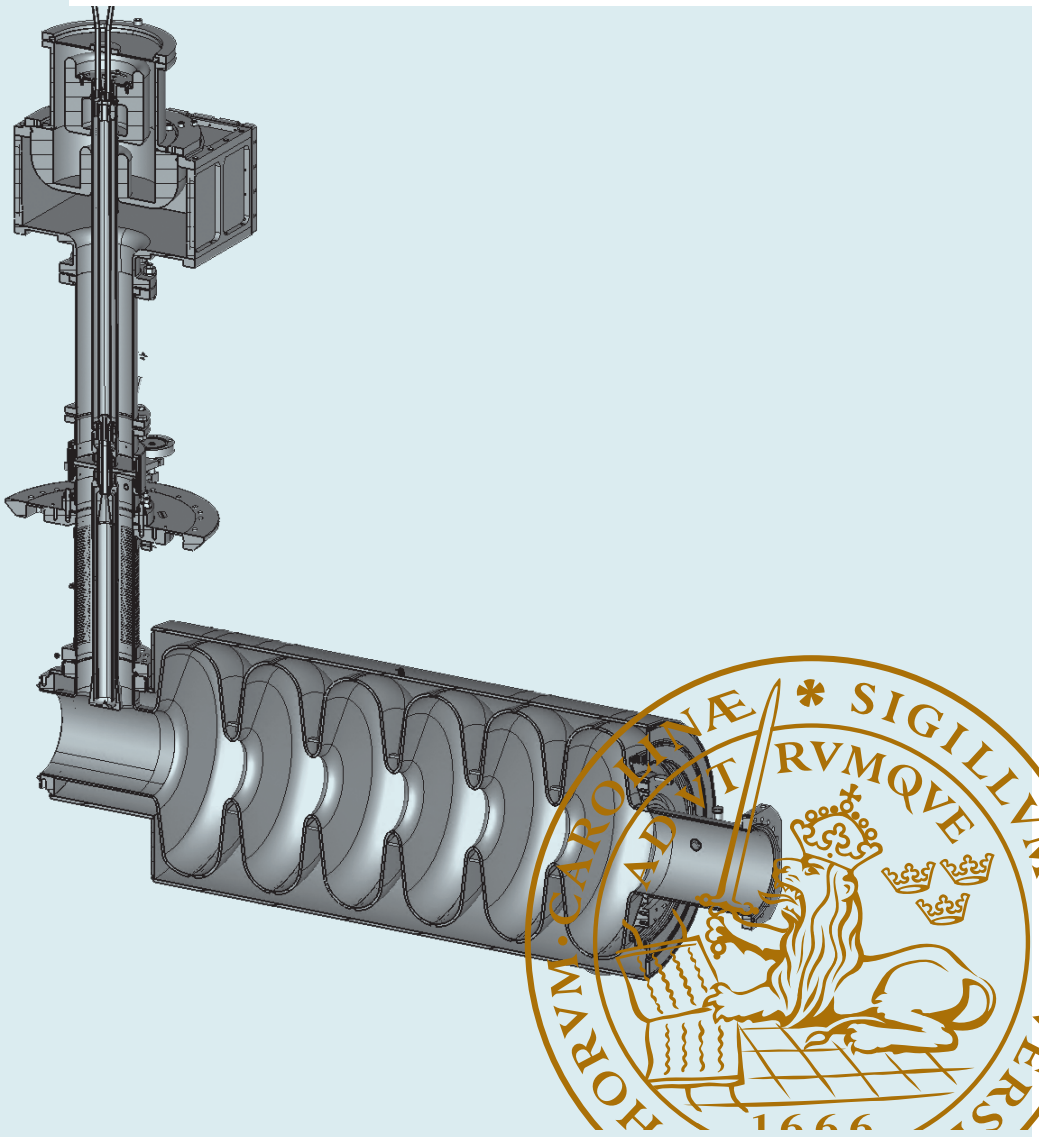

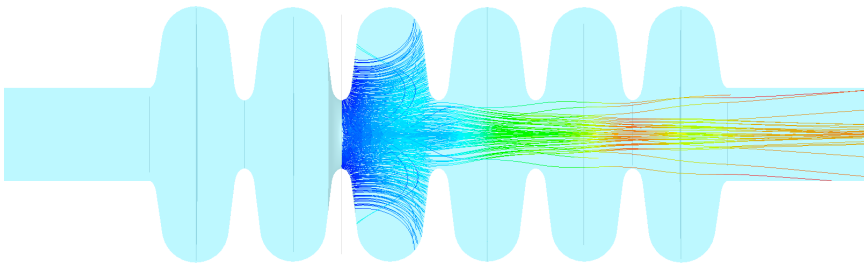

Printed by Media-Tryck, Lund 2020 NORDIC SWAN ECOLABEL 3041 0903

LUND UNIVERSITY

Department of Physics
Particle Physics

ISBN 978-91-7895-456-8

9 789178 954568

Study of the Superconducting Medium Beta Cavity of the European Spallation Source

Saeid Pirani

LUND
UNIVERSITY

Faculty of Science
Department of Physics
Particle Physics

ISBN 978-91-7895-456-8 (print)
ISSN 978-91-7895-457-5 (pdf)

Printed in Sweden by Media-Tryck, Lund
University Lund 2020

Dedication

I am grateful to the kind support of my beloved wife, Ashrafi. It would not be possible to finish this PhD without her support.

I am grateful to my supervisors, Mats Lindroos, Mohammad Eshraqi, Paolo Michelato and Torsten Akesson for their valuable advice and support during my PhD studies.

I am also grateful for the financial support of ESS for this PhD. Many thanks for the support from all the staff at ESS and INFN-LASA.

Particular thanks go to Angelo Bosotti and Paolo Pierini for all their valuable technical advice.

Thanks to JinFang Chen and Michele Bertucci for their valuable consultation.

Table of Contents

Popular summary

The ESS linear accelerator (ESS linac) uses superconducting cavities to accelerate more than 10 peta-protons from 40% to 95% of the speed of light, which is 95% of the total energy gain of the ESS linear accelerator.

One of the advantages of the superconducting cavities over normal conducting cavities is that they deliver practically all the power to the beam, and no power is wasted in the form of heat. However, the design, fabrication, cleaning, testing and operation of such cavities are a broad field of studies due to their sensitivities.

In this thesis the focus is on explaining the design, fabrication, vertical test, higher order mode (HOM) and field emission study of the ESS superconducting medium beta (MB) cavity. In the ESS linac, these cavities are used in the energy range of 220–570 MeV.

Before going deeper into the main field, cyclotron, linac, synchrotron and new accelerator schemes are briefly explained due to the wide area of application of accelerators in industry, medicine and science. Subsequently, the main building blocks of the ESS and their functionality are explained, followed by an explanation of certain accelerator design choices, such as the application of superconducting cavities, RF frequency and the use of different cavity types in the ESS linac.

The ESS MB cavity is 6-cell and elliptical. The main considerations for optimizing the design of a multicell elliptical cavity are explained. Moreover, the fabrication process and some details of how the cavity surface is treated are described. In addition, the cavity performance measurement process, including testing methodology, measurement results of vertical test and RF measurement uncertainties, is explained.

Higher order modes (HOM) parasitic excitations in RF cavities, which are mainly a nuisance in superconducting cavities, are studied. Meanwhile the study includes, calculation of HOMs frequency spectrum and a systematic error study to calculate the effect of mechanical errors on a specific HOM frequency deviation. The MB cavity HOM measurement results and the search for a specific HOM are discussed.

Another concern in superconducting cavities is the emission of electrons from the cavity surface, which degrades cavity performance. Therefore the field emission of the MB cavity is studied to provide a detailed understanding

of the dynamics of the field emission. So CST electron tracking simulation is used to provide the field emission trajectory and impact energy. The electron tracking study is also to assess possible field emitter sites on the MB cavity surface. The electron tracking results from different emitter sites are post-processed to count the number of impact electrons versus their impact energy.

Populärvetenskaplig sammanfattning

ESS linjäraccelerator använder supraledande kaviteter för att accelerera mer än 10^{15} protoner från 40% av ljushastigheten till 95% av ljushastigheten, vilket betyder att de bidrar till 95% av protonernas slutenergi.

En av fördelarna med supraledande kaviteter framför normalledande är att praktiskt taget all tillförd energi går till protonerna och nästan ingenting förloras i form av värme. Deras känslighet gör emellertid att design, tillverkning, renhet, testning och drift av sådana kaviteter är förmål för ingående studier.

Denna avhandling fokuserar på att beskriva design, tillverkning, vertikala tester, högre ordningars moder (HOM) och fältemission i ESS supraledande medium betakaviteter (MB). Dessa används för protonenergier mellan 220 och 570 MeV.

Innan fördjupningar görs inom det egentliga området för avhandlingen ges en kort beskrivning av cyklotroner, linjäracceleratorer, synkrotroner och nya accelerationstekniker. Dessa har breda användningsområden inom industri, medicin och vetenskap. Därefter beskrivs ESS-anläggningens huvudsakliga byggstenar och deras funktion, följt av en diskussion om några designval, såsom användandet av supraledande kaviteter, val av RF-frekvens och vilka slags kaviteter som används.

ESS MB-kaviteter är elliptiska 6-cellskaviteter. En beskrivning ges av de viktigaste grunderna för en optimal design av elliptiska kaviteter med flera celler. Därefter följer en beskrivning av tillverkningsprocessen och detaljer rörande hur ytorna behandlas. Även tillvägagångssätt för uppmätning av kaviteternas prestanda, inkluderande mätmetodik, resultat av vertikala tester samt mätfel diskuteras.

Högre ordningars moder, vilket är oönskade excitationer av supraledande RF-kaviteter, studeras. Studierna inkluderar beräkningar av modernas frekvens och en systematisk undersökning av hur mekaniska fel påverkar frekvenserna. Mätresultat för MB-kaviteterna diskuteras, liksom hur man kan identifiera de olika moderna genom mätningar.

Ett annat potentiellt problem med supraledande kaviteter är fältemission från ytorna, vilket leder till energiförluster och en försämring av kaviteternas prestanda. I avhandlingen studeras fältemission från MB-kaviteterna. Tracking av elektroner med hjälp av CST har utförts för att erhålla en

detaljerad insikt i fältemissionens dynamik. Studien med tracking syftar till att hitta den maximala energi som de emitterade elektronerna kan ha när de träffar andra ytor, vilket beror på varifrån de emitteras. Resultaten från trackingen har efterbehandlats för att erhålla antalet elektroner som funktion av denna energi.

List of publications

Some of the original works explained in this thesis have been published previously in the following publications. These papers include contributions by the author of the thesis.

[1] "Passband Modes Excitation Triggered by Field Emission in ESS Medium Beta Cavity Prototype", Proceedings of SRF2017 - ISBN: 978-3-95450-191-5 - DOI: 10.18429/JACoW-SRF2017-TUPB047

[2] "Investigation of HOM Frequency Shifts Induced by Mechanical Tolerances" - MOPVA091 Proceedings of IPAC2017 - ISBN: 978-3-95450-182-3 - DOI: 10.18429/JACoW-IPAC2017-MOPVA091

[3] "Vertical Tests of ESS Medium-Beta Prototype Cavities at LASA" - Proceedings of IPAC2017 - ISBN 978-3-95450-182-3 - DOI: 10.18429/JACoW-IPAC2017-MOPVA063

[4] "Quench and Field Emission Diagnostics for the ESS Medium-Beta Prototypes Vertical Tests at LASA" - MOPVA061 Proceedings of IPAC2017 - ISBN 978-3-95450-182-3 - DOI: 10.18429/JACoW-IPAC2017-MOPVA061

[5] "Fabrication and Treatment of the ESS Medium-Beta Prototype Cavities" - Proceedings of IPAC2017 - ISBN 978-3-95450-182-3 - DOI: 10.18429/JACoW-IPAC2017-MOPVA060

[6] "Experience on Design, Fabrication and Testing of a Large Grain ESS Medium-Beta Prototype Cavity" - Proceedings of IPAC2017 - ISBN: 978-3-95450-191-5 - DOI: 10.18429/JACoW-SRF2017-TUPB046

[7] "LEBT Chopper Electromagnetic and Beam Dynamics Simulations for the Design During the Off-Site Commissioning" ESS Internal report, 2017

Manuscripts in preparation

[1] Field Emission Study of ESS Medium Beta Cavity

[2] Higher Order Mode Analysis of ESS Medium Beta Cavity and a Study of the Effect of Mechanical Errors on HOM Frequency Deviation

List of tables

List of Figures

Introduction

This thesis presents a study of elliptical superconducting cavities focusing on the ESS medium beta cavity and it has six chapters. Chapter one contains a brief explanation of conventional accelerators and the physics behind their operation. Chapter two is an overview of the ESS accelerator and target with an explanation of the functionality of each section. It explains the logic behind some of the design choices made for the ESS accelerator section design.

Chapter three explains the essential characteristics of a superconducting radio frequency (SRF) cavity. It introduces conventional SRF cavities, which are under operation for charged particle acceleration. Moreover, the realization of an SRF cavity with materials other than bulk niobium is assessed.

Chapter four includes the design, fabrication and measurement of the medium beta cavity. The measurement results are for two prototypes that were fabricated before serial production of the medium beta cavity. This chapter explains some of the essential points of an optimum electromagnetic (EM) design in a multicell elliptical cavity. The main independent contributions of the author to the ESS medium beta cavity design and measurement in this chapter are:

- A systematic study to calculate Q_{ext} variation for the power coupler of the medium beta cavity from its nominal value. The assessment is performed based on field flatness variation effect on the coupler Q_{ext}.
- Calculation of the cavity pickup antenna Q_{ext} change from its nominal value due to a mechanical error in the cavity fabrication.
- Major contribution in finalizing the medium beta cavity design by 3D simulations, and the design of a low power coupler antenna and a pickup antenna for the medium beta cavity.
- Collaboration in the ESS medium beta cavity prototypes fabrication by a frequency and quality factor measurement of the cavity

subcomponents. These measurements were to study the cavity geometry evolution from half-cells to a six-cell cavity.

- Major contribution to the medium beta cavity vertical test and measurement of the cavity RF parameters.
- A study on systematic error sources in the cavity RF measurement, including uncertainty calculation in a Q_0 measurement.

Chapter five explains the cavity higher order modes (HOM). First, an overview of a cavity HOM and its effect on an accelerator performance is explained. Afterward the HOMs of the medium beta cavity are studied. The main independent contributions of the author in this chapter are:

- Study of the HOM frequency distribution and determination of dangerous modes for operating the ESS.
- A systematic study to evaluate an HOM frequency deviation (from its nominal value) due to the mechanical errors in the cavity geometry.
- The HOM measurement of the medium beta cavity to find TM_{011} mode. This mode in the design phase is identified as a mode with a potential to degrade beam quality. The HOM was measured to ensure that the frequency shift of the dangerous mode would stay in the calculated boundary. The mode search was conducted by bead-pull measurement and by checking the E-field profile of the modes.

Chapter six is a field emission study of the medium beta cavity. It explains the field emission effect in limiting of a cavity performance. Independent studies by the author in this chapter are:

- Field emission study for the medium beta cavity by electron tracking inside the cavity. The emitted electron movement is due to the cavity field.
- Calculation of maximum X-ray energy due to the field emission for the medium beta cavity and calculation of the number of electrons that may reach different impact energies. It includes post-processing of the electron tracking results.

Parts that are not independent contributions by the author are specified and referenced.

1 Overview of conventional accelerators

Following the invention of charged particle accelerators, it was shown that a key to sustaining acceleration is to implement time-varying electromagnetic fields. Energy of a particle can continuously increase if it passes through a finite alternating voltage gap several times in a circular machine with a rising magnetic field. A conceptual accelerator design requires a comprehension of classical mechanics, electromagnetism and special relativity. Furthermore technology developments in microwaves, superconductivity and the vacuum are key to constructing accelerators with a higher energy and better beam quality at a lower cost. This results in the further development of accelerators that can directly benefit mankind, such as devices that offer more accurate diagnostics, better cancer care, nuclear medicine, and more efficient energy production.

The De Broglie relation explains the dependency between energy and wavelength as:

$$\lambda = \frac{hc}{E}, \tag{1.1}$$

where λ, E, h and c are wavelength, particle energy, Planck's constant and speed of light, respectively. A particle with a higher energy results in a lower wavelength, which enables smaller dimensions to be observed. The wavelength of visible light is 400-700 nm, for *X*-rays it is between 0.01-10 nm, and for a particle accelerator it decreases further to the size of subatomic particles. Thus, a particle accelerator is like a microscope, showing us the building blocks of matter, and has led to the discovery of subatomic particles such as *Z* and *W* quarks and the Higgs boson [1]-[2]. Particle accelerators are now essential tools in modern science and technology. During the last century, different generation of accelerators appeared. It became possible to explain theoretical models (or modify them), illuminating areas of science

that are still unclear. Nuclear medicine, material studies and cancer therapy are examples of how particle accelerators have served humanity. High-energy particle accelerators in different parts of the world are providing scientific data for universities and laboratories in a wide range of applications including: industry, spallation sources (neutron production), nuclear waste treatment and controlled fusion for energy production (accelerator driven systems, ADS)). Below is a brief review of a cyclotron, a linear accelerator, a synchrotron, and new accelerator schemes. The overview is based mainly on [3] and [4]; elements outside these references are cited separately.

Cyclotron

Ernest Lawrence invented the cyclotron in the late 1920s, having been inspired by Wideroe's linear accelerator. He proposed a practical way to bend charged particles with a magnetic field and accelerate them with an alternating voltage. Charged particles in a cyclotron have a circular acceleration that will continue at a fixed revolution frequency. A cyclotron is ideal for accelerating heavy charged particles. To keep the revolution frequency fixed, a larger rotation radius compensates for the increase in particle speed. A proper magnetic field synchronizes the particle rotation with the alternating gap voltage. **Figure 1.1** is a schematic view of an early cyclotron illustrating the synchronization between alternating voltage and particle radius. Ion sources are injected in the center. In the cyclotron, compensation between the centrifugal and Lorentz forces determines the particle radius and revolution frequency such as:

$$\frac{mv^2}{r} = qvB_0 \,, \tag{1.2}$$

$$r = \frac{mv}{qB_0} = \frac{p}{qB_0} \,, \tag{1.3}$$

$$\omega_{rev} = \frac{qB_0}{\gamma m} \,, \tag{1.4}$$

where m is the particle mass, v is the particle speed, q is the charge of particle, B_0 is the magnetic field strength, p is the momentum, γ=E/E_0 (E^2=E_0^2 + p^2c^2) and ω_{rev} is the revolution frequency. Before a particle becomes relativistic, the revolution frequency depends on the magnetic field strength, the particle mass and the charge. After becoming relativistic, a particle's mass increases such that ω_{rev} will decrease. To compensate for this effect, we can increase the magnetic field or decrease the RF frequency

proportional to ω_{rev}. The radius of the cyclotron is proportional to the particle extraction energy. A condition where the RF frequency is equal to the revolution frequency (or a higher harmonic ($\omega_{RF} = h\omega_{rev}$)) is called resonant condition.

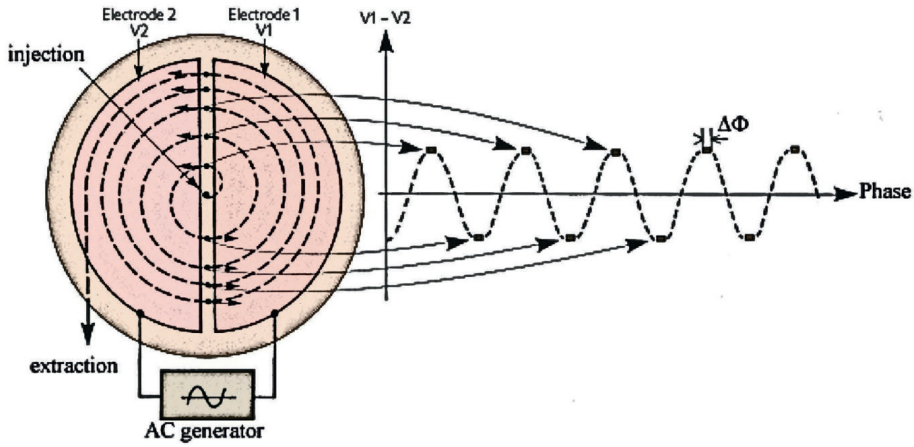

Figure 1.1 Schematic view of on early cyclotron illustrating RF field synchronization with particle rotation radius.

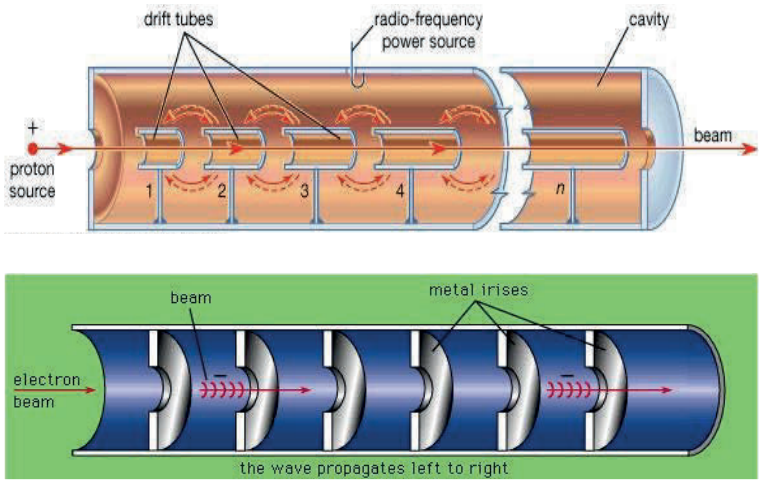

Figure 1.2 (Up) schematic view of a DTL linac. (Down) Schematic view of a traveling wave linac suitable for electron acceleration.

Linear accelerator (Linac)

Luis Alvarez invented the first efficient linac for proton acceleration in 1946. He was inspired by the works of Wideroe and Ising and took advantage of the invention of high-energy klystrons by the Varian brothers in 1937. In a linac, the energy of particles passing along a straight line increases as several alternating voltages are placed in their path. The distance between the gaps is proportional to the charged particle velocity to synchronise particle position with accelerating *E*-field in the gap voltage. There are several linear accelerator types such as: RFQ, DTL, circular waveguide loaded with irises, and side-coupled linacs. Because an electron at rather low energies becomes relativistic[1], it is possible to repeat the same accelerating voltage gap in its acceleration pass. A proton, due to its high rest mass, reaches 95% of the speed of light at 2 GeV. To accelerate proton beam energy until it reaches the speed of light, different linac types will be required. **Figure 1.2** is a schematic view of a DTL and an iris-loaded linac.

Synchrotron

The motivation to develop a synchrotron was based on the desire to increase the acceleration energy of the cyclotron. The only way to double the energy of a proton beam in a cyclotron is to double its radius. This requires four times more steel to construct the magnet. In a synchrotron, the outer edge of the cyclotron's magnet is used to form a closed orbit for the acceleration, around which all the fields are confined. The closed orbit radius is constant and determined by the strength of the dipole magnets and the energy of the particles. Following equation (1.3) and expanding it over the circumference of a circle will result in:

$$\frac{\int B.dl}{p/q} = 2\pi \,, \tag{1.5}$$

where 2π is the total bending angle generated by the dipole magnets over the circumference of the synchrotron.

The invention of strong focusing by including quadrupole magnets in the synchrotron resulted in a significant reduction in beam transversal size. As a result, an intense beam can be confined in a small beam aperture. A cavity in the synchrotron is used to increase the energy of a bunched particle beam.

[1] - 0.5 MeV electron generated by an electron gun reaches 86% of the speed of light

One of the advantages of the synchrotron over a linac is that one cavity can be used to increase the beam energy through several passages of the particle beam through the cavity. A storage ring is a synchrotron with zero beam energy increase and is for particle storage. If the beam in the storage ring is an electron beam, it could be used as an X-ray source (similar to several existing light source facilities). A cavity is needed in such a synchrotron to compensate for synchrotron radiation energy loss in the beam. Another breakthrough in increasing the energy of the synchrotron and preventing excessive increases in machine size was achieved by the invention of superconducting magnets.

New accelerator schemes

For a synchrotron, the equation (1.3) demonstrates the relation between the momentum of a charged particle, the field strength of the bending magnetics and the radius of the synchrotron. Therefore an energy increase for a future accelerator requires synchrotrons with a bigger tunnel radius or a significant jump in the field strength of the bending magnets. The energy radiation loss in the synchrotron reduces the energy of the particle and increases the temperature of the surrounding magnets.

In a linac, there is no synchrotron radiation loss. When a particle beam approaches the speed of light, a series of identically shaped accelerator structures will increase the energy of the particle. Therefore constructing future high-energy colliders on a linac structure frees them from the limitations associated with synchrotrons at high energies. Thus, the International Linear Collider (ILC) holds great promise for particle physicists. The ILC is a proposed linear electron-positron collider based on SRF cavities with a 1.3 GHz RF frequency and a roughly 30 MV/m accelerating gradient. The center of mass energy is planned to be 200–500 GeV, extensible up to 1 TeV [5]. The Compact Linear Collider (CLIC) is another linear electron-positron collider under study whose ultimate center of mass energy is planned to be 3 TeV. It will be composed of two linacs with a 12 GHz RF frequency for the electron and positron acceleration with an accelerating gradient of 100 MV/m [6].

Novel acceleration techniques have been required to overcome the electric breakdown issue in conventional metallic cavities and provide a higher acceleration gradient. The new acceleration techniques need to do more than generate an *E*-field RF mode in a metallic vacuum box. Therefore using plasma for charged particle acceleration is one of future hopes for further

increase in acceleration gradient. In plasma-based accelerators, laser or particle beams are used to produce plasma. Excited space charge oscillation in the plasma will accelerate the charged particle beam without the current levels of limitation in electric breakdown. Two significant achievements in this field are:

- At BELLA in LBNL a laser beam is used for plasma production. In the plasma, electron bunches with a 6 pC charge are accelerated up to 4.2 GeV with a 6% rms energy spread and a 0.3 mrad rms divergence in a 9 cm distance with a 300 TW peak laser pulse [17].
- At FACET in SLAC a particle beam is used for plasma production. Electron bunches with a 74 pC charge in the plasma are accelerated up to 1.6 GeV with a 0.7% energy spread [18].

Currently the plasma acceleration technique and novel techniques other than conventional metallic cavities are still incapable of producing a beam with high luminosity. This makes them inappropriate for high-energy particle physics studies.

2 An overview of ESS

Particle scattering is a solid-state experimental technique for investigating the structural properties of a sample. Neutrons, electrons and X-rays are probe particles that are suitable for particle scattering studies. The X-ray scattering cross section varies with the square of the atomic number (Z^2), whereas neutrons have a high scattering cross section for hydrogen with Z=1. Based on properties of the investigated matter, one of these probe particles is selected for scattering. Due to interaction with electrons on the sample structure, X-rays and electrons have low penetration depth, whereas the neutron, due to its neutral electric charge, has high penetration depth. Neutron scattering and X-ray diffraction are complementary. Whereas neutron scattering is the more expensive of the two, it has critical advantages. It can be implemented to determine microscopic magnetic order and detect antiferromagnetic ordering in a material that cannot be investigated with an X-ray.

A free neutron is an unstable particle with a half-life of roughly 15 minutes. It decays to a proton, an electron and an anti-neutrino. Neutrons for scattering experiments are produced in a nuclear reaction or through an accelerator. Initially, neutron beams for material study were received from research reactors. However, progress in charged particle accelerator technology revealed that accelerator-driven sources would include new advantages for neutron scattering compared with those from the early reactors. The amount of radioactive waste produced by a spallation source like SNS (Oak Ridge National Laboratory) after many years of operation will be equal to the amount produced by a fuel element of the Institute Laue-Langevin (ILL) reactor over fifty days [7]. Furthermore in the spallation process, neutron flux control is achieved by controlling the proton beam.

A neutron beam provided by a reactor is continuous; whereas an accelerator-driven neutron source produces sharp neutron pulses and causes much less heat than a fission reaction in a reactor. Also, a pulsed neutron beam provided

by a proton accelerator has much higher peak brightness than the continuous beam of a reactor.

Using an accelerator driver, neutrons are produced by photofission and spallation reactions. Spallation is the most practical and efficient way to produce neutrons. Three types of accelerators produce the high-energy proton as the spallation driver: a linac, a cyclotron and a synchrotron. A cyclotron such as PSI in Switzerland produces a stable neutron current using a continuous proton beam. Likewise, a linac provides long neutron pulses. ESS and SNS use a linac as the spallation driver. A storage ring at the end of a linac can be used to compress long proton pulses to the range of a few microseconds (ISIS, UK).

In photofission, a high-energy electron collides with a heavy metal target and generates neutrons in a two-stage procedure. The high-energy electron collision with a heavy metal target causes the electron to slow down resulting in gamma radiation due to the Bremsstrahlung effect. The gamma ray generates fast neutrons due to the photofission reaction.

Spallation process

The term ‘spallation’ comes from geology and the verb ‘spell’, means to chip with a hammer. In spallation, the high-energy proton acts as a hammer and the high-energy protons bombard the nuclei of a heavy atom. Therefore the high-energy particle drives the nuclei of the heavy atom into an excited state. This results in the emission (evaporation) of many lower energy neutrons and a variety of lighter particles (**Figure 2.1**). The spallation disintegrates the heavy nuclei, and typically a proton with 1 GeV energy results in 20–40 neutrons evaporating. In the spallation process a neutron yield mainly depends on the proton energy and the target material. **Figure 2.2** demonstrates a neutron yield comparison for uranium, tungsten, gold, tantalum and lead as a function of proton beam energy. An increase in proton beam energy enhances the neutron yield, however this is not a linear dependence; the neutron yield enhancement rate begins to appear saturated from 1 GeV of energy [7].

Practical issues in fabricating the linac, target, and moderator, as well as keeping the shielding requirements reasonable, make 1–3 GeV the optimum boundary for the proton energy. In ESS, the preliminary 2.5 GeV proton energy was reduced to 2 GeV to reduce cost and the number of high beta cryomodules. At the same time, to retain the 5 MW average beam power, the

proton beam current was increased to 62.5 mA. This current was set based on [9]:

- To limit space charge effect on a tolerable level at low energies
- Practical limitation in power delivery to the beam at medium and high energies. The beam current enhancement requires a higher amount of RF power delivery to the beam.
- Beam current enhancement will increase the beam loss.

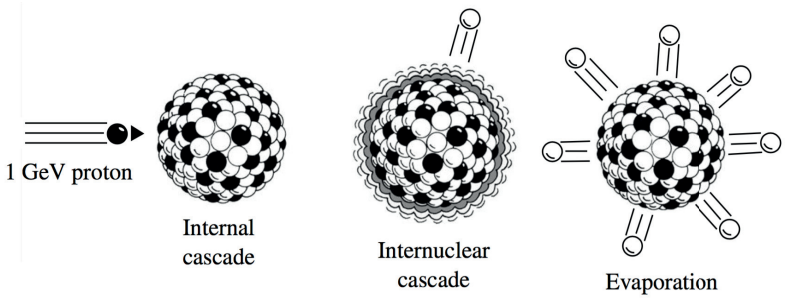

Figure 2.1. Spallation process [7].

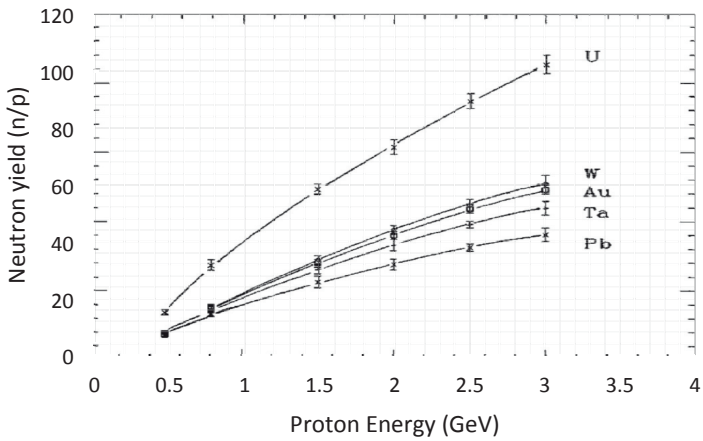

Figure 2.2. Neutron yield for uranium, tungsten, gold, tantalum and lead as a function of proton beam energy [16]

The primary ESS configuration proposed in 2003 [13] and the updated high-level characteristics of ESS are illustrated in Table 2.1 [10]. There are two

main scientific considerations in determining the high-level parameters of ESS:

- To deliver a higher time average neutron flux than in existing continuous sources
- To select a low pulsed repetition rate to maintain efficiency even for the coldest neutrons

Providing a superior neutron flux and maintaining efficiency for the coldest neutron resulted in 357 kJ energy per pulse and 5 MW average beam power for the ESS. This energy per pulse requires a linac to increase the proton beam energy up to around 2 GeV. MYRRHA in Belgium, China's ADS, Project-X in the US and EURISOL in Europe are high-power proton accelerators currently under design.

The following briefly discusses the ESS linac and target, while explaining to some extent their building blocks. It includes details about subsections in each and their functionality. This chapter is prepared based on content in [10], [12], [13] and [15]; elements outside of these references are cited separately.

Table 2.1
High level parameters of ESS **[10]**

Parameter	Value
Average beam power (MW)	5
Proton kinetic energy (GeV)	2
Pulse repetition rate (Hz)	14
Energy per pulse (kJ)	357
Average pulse current (mA)	62.5
Macro pulse length (ms)	2.86
Number of target stations	1
Number of moderators	2
Number of neutron beam ports	42

2.1 ESS linear accelerator section

To accelerate a charged particle along a line in a linac, specific technologies are required, including a source of particles (such as an ion source or an electron gun), RF cavities, magnets, beam diagnostics, vacuum, cooling system, power supply and control systems. **Figure 2.3** shows a block diagram

of the main parts of a linac. A cavity increases the energy of the particles, and magnets (quadrupole or solenoid) focus the particles and prevent the beam from blowing up because of forces such as space charge. While the diagnostic devices track the beam and control its quality. Vacuum systems are for proper beam transmission and to remove sources of beam scattering. Meanwhile the cooling system removes the heat generated by the devices when operating. The power supplies provide adequate electric power for each system, whereas the control system ensures that the entire accelerator is correctly operated and controlled.

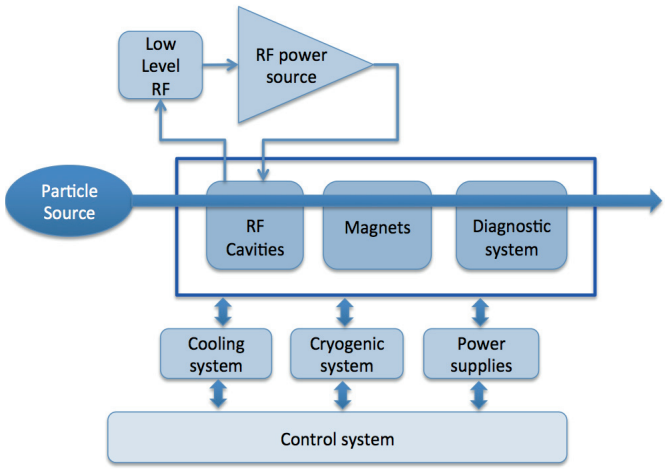

Figure 2.3 Block diagram schematic of main parts in a linac

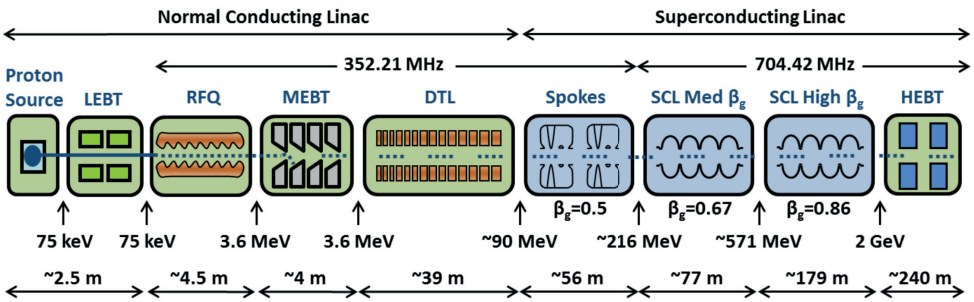

Figure 2.4 Block diagram schematic of ESS linac **[20]**

Below the Lorentz force describes the acceleration, bending and focusing of a charged particle:

$$F = q(E + v \times B) \,, \tag{2. 1}$$

where E, v, q and B are the electric field, charged particle velocity, electric charge and magnetic field, respectively. In a linac, an electric field accelerates the charged particles[2], and a magnetic field may bend or focus them. To increase energy/momentum, it is sufficient to put several alternating gap voltages in the way of a particle. Moreover relative velocity (β=v/c) is explained as a function of particle kinetic energy by:

$$\beta = \sqrt{1 - (\frac{E_0}{E})^2} \,, \tag{2. 2}$$

where E_0 and E are a rest mass energy and a kinetic energy of the particle, respectively. To efficiently accelerate heavy ions and protons, identical cavities should not be in the way of a beam before it gets close to the speed of light. A cavity with a proper transit time factor is required due to the particle velocity change while it becomes relativistic. **Figure 2.4** shows a block diagram schematic of the ESS linac with six different cavity types along the linac. The accelerating structure is divided into normal conducting (RFQ, MEBT and DTL) and superconducting sections (spoke, medium beta and high beta cavities) with a frequency jump from 352.2 MHz to 704.4 MHz in the superconducting section.

The choice of RF frequency in the linac needs to be based on a compromise between mechanical, RF and beam dynamic issues, as well as component availability. Component availability means possibility to order a component off-the-shelf (for example RF power source) or of experience in component design (for example in the cavity and cryomodule). Selecting an RF frequency with no available components and experience in the accelerator community will increase R&D expenditure. In the case of a superconducting elliptical cavity, previous experience of 650 MHz (PIP-II [64]), 704 MHz (TRASCO [63]), 805 MHz (SNS [65]) and 1300 MHz (TESLA [66]) RF frequencies exists. In the following lower and higher frequency comparison is between these frequency ranges.

[2] - In some specific cases, an E-field also is used for particle deflection

Concerning mechanical aspects, a higher RF frequency means smaller cavities and less material consumption per cavity. A higher frequency also results in a tighter machining tolerance, which increases fabrication cost. RF loss in a cavity is derived by:

$$P = \frac{R_S}{2} \int H^2 dA \,, \tag{2.3}$$

where P, H and R_s are the power loss, magnetic field integrated over the cavity surface and cavity surface resistance, respectively. A cavity surface area is inversely proportional to frequency. The cavity surface resistance is composed of R_{BCS}[3] and residual loss. The R_{BCS} scales with the frequency squared, and residual loss is independent of frequency. For frequencies above 3 GHz at 2 K operating temperature, the R_{BCS} term dominates and the cavity RF loss growth is proportional to the increase in frequency. For frequencies below 300 MHz the residual loss term dominates and the cavity RF loss growth is inversely proportional to the increase in frequency [16].

To achieve an efficient use of length in cavities with a higher RF frequency, the number of cavity cells per cavity structure is generally higher. This increases the probability of a trapped mode inside the cavity. A cavity with a lower frequency has a bigger beam pipe radius, resulting in better conditions for HOM propagation out of the cavity. Such compromises for the ESS resulted in a frequency jump from 352 MHz to 704 MHz, occurring between the spoke cavities and the medium beta cavities. The frequency jump may result in a longitudinal unstable crossover for the beam. Nevertheless the 352 MHz frequency provides a larger transverse acceptance for the lower energy part of the linac. Moreover the 704 MHz RF frequency in the elliptical cavities increases efficiency by reducing cavity size and fabrication costs [19].

In the ESS linac after the ion source, the proton beam will be transferred to a low energy beam transfer (LEBT) section. The LEBT should match the beam to the radio frequency quadrupole (RFQ). The RFQ does focuses, bunches and accelerates the proton beam. Furthermore, it preserves beam emittance. Afterwards, the beam moves to a medium energy beam transfer (MEBT) section. The MEBT matches and steers the beam coming from the RFQ to a drift tube linac (DTL), which operates in 0-mode. Afterward, the beam moves to the SRF section and is given an energy boost up to 2 GeV. The SRF

[3] - Bardeen Cooper Schriffer (BCS) resistance, explained in section 4.3.3

cavities deliver 95% of the beam energy. The ESS has three types of SRF cavities: spoke, medium beta (MB) and high beta (HB) cavities. At the end of acceleration, the proton beam will be transferred to the target or the beam dump through the HEBT.

In a high-energy and high-intensity accelerator, regular machine maintenance is essential for high availability. In the ESS, limiting beam power loss meets this requirement. The maximum acceptable beam power loss needs to be less than 1 W/m. A higher beam loss will result in activation and complicates maintenance procedures. One of the issues in terms of beam loss is beam halo. A fraction of particles in a proton beam acquire transverse energy due to the repulsive space charge forces and form the beam halo. Particles in the beam halo can be lost on the beam line wall and cause activation. Formation of the beam halo is mainly due to emittance growth, high space charge, non-linear fields and tune depression, [23] and [24]. Mechanical tolerances and errors in the fabrication, installation and operation of the accelerator components are external sources that may generate a beam halo and cause beam loss growth.

Ion source

The ESS ion source is a microwave discharge type with electron cyclotron resonance (ECR) and microwave power heating for making plasma. The ECR is similar to the charged particle acceleration in a cyclotron. In the ion source the ECR frequency in a magnetic field zone is coupled to the frequency of the microwave source. This provides a resonant coupling between the microwave source and the realized plasma in the chamber. Equation (1.4) shows the resonance coupling between RF frequency and the magnetic field. Using the RF voltage to generate plasma keeps the ion source free from contamination and electron emission, giving the ion source a longer operational life.

Figure 2.5 is a schematic view of the ESS ion source. The plasma chamber is connected to a waveguide from its left side and fed by a 2.45 GHz magnetron. The ridged pattern on the end section of the waveguide is for impedance matching between the RF source and the plasma chamber. This technique minimizes power reflection. The plasma chamber geometry is optimized for a TE_{111} cavity mode. The magnetic system of the ion source has three solenoids. It is designed to provide a flat 875 Gauss magnetic field in the plasma chamber and an ECR condition around the 2.45 GHz frequency. This increases RF power absorption by the plasma and enhances the ion source output current.

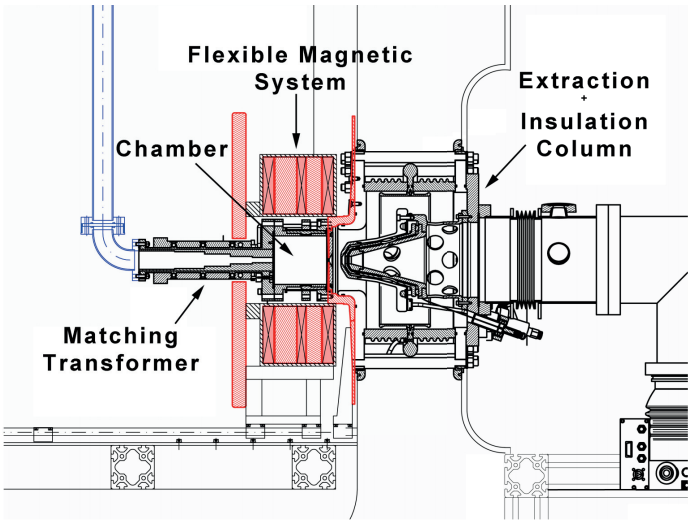

Figure 2.5 Schematic view of ESS ion source **[12]**

LEBT and RFQ

The space charge of the proton beam in the ion source output is high. Therefore the LEBT compensates the ion source beam for afterward RFQ. The LEBT is to prevent emittance blow-up and provide a tight, focused beam on the RFQ entrance. **Figure 2.6** is a schematic view of the ion source and LEBT. It is composed of two solenoids, a chopper, an iris and a Faraday cup. The two solenoids limit the beam cross-section size expansion. The iris adjusts the beam current without changing the ion source settings. The chopper removes low-quality head and tail parts of the beam and provides sharp rising and falling edges for the beam pulse. Chopping the beam at low energy provides low injection beam loss. The maximum flattop pulse time length of the proton current is 3 ms, and the chopper rise and fall time lengths are 100 ns. **Figure 2.7** is a schematic view of the chopper and *E*-field pattern for a 10 kV bias voltage showing the magnitude of vertical *E*-field in the middle of the chopper (calculated by CST [59]). Besides the diagnostics measure beam quality before injection into the linac.

The RFQ has four vanes and works with a TE_{210} mode (a cavity resonance mode which focuses the beam transversely). Alternating a voltage between electrodes produces an alternating transverse focusing channel and bunches beams at a rate of 352.2 MHz. The RFQ is a low-energy beam with β from 0.01 to 0.1 that accelerates the beam from 75 keV to 3.6 MeV.

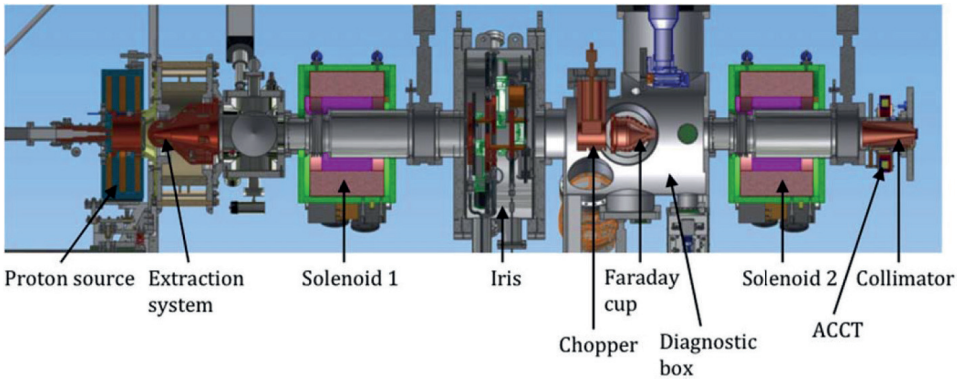

Figure 2.6. Schematic view of the ESS ion source and LEBT [10]

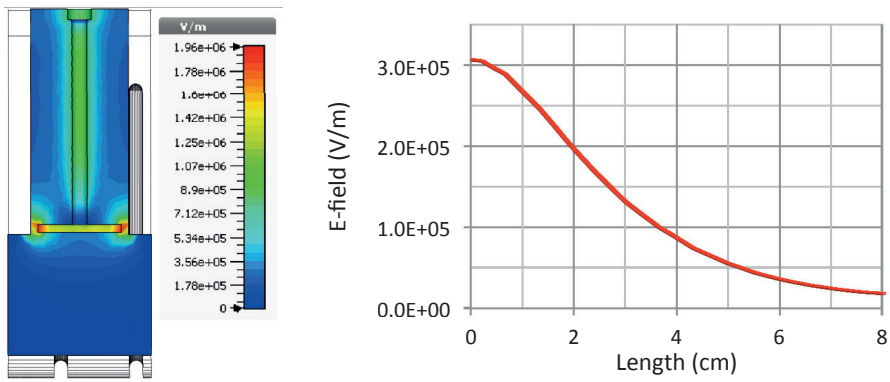

Figure 2.7 (Left) Schematic view of chopper with its *E*-field pattern for 10 kV bias voltage. (Right) Magnitude of vertical *E*-field in the middle of chopper going through the center of the conducting plate.

MEBT and DTL

The MEBT is composed of eleven quadrupoles, three buncher cavities, a series of diagnostic tools, a fast chopper and a beam dump. The quadrupoles and buncher cavities adjust the transverse and longitudinal characteristics of the beam, respectively. **Figure 2.8** is a schematic view of the MEBT lattice and beam envelope variation along the MEBT. Initially a quadrupole triplet is used to focus the beam entering the MEBT. To compensate the beam expansion after the chopper and beam dump, a second quadrupole triplet is placed after the second buncher cavity. The last four quadrupoles are optimized to provide a transverse match between the MEBT output and the DTL input. The three bunchers are identical, but their gap voltages are different. **Figure 2.8** shows that the third buncher implements the largest

phase reduction and delivers a smaller beam size to the DTL than the MEBT input. This is due to the highest gap voltage provided for this cavity compared with others. Table 2.2 shows the main parameters of a buncher cavity. The 150 kV is the maximum applicable gap voltage on the bunchers. The fast chopper removes uncompensated bunches from the head and tail of the pulse.

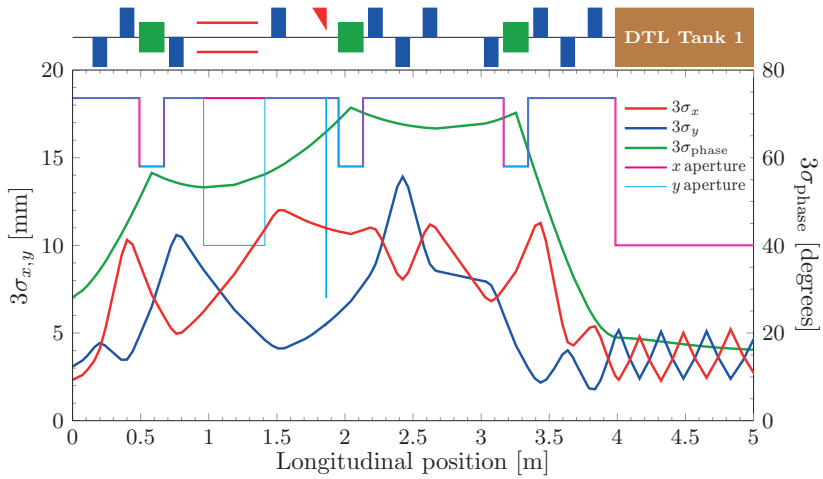

Figure 2.8 (Up) Schematic view of MEBT lattice componenets, (Down) Beam envelope variation versus beam aperture. (Blue boxes are quadrupoles, green boxes are buncher cavities, parallel red line is fast chopper and red triangle is beam dump) **[26]**.

Table 2.2
Main parameters of a buncher cavity in MEBT **[10]**

Parameter	Value
RF (MHz)	352.2
Gap voltage (kV)	150
Q_0	23477
Transit time factor	0.643
Shunt Impedance (MΩ)	1.65
Power dissipation (kW)	13.7

A DTL is a series of drift tubes suspended from the outer tank by a stem on the cavity axis to make a series of coupled cells with no wall in between. A voltage gap between drift tubes accelerates the beam, and the beam is inside the drift tube while the *E*-field is decelerating. The ESS DTL works at 352.2

MHz and it is similar to CERN LINAC4 DTL [31]. Permanent quadrupole magnets in every other drift tube of the DTL are implemented to realize an FODO lattice for transverse focusing.

SRF section

Copper cavities are much cheaper than the SRF cavities. The copper cavity application includes no cryogenic, which means less complication in operating and maintaining the accelerator. From equation (2.3), the cavity power loss increases with the square of the cavity accelerating voltage. Surface resistance in the SRF cavities is roughly six orders of magnitude lower than the copper cavities. A continuous wave (CW) and long pulse length operation mode for a copper cavity will limit its accelerating gradient to a few MV/m. This is due to excessive power loss in the copper cavity in such operation modes. Because surface resistance is much lower, the accelerating gradient in the SRF cavity can be much higher for such operational modes. For instance, the 1300 MHz SRF cavity can operate in CW mode at 16 MV/m at 2 K [28] and [29].

The SRF cavities in the ESS linac are based on a required high acceleration gradient and long RF pulse length. The main criteria in the SRF section design are construction cost, power consumption, reliability and maintenance. The SRF linac length is directly related to the linac cost so the design of this section is optimized to have the shortest possible SRF linac section.

A spoke cryomodule contains two spoke cavities, each of which has three accelerating gaps. The spoke cavities can be tuned based on the proton beam in the linac, therefore they provide flexibility in the linac operation. The relative velocity change in the proton beam in the spoke cavities is 0.42–0.58. The spoke cavities accelerate the beam from 90 MeV to 216 MeV.

The radio frequency after the spoke cavity section increases to 704 MHz for the superconducting elliptical cavities, of which there are two types: A five-cell (medium beta) cavity and a six-cell (high beta) cavity. A cryomodule in the elliptical cavities section contains four cavities for both of the five-cell and the six-cell cases. In the medium beta SRF section, relative proton beam velocity changes from 0.58 to 0.78. The relative beam velocity change in the high beta section is 0.78–0.95. **Figure 2.9** shows a cross section view of the three SRF cavities implemented in the ESS linac. The cavities are inside their helium tank with a power coupler antenna.

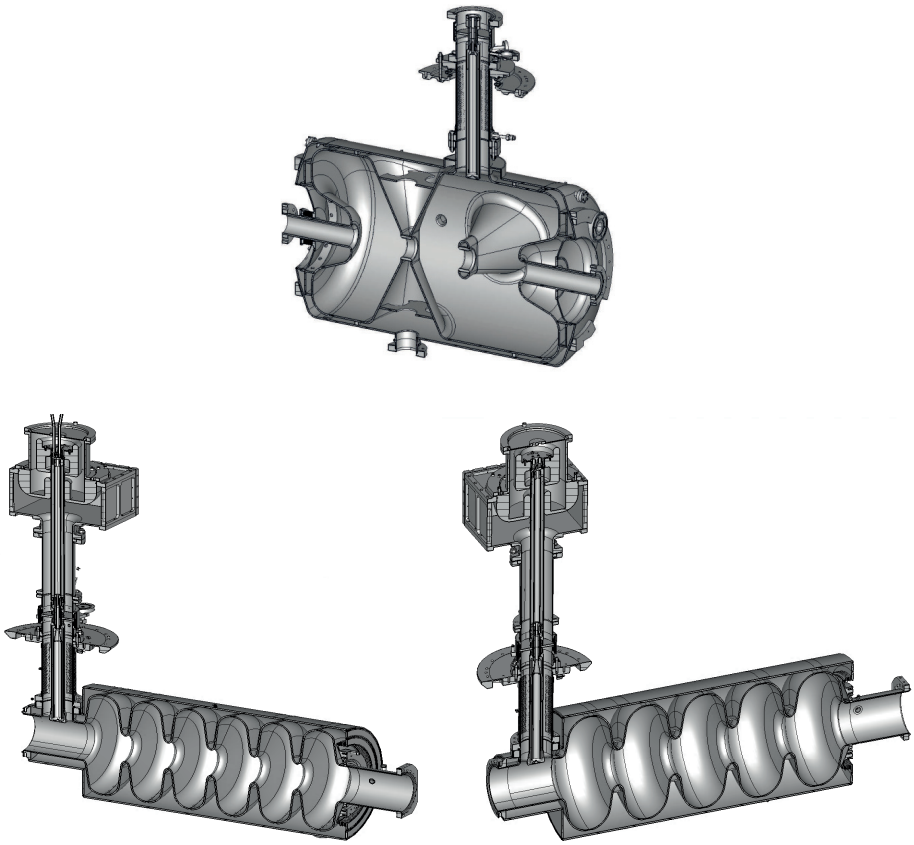

Figure 2.9 Cross section of the ESS SRF cavities. (Up) spoke cavity (Down-left) medium beta cavity, (Down-right) high beta cavity

HEBT

The HEBT transfers the beam from the accelerator to the target section and is composed of four main sections, including:

- HEBT-S1: A straight section for a possible energy upgrade of ESS. There is a set of matching quadrupoles at its end.
- HEBT-S2: For transferring the beam from the linac, which it is underground, to above the ground. It is composed of two bending magnets in the beginning of the section to bend the beam vertically and another two bending magnets that bend the beam toward the target.

- HEBT-S3: Transports the beam to the target at ground level. A proton beam window is placed at the end of this section to separate the accelerator vacuum system from the target.
- Beam dump: For machine studies, tuning and commissioning issues, the beam will be sent to the beam dump.

Figure 2.10 is a schematic view of four sections of the HEBT and its interface with the target section. The dipole magnets at the beginning of the HEBT-S2 act as a switch to choose the target or the beam dump for the proton at the end of the acceleration tunnel. There is an expander system to spread the proton beam on a rectangular profile on the rotating target surface.

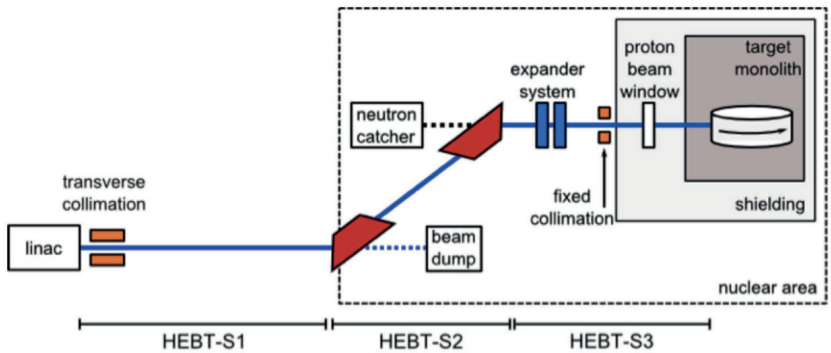

Figure 2.10 Schematic view of the HEBT and target **[13]**

2.2 ESS target section

The target section has three main functions: to convert a pulsed proton beam through nuclear spallation reaction into fast neutrons; to transform fast neutrons emitted by the target into slow neutrons through a moderator-reflector; to divide and guide the slow neutrons into 42 neutron extraction beam lines. Beam ports are accessible at the end of the target shielding to provide neutrons for the neutron scattering instruments. The neutrons' energy distribution after moderation depends on the moderator temperature. **Figure 2.11** shows Maxwell-Boltzmann flux distribution for 25 K, 300 K and 2000 K moderator temperature [7].

In addition to the neutrons that are the desired product of the spallation, there will be a large amount of radioactive isotopes and radiation as unfavourable products. The fast neutrons have roughly 10% of the speed of light, and the moderator-reflector system reduces their speed to the speed of sound to make them usable by the instruments.

The monolith is located in the center of the target station. Its inside view is demonstrated in **Figure 2.12**. It is composed of a rotating target wheel at its heart, two moderator-reflector systems, one above and one below the target wheel, and the beam extraction lines. A proton beam window is the entrance point for the proton beam pulse into the target section.

The ultimate goal of ESS is to produce intense beams of neutrons for neutron scattering studies and all machine sections are optimized to supply the highest possible source brightness. The material and shape of the target are optimized to increase neutron yield. **Figure 2.13** shows the target wheel, whose inner section is made of steel and outer section is composed of radial sections filled with tungsten bricks. The proton beam collides with the tungsten in the target wheel. Tungsten is a dense material with high neutron production density, high conductivity and a high melting temperature. These make tungsten a suitable material choice for the spallation process. To reduce the temperature increase in tungsten without significantly degrading neutron production, the 5 MW proton beam is expanded to a 60 × 160 mm cross section footprint by quickly switching magnets on the rotating target. This has extended the target life by up to five years.

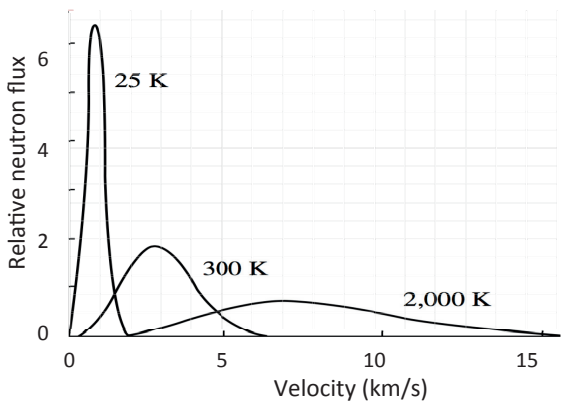

Figure 2.11. The Maxwell-Boltzmann flux distribution for 25 K, 300 K and 2000 K moderator temperature [7]

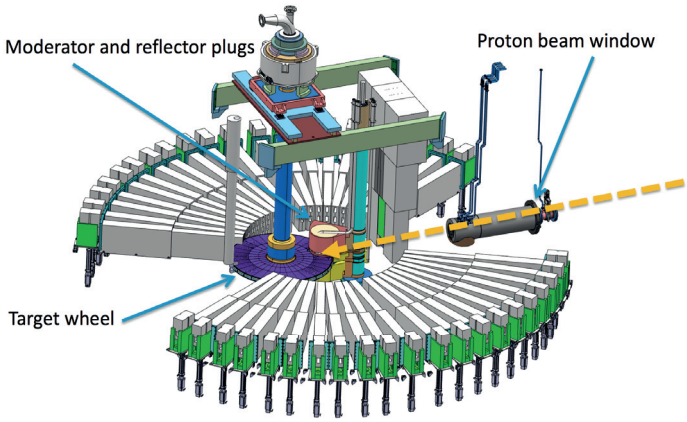

Figure 2.12 Inside view of ESS target monolith includes target wheel, neutron beam extraction lines, moderator-reflector system and proton beam window (entrance of proton beam) **[12]**

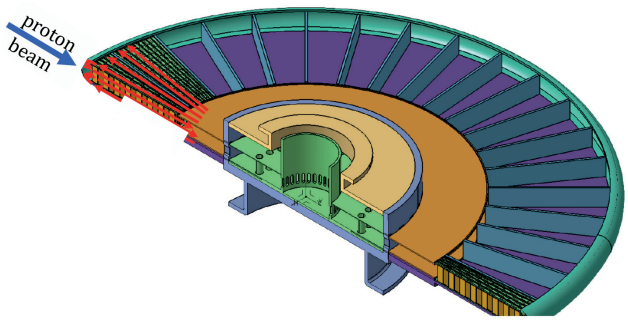

Figure 2.13 Sketch of the ESS target wheel [14].

3 Superconducting RF cavities

Temperature reduction of a superconductor below its critical temperature (T_c) results in a phase transition at the T_c and leads to roughly zero resistance against dc electric current. Another significant characteristic of superconductivity is the expulsion of magnetic fields, called the Meissner effect [32]. A temperature increase above T_c or exposing the superconductor under a magnetic field higher than its critical magnetic field (H_c) will annihilate the superconductivity and return normal conductivity. Both T_c and H_c are characteristic properties of superconductors. A temperature increase on a superconductor results in a lower H_c for annihilating superconductivity. Furthermore, implementing a magnetic field on a superconductor also reduces T_c. Apart from temperature and magnetic field, a current passing through the superconductor in its critical value (I_c) breaks the superconductivity. Again, the critical current value is a function of the temperature and applied magnetic field. Transition to the superconductivity phase is determined by these three characteristic properties. **Figure 3.1** is a schematic view of the superconducting critical surface phase diagram for type-I and type-II superconductors, a visual demonstration of the superconducting boundary defined by I_c, T_c and H_c. This interaction in a superconductor is explained by free energy as:

$$F = U_{int} - TS \,, \tag{3. 1}$$

where U_{int}, T and S are internal energy, temperature and entropy, respectively. An external magnetic field on a superconductor induces current in the solid penetration depth to cancel the external field effect and keep the magnetic field excluded from the inside. Increasing the external magnetic field to H_c will make the free energy equal for the normal conducting and superconducting states. This is explained as:

$$F_s(H_c) = F_n(H_c) = F_s(H = 0) + \mu\, V_s \int_0^{H_c} H\, dH \,, \tag{3. 2}$$

where V_s is the superconductor volume. As demonstrated, the magnetic field enhancement increases the free energy of the superconductor, so a temperature increase of less than T_c will annihilate the superconductivity.

The physics of superconductivity is explained by the BCS theory, i.e. when a metal becomes superconductive, interaction between conduction electrons and phonons (lattice vibrations) results in the formation of paired electrons, Cooper pairs. A Cooper pair is a boson to which the Pauli exclusion principle does not apply and which condenses into a single quantum ground state. In a superconductor there is a 2Δ energy gap between excited energy levels and quantum ground state, i.e. the energy to break Cooper pairs. The energy gap $2\Delta(0)=3.53k_BT_c$ resulting in the energy gap which is normally only a few meV. Therefore the specific heat and RF surface resistance in a superconductor are temperature-dependent. Experimental evidence has demonstrated the influence of the energy gap (2Δ) in the electronic energy levels.

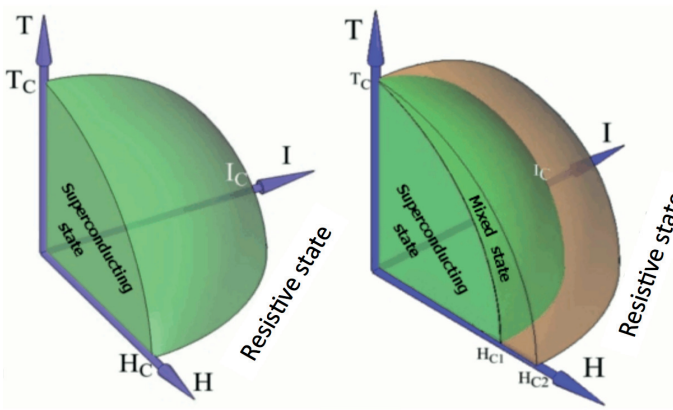

Figure 3.1. Superconducting critical surface phase diagram (left) for a type-I superconductor (right) for a type-II superconductor [34]

The magnetic field penetration inside a superconductor has an exponential decay, i.e. London penetration depth (λ_L). Electric current flow in a superconductor will be confined in a depth of λ_L. Another important length scale associated with a superconductor is coherence length (ξ_0), which shows the density change of Cooper pairs in a superconductor. Superconductors are generally divided in two main categories: type-I and type-II. A type-II superconductor has two critical magnetic field levels: lower and upper (H_{c1} and H_{c2}, respectively). Up to H_{c1}, there is no magnetic field penetration inside

the superconductor (Meissner state), whereas between H_{c1} and H_{c2} an array of normal conducting boundaries form inside the superconductor while superconductivity still exists. For the magnetic field higher than H_{c2}, the material transforms to normal conducting state (**Figure 3.1** (right)). In type-I superconductors there is no intermediate state, and implementing a magnetic field of H_c will annihilate superconductivity (**Figure 3.1** (left)). The Ginzburg-Landau parameter ($K_{GL} = \lambda_L/\xi_0$) distinguishes type-I and type-II superconductors from each other. For a type-I superconductor, K_{GL} is smaller than $1/\sqrt{2}$; for type-II superconductors, K_{GL} is higher than $1/\sqrt{2}$. **Figure 3.2** demonstrates λ_L and ξ_0 lengths for type-I and type-II superconductors.

A type-II superconductor with high H_{c2} is useful for fabricating superconducting magnets because dc electric current flows without loss while the material is superconductive. In the SRF cavity case, an RF-critical magnetic field has a significant role. The imperfections and impurities in the RF penetration depth facilitate thermal breakdown and are quenched before magnetic field rises to the critical magnetic field.

Above explanations for superconductivity are prepared from content in [33] and [34]. After a brief overview of cavity figures of merit, this chapter explains conventional SRF cavities under study. Furthermore, spoke and elliptical cavities are explained in more detail due to the wide interest in their application. At the end, a short overview of some of the studies that introduce materials other than pure niobium sheets for SRF cavity fabrication is presented. Those studies aim to increase the SRF cavity acceleration gradient, increase the operating temperature and reduce operation cost.

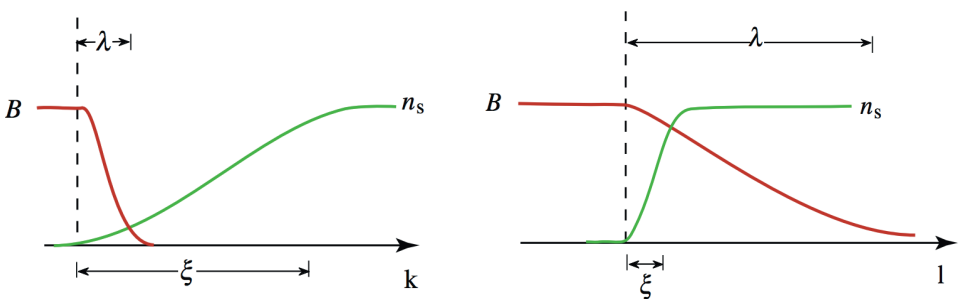

Figure 3.2. Illustration of London penetration depth and coherence length in (Up) type-I (Down) type-II superconductor [30]

3.1 Cavity figures of merit

The design of a cavity determines its efficiency in concentrating the field in the region of the beam, as well as storing energy, having the correct resonant frequency, and other functions. The following explains some of figures of merits of a cavity, which are prepared from [32].

The cavity accelerating voltage is defined as the voltage seen by a particle of charge q traveling on the cavity axis, such that:

$$V_{acc} = \left|\frac{1}{q} \cdot maximum\ energy\ gain\ possible\ during\ transit\right|. \quad (3.\ 3)$$

This voltage is given by the line integral of the electric field along the longitudinal cavity axis, E_z, as seen by the particle:

$$V_{acc} = \left|\int_0^L E_q dz\right|, \quad (3.\ 4)$$

where L and E_q are the cavity active length and on-axis field (as a function of time and position), respectively:

$$E_q = E_Z(r = 0, z)e^{j\left(\frac{\omega_0 z}{c}+\varphi\right)}, \quad (3.\ 5)$$

where ω_0 is the angular frequency of the accelerating mode and φ is an arbitrary phase. We find:

$$V_{acc} = \left|\int_0^L E_Z(r = 0, z)e^{j\left(\frac{\omega_0 z}{c}+\varphi\right)} dz\right|. \quad (3.\ 6)$$

Often, the average accelerating electric field E_{acc} is quoted, which the particle sees during its transit. This is given by:

$$E_{acc} = \frac{V_{acc}}{L}\ \left[\frac{V}{m}\right]. \quad (3.\ 7)$$

Cavity stored energy

The electric and magnetic fields in a cavity are 90 degrees out of phase. The energy stored in the EM field of a cavity mode is continuously oscillated back and forth between the electric and magnetic fields. On average, the

stored electric and magnetic energies are equal. The energy stored in a cavity mode is given by:

$$U = \frac{1}{2}\int_V^C \varepsilon_0 E^2 dV = \frac{1}{2}\int_V^C \mu_0 H^2 dV. \quad (3.\ 8)$$

The time dependence of these fields in the cavity generates currents which flow within a thin surface layer δ (skin depth) of the cavity walls:

$$\delta = \sqrt{\frac{2}{\sigma\omega\mu}}\ , \quad (3.\ 9)$$

where σ is the conductivity of the cavity wall. The surface current sees the surface resistance R_s that is given by:

$$R_S = \frac{1}{\delta\sigma}\ . \quad (3.\ 10)$$

Power dissipation and quality factors

The surface current induced by the magnetic field of the cavity mode causes resistive loss. The power dissipation per unit area due to Joule heating is explained by equation (2.3). One of the most important characteristics of a cavity is its "unloaded quality factor" (Q_0), which determines the amount of power required to keep the stored energy inside the cavity. It is defined as:

$$Q_0 = \frac{Stored\ Energy}{Energy\ consumed\ per\ period} = \omega_0 \frac{Stored\ Energy}{Dissipated\ Power} = \frac{\omega_o U}{P_{diss}}, \quad (3.\ 11)$$

where P_{diss} is the resistive loss on the cavity wall. In this case:

$$Q_0 = \frac{\omega_0\mu_0}{R_S} \cdot \frac{\int_V^C \mu_0 H^2 dV}{\int_S^C |H_\vartheta|^2 ds}. \quad (3.\ 12)$$

Other important cavity figures of merit are shunt impedance R and R/Q factor. Shunt impedance is defined as:

$$R = \frac{V_{acc}^2}{P_{diss}}. \quad (3.\ 13)$$

Note that shunt impedance has to be maximized to get maximum acceleration for lower power loss. The R/Q factor relates the accelerating voltage to the stored energy and is given as:

$$\frac{R}{Q} = \frac{V_{acc}^2}{P_{diss}} \cdot \frac{P_{diss}}{\omega_0 U}. \tag{3. 14}$$

Some of the properties of the R/Q are:

- Independent of size (frequency) and material
- Depends on mode geometry
- Proportional to the number of cells
- For the elliptical cavities R/Q ~ 100 Ω per cell
- Inversely proportional to the beam hole diameter

To operate the cavity, we have to connect it to some source of energy in order to feed the cavity with the RF field. Also, to measure the energy of the field, an output port is required. In practice, we use an input probe antenna to inject RF power into the cavity and a pickup probe antenna to monitor the E-field level inside the cavity. To measure the cavity external figures of merit, we feed the cavity and charge it to reach a steady-state field and then turn the RF generator off. After RF is turned off, stored energy in the cavity dissipates through power loss on the cavity wall (P_{diss}), power radiated back to input coupler (P_{e}), and power transmitted out through the pickup antenna (P_{t}). The total power loss is equal to:

$$P_{tot} = P_{diss} + P_e + P_t. \tag{3. 15}$$

Using the total power loss, the loaded quality factor is:

$$Q_L = \frac{\omega_0 U}{P_{tot}}. \tag{3. 16}$$

With the same approach, we can calculate Q_{i} and Q_{t} (external quality factors) for the input and pickup probe ports as:

$$Q_i = \frac{\omega_0 U}{P_e}, \tag{3. 17}$$

$$Q_t = \frac{\omega_0 U}{P_t}. \quad (3.\ 18)$$

Based on (3.15), (3.16), (3.17) and (3.18), we can write:

$$\frac{1}{Q_L} = \frac{1}{Q_0} + \frac{1}{Q_i} + \frac{1}{Q_t}, \quad (3.\ 19)$$

$$Q_0 = Q_L(1 + \beta_i + \beta_t). \quad (3.\ 20)$$

Geometrical parameter (G)

This is a product between the cavity quality factor and the surface resistance, as:

$$G = R_s Q_0 = \omega_0 \mu_0 \cdot \frac{\int_V^C \mu_0 H^2 dV}{\int_S^C |H_\vartheta|^2 ds} = 2\pi \sqrt{\frac{\mu_0}{\varepsilon_0}} \cdot \frac{1}{\lambda} \cdot \frac{\int_V^C \mu_0 H^2 dV}{\int_S^C |H_\vartheta|^2 ds} = \frac{2\pi Z}{\lambda} \cdot \frac{\int_V^C \mu_0 H^2 dV}{\int_S^C |H_\vartheta|^2 ds}. \quad (3.\ 21)$$

$Z = 377\ \Omega$ is the vacuum impedance and $\lambda\omega_0 = 2\pi c$. It has been demonstrated that G is independent of size and material, and depends only on the shape of the cavity and electromagnetic mode. When the resonator is connected (coupled) to the external world, we can define loaded Q (Q_L) and external Q (Q_{ext}) for the cavity, in addition to Q_0. In these two cases (Q_L and Q_{ext}) the power loss on the cavity ports is taken under consideration.

3.2 Superconducting accelerating structures

The SRF cavities applied for charged particle acceleration are divided in two main categories: TM[4] and TEM[5] mode cavities. The TM mode cavities are for the charged particle acceleration in the $0.6<\beta<1$ range and the TEM mode cavities are for acceleration in the $0.01<\beta<0.6$ range. An elliptical cavity is a TM mode resonator working in single cell or multicell shapes with $\beta\lambda/2$ gap voltage length per cell. The cells resonate in TM_{010} mode. Normally a multicell elliptical cavity operates in a π-mode.

[4] - Transverse magnetic (TM)

[5] - Transverse electric magnetic (TEM)

The TEM mode SRF cavities are available in three structures: a quarter wave resonator (QWR), a half wave resonator (HWR), and a spoke cavity [28]. In this section, after a short review for the low and medium β SRF cavities, the operation and design of the spoke cavity and the elliptical cavity are explained in some detail.

3.2.1 Low and medium β SRF cavities

The low and medium β SRF cavity applications are in a high duty cycle, and heavy ion and proton linacs (usually low current). Cavities in this β range are divided in two main types: the QWR and the HWR cavities. There are two types of HWR cavities: coaxial and spoke. These cavities have a low beam loading. The bigger beam pipe radius of an SRF cavity (in comparison with a normal conducting cavity) makes it possible to use a larger transverse beam size, which helps minimize beam losses. For cavities in the $0.03<\beta<0.1$ range, a low RF frequency is desired. The lower RF frequency results in a longer wavelength, a longer bunch and a lower space charge effect. It also provides a longer practical acceleration length for the cavity. It is preferable to operate these cavities at 2 K rather than 4 K (especially in big accelerator machines) to ensure a lower surface resistance and stable helium pressure. Stable helium pressure results in less cavity frequency change and less mechanical stress. The effective cavity cell length in cavities similar to elliptical cavities is $\beta\lambda/2$. Typically, in fabricating the SRF cavity for better heat transfer; a thin niobium sheet is implemented. Moreover, the cavity is integrated inside a helium vessel to provide stable mechanical operating conditions.

In the SRF cavity, it is desirable to confine the cavity volume around the beam trajectory to ensure efficient use of the cavity material and cryostat space. The cavity aspect ratio is a parameter that compares a confined volume around the beam pass trajectory for different cavity types. In a cavity, it is defined as the ratio of longitudinal length over transverse length. As the diameter of an elliptical cavity is roughly 0.8λ, its aspect ratio for a cell is roughly 0.6β; for the QWR and the HWR the ratio is 2β and β, respectively. The QWR and the HWR cavities typically have few accelerating gaps. Therefore, it is possible to use them for a wide variety of heavy particles with flexible phase adjustment between the cavities. Table 3.1 compares the main RF parameters for some of the TEM SRF cavities.

QWR cavities

The QWR cavity is a transmission line resonating in the TEM mode, with a gap voltage, which is loaded by a $\lambda/4$ shorted line at one of its ends. In contrast to elliptical cavities, they are designed for lower RF frequencies and lower charged particle relative velocity (β=v/c). **Figure 3.3** is a schematic view for QWR cavities with cylindrical, tapered and racetrack shapes. In the QWR the electromagnetic field distribution around the beam is asymmetric, which results in a transverse kick for the beam. There are two procedures for correcting this issue, both aiming to compensate for the transverse kick:

- Inserting a displacement along the length of the inner resonator in the installation process.
- Changing the beam port profile shape to generate a transverse *E*-field component

To decrease E_{peak}/E_{acc}[6] and H_{peak}/E_{acc}[7] in the QWR cavity, the $\lambda/4$ resonator shape is modified from a cylindrical to tapered and racetrack geometry. The inner conductor shape has a significant role in peak field compensation [35].

Table 3.1.
A list of SRF TEM type cavities with characteristic performance

Project	Cavity	Frequency (MHz)	β	E_{acc} (MV/m)	E_{peak}/E_{acc}	B_{peak}/E_{acc} (mT/(MV/m))	Reference
PIP-II	HWR	162.5	0.11	9.7	4.63	4.98	[95]
PIP-II	spoke	325	0.22	10	3.84	5.81	[95]
PIP-II	spoke	325	0.47	11.4	3.51	5.66	[95]
ESS	Double-spoke	352	0.5	8	4.4	8.7	**[10]**
MYRRHA	Single-spoke	352	0.37	6.2	4.29	7.3	[11]
China ADS	HWR	162.5	0.1	5	5.9	12.1	[41]
China ADS	HWR	162.5	0.15		4.9	6.1	[41]
China ADS	Double-spoke	325	0.52	9	3.8	7.6	[42]

[6] - Ratio of the surface peak *E*-field over accelerating gradient field

[7] - Ratio of the surface peak *H*-field over accelerating gradient field

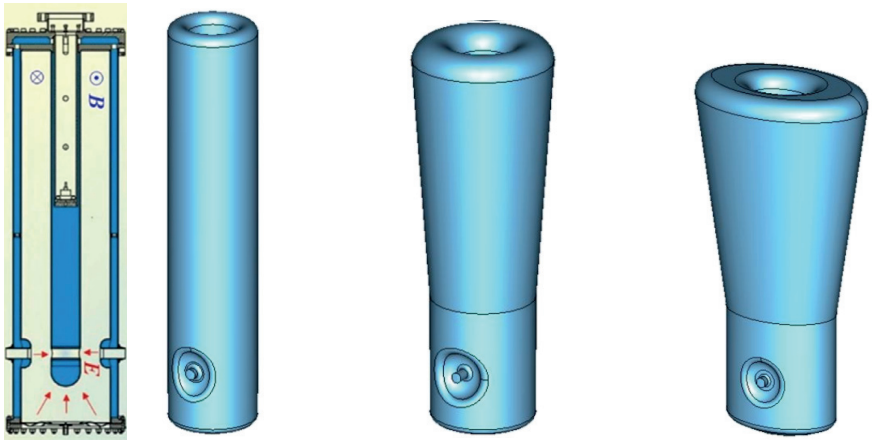

Figure 3.3 Sketch of three QWR cavity with two voltage gaps (a) cylindrical (b) tapered (c) race-track [35]

HWR cavities

Combining two QWRs from the open side of the transmission line as demonstrated in **Figure 3.4** will result in an HWR cavity. The transverse length of these cavities is double that of a QWR. Due to symmetric field distribution around the beam in the HWR cavity, the unwanted transverse kick is eliminated. The inner conductor has a significant role in optimizing E_{peak} and H_{peak}. In a design for the PIP-II HWR cavity, inner conductor geometry is ring shaped. **Figure 3.5** is a schematic view of the cavity geometry and its EM field distribution [43].

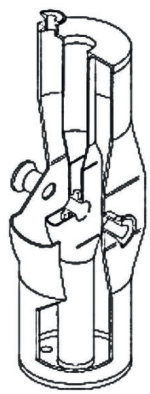

Figure 3.4 Schematic view of a HWR cavity cross section (Coaxial type) [35]

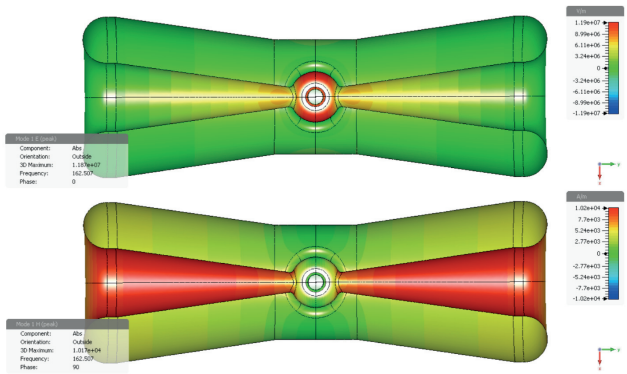

Figure 3.5. EM field distribution for an HWR cavity with ring-shape inner conductor. (Top) *E*-field distribution (Bottom) H-field distribution [43]

3.2.2 Spoke cavities

A spoke cavity has a lower transverse size than an elliptical cavity for a similar RF frequency. It is composed of an outer cylinder (cavity outer conductor), re-entrant irises on the cavity sidewalls and one or a few spokes inside the cavity. A spoke is radial, perpendicular to the beam pass and has an aperture for the beam pass at its center. The geometry of a spoke is divided into two areas: the spoke base (intersecting outer conductor wall) and the spoke aperture (intersecting the beam line). The spokes increase the capacitive effect of the cavity and their number determines the number of accelerating gaps and the cavity length. There will be n+1 accelerating gaps for n spokes. A spoke cavity works in a TEM mode with a 180-degree phase difference between the *E*-field of adjacent cavity cells. There is magnetic coupling between cavity cells. A cross-spoke configuration (subsequent spokes being perpendicular to each other) provides high cell-to-cell *H*-field coupling. Therefore, field flatness tuning is not required and, compared with an elliptical cavity; it is much less sensitive to trapped higher order modes (HOMs) [36]. Ports for the cavity power coupler and pickup antennas are placed on the outer conductor surface of the cavity.

In a spoke cavity, the primary design is based on nominal resonant frequency and β_{opt} (particle relative velocity to the speed of light). The cavity diameter and L_{acc} (iris to iris length) are optimized based on the cavity frequency and β_{opt}. In the second step, the cavity geometry will be optimized to achieve minimum values for $E_{\mathrm{peak}}/E_{\mathrm{acc}}$ and $H_{\mathrm{peak}}/E_{\mathrm{acc}}$ and to choose the re-entrant length on the end-cups. A high surface H-field results in cavity quench,

whereas a high surface E-field results in field emission. An optimum cavity design requires cavity simulation with numerical codes and the derivation of optimum values for the cavity geometry. **Figure 3.6** illustrates a cross section of the ESS spoke cavity with two spokes. An effective approach generally used to reach optimum geometry values for a cavity design is to tune one geometry parameter in each step while other parameters are fixed. When the optimum value for the geometrical parameter under study is found, it is fixed and another parameter can begin to be optimized. This process will be repeated until the optimum value for all the parameters are found.

The ESS spoke cavity EM simulation results for E-field and H-field distributions are illustrated in **Figure 3.7**. As shown, the concentration of H_{peak} is around the spoke base, whereas E_{peak} distribution is around the spoke apertures and cavity irises. E_{peak} and H_{peak} optimization is highly dependent on the geometry of the spokes. A bigger spoke base with a greater surface area for H-field distribution decreases the H_{peak}. The main geometrical shapes used for the spokes in literature are cylindrical, elliptical and racetrack or a combination of these. A cylindrical shape is easier to fabricate but results in a higher peak magnetic field than others. Studies on spoke cavities in [37]–[39] show that racetrack spoke geometry may deliver lower values for the E_{peak}/E_{acc} and H_{peak}/E_{acc}. The ESS spoke cavity has a conical spoke with a circular base. This is based on the IPN Orsay experience of engineering complexities in shaping such spokes and welding the spoke to the outer conductor [38].

Resonant frequency varies during a spoke cavity power test at 2 K, due to a pressure change in the saturated liquid helium, microphonics and Lorentz force detuning. In a spoke cavity, frequency change is compensated for by a tuning system installed on one side of the spoke cavity helium tank designed to pull and stretch the cavity beam pipe flange. The tuning system is composed of a slow and a fast tuner. The slow tuner pulls the cavity beam pipe through a system comprised of a stepper motor, ball screws and lever arms. The slow tuner design requires high force to be applied with fine precision (**Figure 3.8**). The fast tuner section is composed of two piezos inserted in lever arms. The slow tuner is for cavity low power resonant frequency tuning, whereas the fast tuning systems corrects Lorentz force detuning.

The spoke cavity power coupler is a 50 Ω coaxial line with a ceramic window for vacuum insulation. It has capacitive coupling to the cavity's electromagnetic field. **Figure 3.9** is a schematic view of the ESS spoke cavity

cryomodule. It is composed of two double-spoke cavities, each of which has a separate power coupler. The power couplers inject the RF power to the cavity from the lower side. There is a doorknob transition between the waveguide and the coupler coaxial line for impedance matching and to transform the waveguide TE_{10} mode to the coaxial line TEM mode. This is for RF efficiency and to achieve minimum power reflection. The maximum RF transition in the doorknob is achieved by its geometry and position optimization.

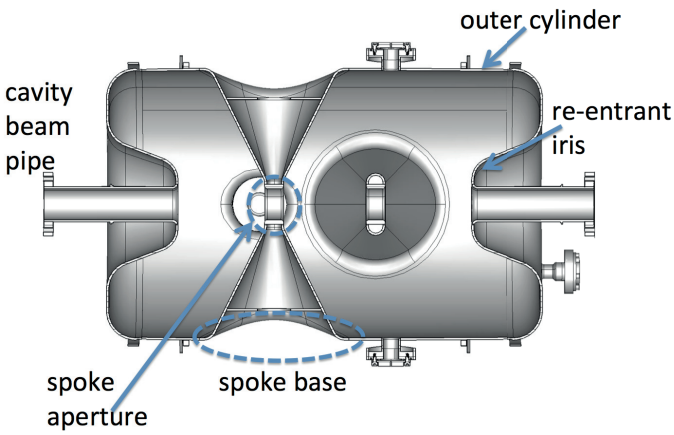

Figure 3.6. Cross section of the ESS double-spoke cavity

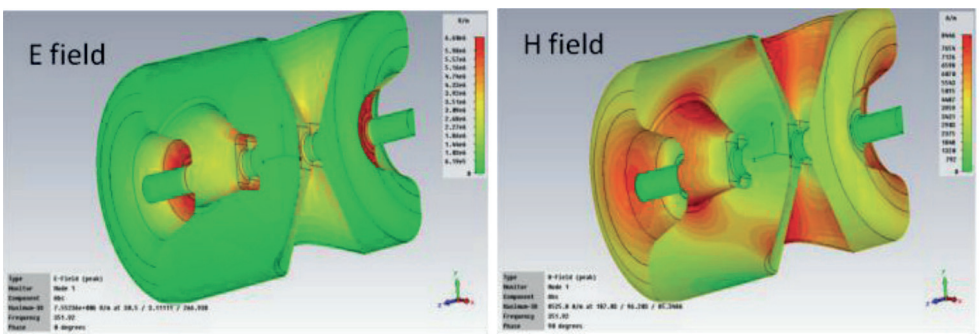

Figure 3.7. EM field simulation result for the ESS spoke cavity (Left) *E*-field (Right) H-field [38]

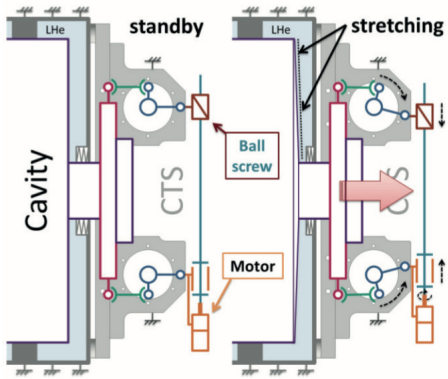

Figure 3.8. Schematic view of the spoke cavity frequency tuner for pulling the cavity from the beam pipe side **[40]**

Table 3.2.
ESS spoke cavity tuning system parametrs **[12]**

Parameter	Value
Cavity sensitivity (kHz/mm)	110
Cavity RF bandwidth (Hz)	1355
Lorentz force detuning (Hz)	400
Cavity stiffness (kN/mm)	20
Slow tuning range (kHz)	170
Fast tuning range (Hz)	675

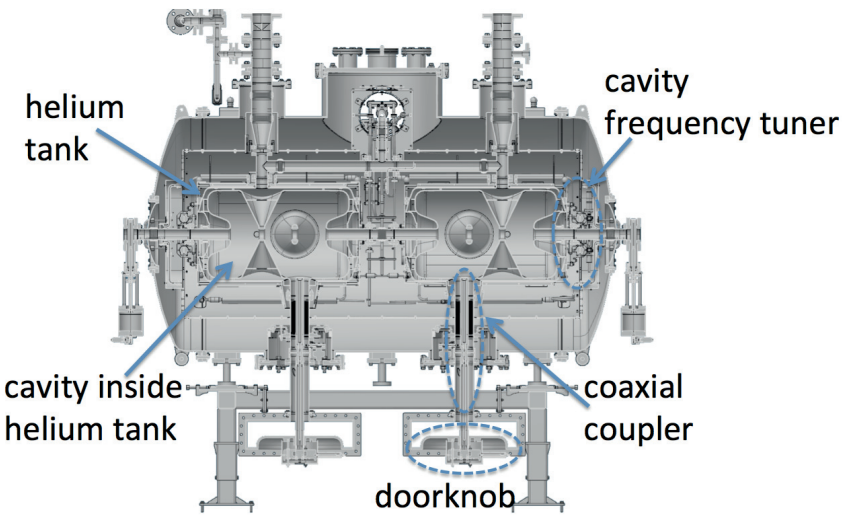

Figure 3.9. Cross section view of the ESS spoke cryomodule [12]

3.2.3 Elliptical cavities

Using the elliptical SRF cavity for medium energy particles with β<0.6 reduces the cell length and results in a cavity with almost vertical walls, which the makes mechanical structure of the cavity unstable. **Figure 3.10** shows *E*-field and H-field distributions of the ESS medium beta cavity as a typical example of an elliptical cavity. As illustrated, E_{peak} distribution is on cavity irises and H_{peak} distribution is on the cavity equator. In an elliptical cavity, a power coupler port is placed on the cavity beam pipe. The proper coupling condition between the coupler antenna and the cavity is achieved based on the nominal beam current, which is accelerated by the cavity.

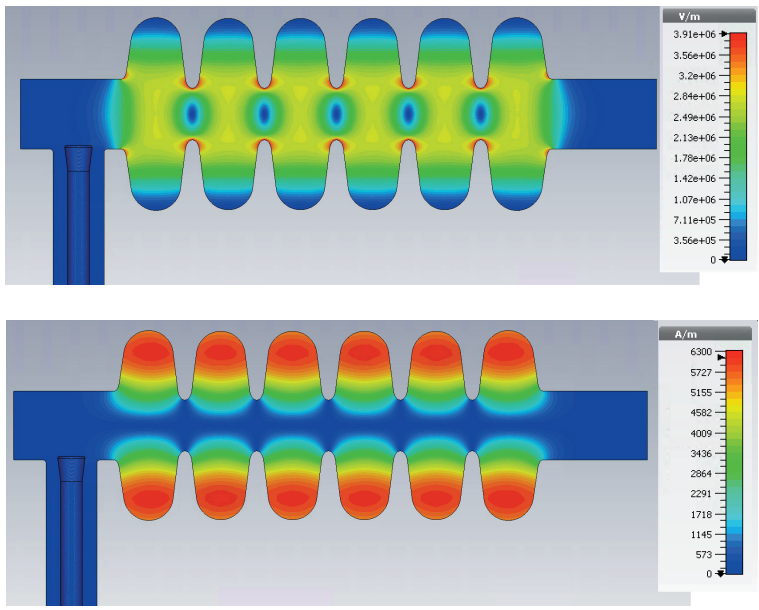

Figure 3.10. CST EM simulation result for the medium beta cavity π-mode. (Top) *E*-field (Bottom) H-field

Figure 3.11 (left) illustrates a 3D layout model of a medium beta cavity cryomodule. The medium beta cavity assembly has a helium tank and magnetic shielding. The cavity power coupler and the doorknob inject RF power from the bottom into the cavity. **Figure 3.11** (right) illustrates a fundamental power coupler installation on the medium beta cavity coupler port. When there is no beam to pass through the cavity (vertical test), applying the fundamental power coupler results in a reflection of most of the RF power. For efficiency considerations, a probe antenna design is necessary

for the vertical test. **Figure 3.12** (left) illustrates a probe antenna for the medium beta cavity vertical tests. **Figure 3.12** (right) shows the pickup antenna, which monitors the *E*-field in the cavity. The same pickup is implemented for both vertical and cryomodule tests. All these antennas have capacitive coupling to the cavity.

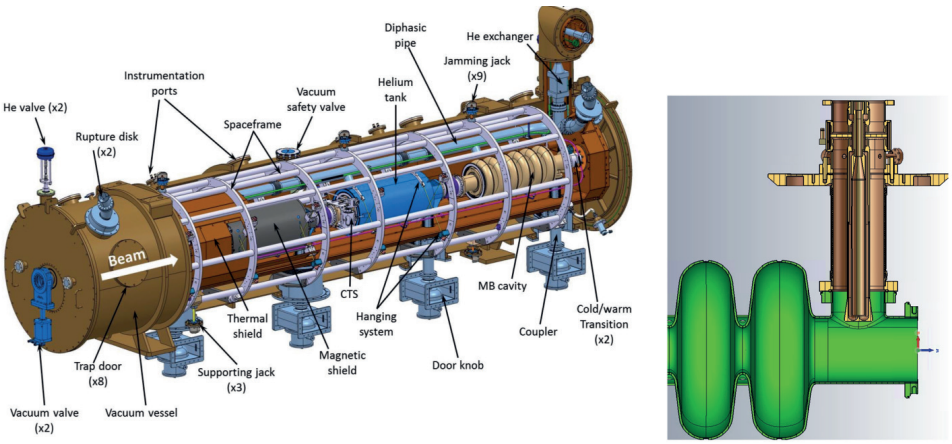

Figure 3.11. (Left) 3D layout model of the medium beta cavity cryomodule (Right) The fundamental power coupler installed on the medium beta cavity, coupler port

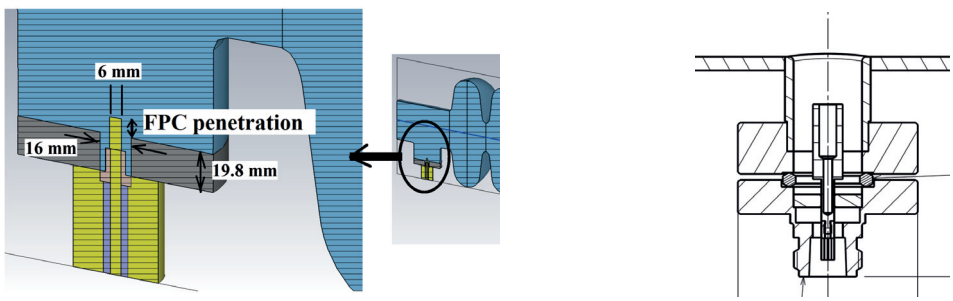

Figure 3.12. (Left) Schematic view of the probe coupler on the cavity coupler port for vertical test. (right) The cavity pickup antenna.

Table 3.3 compares some of designs for elliptical cavities. It provides a quantitative overview for the main RF operational parameters in an elliptical cavity. Determining the nominal accelerating gradient for an SRF cavity is based on maximum E_{peak} and H_{peak}. E_{peak} is determined by practical considerations. The theoretical limit for the E_{peak} in a niobium cavity at 2 K is

equivalent to 220 mT magnetic superheating field (H_{sh})[8] on the cavity surface. This is a field that the niobium cavity superconductivity breaks in ideal conditions. In practice, superconductivity is lost for a lower surface magnetic field due to cavity surface heating. The surface heating may be caused by sites on the inside surface of the cavity with a sharp projection or jagged surface and exterior material in the niobium. Surface treatment quality and estimation of the onset of the exponential increase of field emission (explained in detail in chapter 6) are practical considerations in this case.

Table 3.3.
RF properties of some of the elliptical SRF cavities

Project	Frequency (MHz)	β	E_{acc} (MV/m)	E_{peak}/E_{acc}	B_{peak}/E_{acc}	Reference
ESS	704.4	0.67	16.7	2.55	4.95	**[12]**
ESS	704.4	0.86	18	2.2	4.3	**[12]**
PIP-II	650	0.64	15.9	2.47	4.69	[95]
PIP-II	650	0.97	17.8	2.18	4.1	[95]
Trasco	704.4	0.47		3.57	5.88	[63]
TESLA	1300	1	25	2	4.26	**[16]**
MYRRHA	704.4	0.705	14.3	3.3	5.5	[44]
MYRRHA	704.4	0.51	10.7	2.5	4.6	[44]
SNS	805	0.61	10.1	2.71	5.72	[65]
SNS	805	0.81	21.5	2.19	4.72	[65]

In general, there are many trade-offs between design requirements. Some issues require reiterations between SRF and mechanical properties based on accelerator machine requirements. For instance, the beam aperture size is decided based on the beam dynamic aperture, vacuum calculations, cell-to-cell coupling, and peak surface fields.

Stored energy and power loss in a cavity are proportional to its volume and surface area, respectively. The linear length of an elliptical cavity depends on the beam's relative velocity (β). Thus, a linear decrease in the cavity stored energy is expected due to a linear decrease in the β value. Whereas power loss in an elliptical cavity mostly depends on the cavity end-cups, power loss weakly depends on the cavity length. The R/Q changes (per cell) in an elliptical cavity versus β are based on:

[8] - Magnetic superheating field (H_{sh}) is the critical magnetic field of an RF superconductor

$$\frac{R}{Q} = \frac{(E_{acc}L)^2}{\omega U}, \tag{3. 22}$$

even though both L (cavity length) and U (stored energy) are linearly proportional to β. However, considering the illustrated increase in E_{peak}/E_{acc} due to the β decrease in **Figure 3.13**, a decrease in E_{acc} is expected with lower β. Therefore, reducting the β value will result instead in a higher reduction in R/Q than a linear reduction.

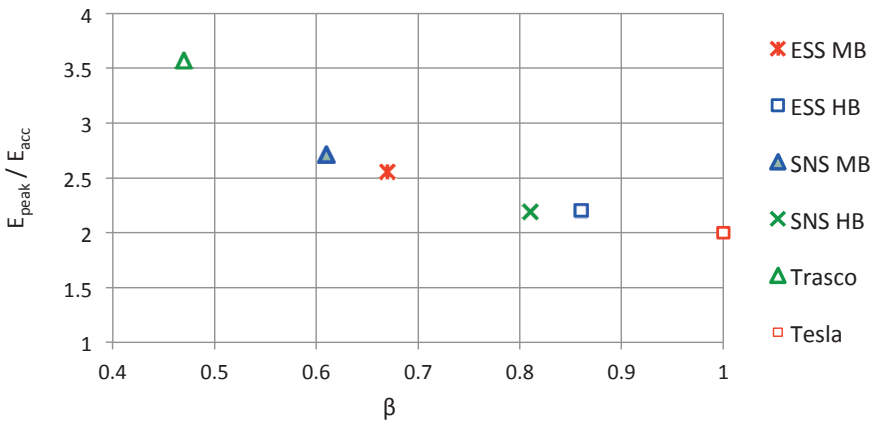

Figure 3.13 Comparison of E_{peak} / E_{acc} versus β for some existing SRF cavities.

Q-degradation and cures

Q_0 and E_{acc} are two significant characteristics of an SRF cavity. In an ideal situation it is expected to have constant Q_0 versus E_{acc} increase until the cavity reaches H_{sh}. In practice, multipacting, thermal breakdown, field emission and hydrogen Q-disease are observed challenges in raising the accelerating gradient of an SRF cavity. Multipacting, which occurs in discrete field levels, was solved by the invention of a spherical geometry for the equator region, which varies the H-field along the spherical surface and the very low E-field in the equator. Current capabilities in the cavity material preparation, cavity fabrication and surface treatment make it possible to prevent the inclusion of foreign material on the cavity surface. This limits and prevents thermal breakdown for low E_{acc}. Assembling the cavity in a clean room and high-pressure rinsing have also reduced field emission rates significantly. However, accidental contamination may happen during cavity assembly. Field emission and multipacting due to such contamination will be

resolved by RF conditioning, which suppresses the effect of residual field emitters by increasing the *E*-field. The increase in surface *E*-field increases the emission current and will destroy the emitter.

In cavity surface treatment, hydrogen is diffused inside the niobium bulk. The hydrogen precipitations (in the RF surface) into a lossy hydride cause a residual loss, which results in the cavity quench. This is called Q disease. The best cure for a cavity Q disease is hydrogen degas from niobium by baking the cavity at 800°C for a couple of hours in a vacuum (better than 10^{-6} Torr), or baking at 600°C for 10h (if the decrease in yield strength from 800°C bake cannot be tolerated) [29].

3.3 Materials other than bulk niobium

Niobium's critical temperature (T_c) is 9.2 K. It has the highest critical temperature and magnetic field (220 mT) of all pure metals. Its mechanical properties enable it to tolerate mechanical tension and pressure in the cavity fabrication procedure. These properties make bulk niobium a suitable material choice for the SRF cavity fabrication. In the past 50 years, cavity fabrication with bulk niobium has continuously been improved and the accelerating gradient increased. However, the SRF cavity with bulk niobium is approaching its physical limits for the high gradient. Innovation is essential if further improvements are to be made. One way is to use other forms of niobium or other superconducting materials with higher T_c and H_c. A higher H_c will result in higher E_{acc} (fewer cavities), and higher T_c will reduce surface loss[9] (cheaper cryogenics). Furthermore a higher T_c may result in an operation temperature higher than 2 K or 4 K. Operating the SRF cavity at higher temperature will greatly simplify the cavity cryoplant. For instance, a cryogenic operation Carnot efficiency of 4.2 K with atmospheric liquid helium is 60% higher than 2 K operation [45]. Both 4 K and 2 K are typical operation temperatures for SRF cavities the in accelerator facilities. Due to helium boiling temperature at 4.2 K, operating the SRF cavity at 2 K results in higher frequency stability for the cavity operation, thus the cryogenic system required is more expensive.

[9] - Surface resistance dependence on T_c is explained in 4.3.3 section

Table 3.4 compares the main superconducting characteristics of NbN, NbTiN and Nb_3Sn with the bulk niobium. Applying a new material to the SRF cavity fabrication requires considerations such as surface resistance, critical magnetic field, superconducting gap symmetry and stability against mechanical tension. Materials like H_2S with T_c = 200 K, applicable at 155 GPa pressure, are not suitable for the SRF cavity application. In the following, the niobium thin film sputtering on a copper cavity base (Nb-Cu) and Nb_3Sn layer development on the bulk niobium cavity base are assessed. Both of them are promising alternatives to overcoming some of limitations of the bulk niobium cavity.

Table 3.4.
Parameter comparison of some of superconducting materials with bulk Nb **[48]**.

Material	T_c (K)	ρ_n ($\mu\Omega$ cm)	$H_c(0)$ (T)	λ (nm)	Δ (meV)	ξ (nm)
Nb	9.23	2	0.2	40	1.5	35
NbN	16.2	70	0.23	200–350	2.6	3–5
NbTiN	17.3	35	n.a.	150–200	2.8	5
Nb_3Sn	18	8–20	0.54	80–100	3.1	4

Niobium thin film on a copper base

Skin depth in the SRF cavity with bulk niobium is roughly 40nm, and the SRF properties of the cavity are determined through the properties of this thin layer at the surface. Niobium heat conductivity at 4.2 K is roughly 75 W/m, whereas copper heat conductivity is roughly 300–2000 W/m [48]. Thus, it would seem logical to provide superconductivity in the SRF cavity through a thin film coated on another metal with better heat conductivity and a lower cost, such as copper. Moreover, the reasons for using the niobium thin film on the copper instead of bulk niobium are better thermal stability, lower cost and less sensitivity to trapped magnetic flux.

For the heat generated due to defects on the cavity surface, the higher heat conductivity of the copper will better transfer the heat to the helium bath. Better thermal conductivity means wall thickness can be increased, which results in higher mechanical stability. Moreover the cost of copper is roughly 10% that of niobium. The surface resistance of the SRF cavity with thin film niobium is almost independent of the earth's magnetic field due to a low electron mean free path and high upper critical magnetic field (H_{c2}) [75]. Therefore, the cryomodule will require less magnetic shielding.

A cylindrical magnetron is used to sputter a thin film niobium of on the copper cavity base. **Figure 3.14** is a schematic view of typical niobium thin film coating. A stable current is established between the niobium cylinder (cathode) and the grounded cavity wall, also a permanent magnet is placed inside the cavity to increase ionization efficiency. A low-pressure noble gas (Ar, Kr, Xe or Ne) sputters the niobium atoms from the cathode and projects the niobium atoms on the cavity wall [51]. Thus, atoms of the noble gas will be embedded in the niobium film. The optimal niobium thin film thickness is roughly 2–4 μm.

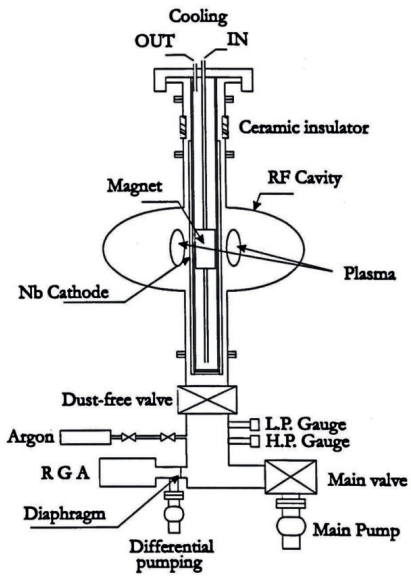

Figure 3.14. Schematic view for niobium thin film coating in a single cell cavity by cylindrical magnetron sputtering [51]

This procedure of thin film growth prevents exterior material from being included in the cavity RF surface, except for the inert gas that is trapped. Therefore, the SRF cavity will not be quenched because of normal conducting defects in the superconductor region. The surface roughness in the cavities with the sputtered niobium thin film mainly depends on the roughness of the base substrate [48]. It is critical to have a smooth, clean-coated surface without pores.

Nb-Cu cavities still cannot compete with the bulk niobium cavities for high gradient applications as they are limited to 10 MV/m accelerating gradient. A

low field Q slope is the main obstacle to increasing the accelerating gradient. Ongoing research is seeking to understand the low field Q slope and develop higher-quality thin film niobium. In this regard thin film growth using an electron cyclotron resonance (ECR) deposition is a promising alternative to the magnetron sputtering method. Electron cyclotron resonance uses electron beam evaporation to provide a high flux of ionized niobium atoms through the ECR process. A magnetic field steers the ionized niobium atoms. The reason for applying the ECR deposition method is to increase the condensation energy of the niobium ions. In niobium coating by ECR rather than magnetron deposition, there is no carrier gas, which prevents voids from forming in the thin film. The niobium thin film developed by the ECR has a dense grain boundary and good adhesion to the substrate. Surface resistance for the niobium thin films developed by ECR and by magnetron sputtering has been compared in [50]. The surface resistance is measured for both thin films as a function of a 400 MHz magnetic field increase at 2.5 K and 4 K. For both 2.5 K and 4 K, the surface resistance of the sample prepared by ECR was lower.

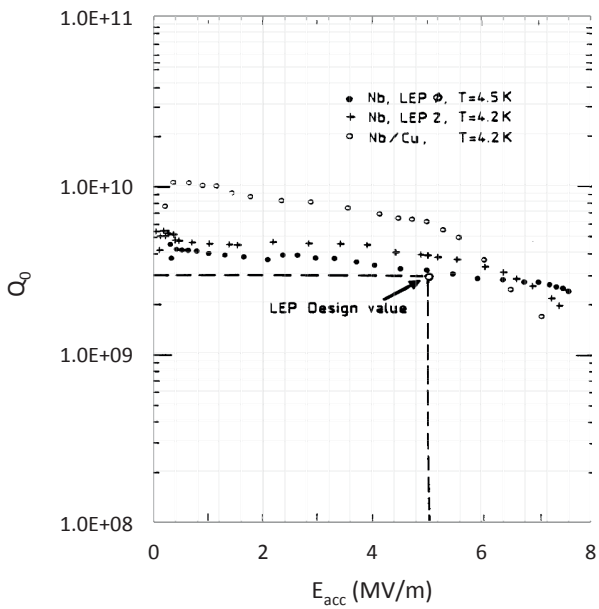

Figure 3.15. Q_0 versus E_{acc} performance for the LEP-II four-cell cavity [48]

Thin film niobium sputtering on the copper base is implemented for the ALPI linac at INFN-LNL [53], for LEP-II, LHC, and HI*E*-ISOLDE at CERN [54]. The LEP-II is a four-cell cavity that has been operated from 1989 to 2000. Its RF frequency, accelerating gradient and operation temperature were 352 MHz, 7 MV/m and 4 K, respectively. **Figure 3.15** shows its Q_0 versus E_{acc}. Furthermore the single-cell LHC cavity RF frequency and accelerating gradient are 400 MHz and 14 MV/m at 2.5 K respectively. **Figure 3.16** shows its performance for 2.5 K and 4.5 K operating temperatures. Besides ALPI and HIE-ISOLDE linacs use quarter wave resonators.

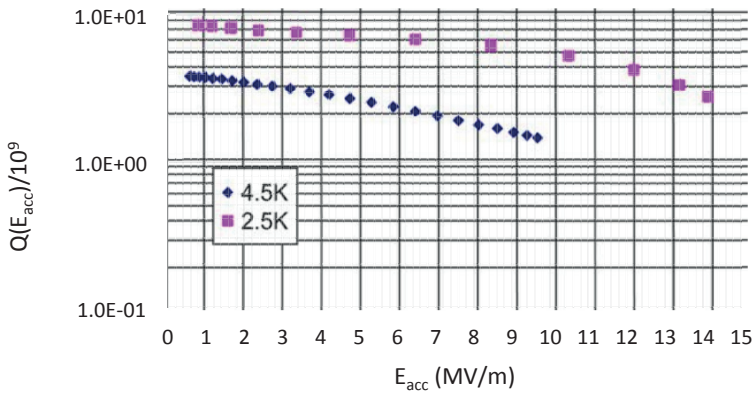

Figure 3.16. Q_0 versus E_{acc} perforance of the 400 MHz LHC cavity at 2.5 K and 4.5 K [48]

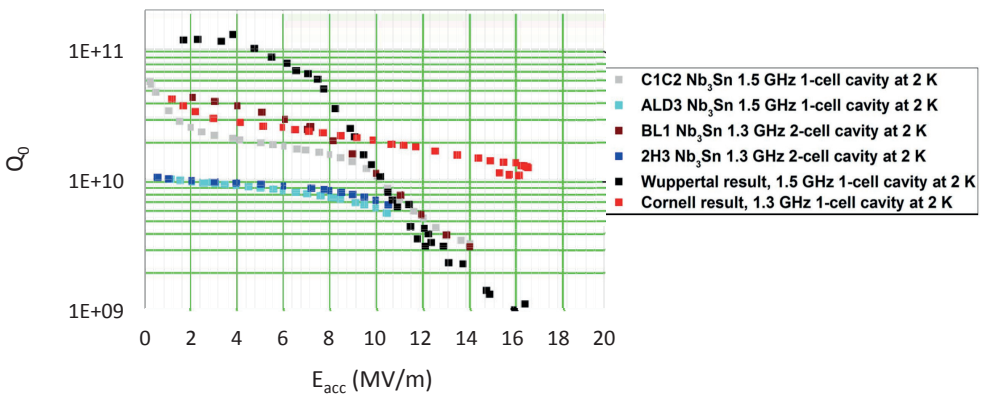

Figure 3.17. Q_0 versus E_{acc} measurement result comparison for SRF cavities with Nb_3Sn thin film. (C1C2, ALD3, BL1 and 2H3 cavities are developed by Jefferson Lab) [47]

Nb_3Sn thin film on a niobium base

The superheating magnetic field (B_{sh}) and T_c of the Nb_3Sn are roughly twice that of niobium. The Nb_3Sn is mechanically brittle and is a poor thermal conductor. Depositing the Nb_3Sn layer on a metal with good thermal conductivity, which is sustainable for cavity fabrication, is the best alternative for bulk niobium.

Initial SRF cavities with Nb_3Sn thin layer coating on a niobium surface (with the shape and frequency of conventional SRF cavities) had a higher low-field Q_0 than exiting cavities with bulk niobium had. On the other hand, their high Q-slope onset was on E_{acc}=5 MV/m [46]. The Nb_3Sn thin layer coating was applied using tin vapor diffusion on a cavity with bulk niobium. The high Q slope for low E_{acc} was suppressed by providing a uniform coating layer and reducing areas with low tin content on the RF layer [47]. Measurement results for the SRF cavities with Nb_3Sn thin layer coating are promising, but certain practical issues, such as sufficient coating thickness and uniform coating thickness, need to be resolved before putting such cavities in an accelerator machine. An SRF cavity has a complex shape for coating, which make a uniform coating challenging. The coating layer must be sufficiently thick to screen the base metal from the RF field. **Figure 3.17** compares the Q_0 vs. E_{acc} of an SRF cavity developed in Cornel with Nb_3Sn thin film with earlier developments.

4 Design, fabrication and test of the ESS medium beta cavity

This chapter explains the design, fabrication, surface treatment and RF measurement for the ESS medium beta cavity. In the medium beta cavity design section, the main issues related to a multicell elliptical SRF cavity geometry design are briefly discussed. Moreover, the geometry error effect of the cavity cells on pickup Q_{ext} is studied. In addition, the cavity field flatness variation effect on the coupler Q_{ext} value is assessed. Further, the fabrication process of an elliptical multicell cavity is explained, followed by a description of the evolution of the cavity geometry from a half-cell to a six-cell cavity. Then, cavity field flatness tuning and surface treatment are explained.

The cavity measurement section describes the testing methodology for the medium beta cavity. Moreover, the RF measurement results for the cavity are reported and discussed. Finally, a measurement uncertainty for RF measurement in a vertical test set up is studied, including possible sources of systematic errors in RF measurement.

4.1 MB cavity design

To optimize cavity design, it is essential to use correct geometry parameterization. The optimal design needs to meet the requirements of the RF and mechanical parameters of the cavity, while also considering fabrication limitations. These requirements include the effect of the cavity on a beam, electromagnetic field specifications and the geometric boundary conditions. For the SRF cavities, boundary conditions include, but are not limited to, the tuner design, the helium bath design, the cryomodule, the fundamental power coupler and higher order mode coupler design. Including these considerations into the cavity design will result in an iterative process.

For the ESS linac, medium beta cavities are designed by INFN-LASA. The cavity needs to be compatible with the existing design of the cryomodule, i.e. to be plug compatible with the cryomodule design.

A multicell elliptical cavity design starts with a half-cell design. The half-cells are characterized by seven geometrical parameters, shown in **Figure 4.1**. These parameters are:

- Half-cell radius (D),
- Iris radius (R_{iris}),
- Equator ellipse ratio (R=B/A),
- Iris ellipse ratio (r=b/a),
- Half-cell length (L),
- Sidewall inclination (α) and
- Sidewall distance to iris plane (d).

The best design is achievable by optimizing the RF and mechanical characteristics of the cavity. The first step is a 2D design of the cavity, which could be done using tools such as Superfish [57] and BuildCavity [58]. When the parameters in the 2D design converge, the 3D electromagnetic design can start, using software such as CST [59] and HFSS [60].

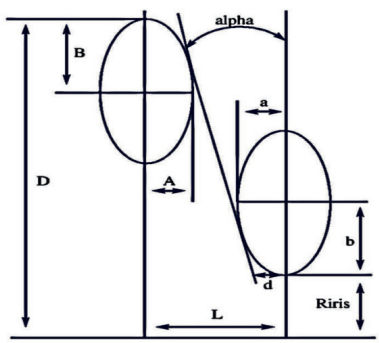

Figure 4.1 The half-cell geometry parametrization for the elliptical cavity design

The main considerations in the cavity half-cell design are:

- Large cell-to-cell coupling factor (k_{cc})
- Equator ellipse ratio equal to one (R=B/A)

- Tuning iris ellipse ratio (r=b/a) for lowest E_{peak}/E_{acc}
- Using the cell radius for half-cell π-mode frequency tuning
- Using the sidewall distance to the iris plane to provide balance between E_{peak} and k_{cc}.
- Designing the half-cell length based on the π-mode half wavelength and relative velocity of the particle to the speed of light
- Considering the beam pipe effect in the end-half-cell design
- Tuning the end-half-cell on the main coupler side for the desired EM coupling level with the coupler

Setting the equator ellipse ratio to one provides spherical geometry on the cavity equator and limits multipacting. For the ESS medium beta cavity design, the initial starting point of the optimization benefited from the criteria applied to the TRASCO cavity, which were later also used for the PIP-II LB650 [62]-[64] cavity design. Table 4.1 illustrates the k_{cc} comparison for the ESS, SNS [65] and TESLA [66] cavities. For the TESLA and SNS cavities, it is preferable to have a k_{cc} higher than 1.5% to reduce the cavity π-mode field flatness sensitivity to frequency errors on the cavity cells [67]. Field flatness sensitivity is defined as:

$$\frac{N^2}{\beta\, k_{cc}}, \tag{4.1}$$

where N is the number of cells and β is the ratio of the particle velocity to the speed of light. The iris radius is set at 50 mm in the medium beta cavity design to provide proper cell-to-cell coupling (k_{cc}>1.5%). Based on the specifications, R_{iris} needs to be larger than 47 mm; at 50 mm instead of 47 mm, the cell-to-cell coupling increases by 26% and the mode separation between π and 5 π/6 increases by 30%. In contrast, an increase in R_{iris} will reduce the R/Q of the π-mode by 7% and increase the E_{peak}/E_{acc} by 6%. These drawbacks are negligible compared with the benefits.

Table 4.1.
Cell-to-cell coupling comparison for three multicell elliptical cavities **[64]**

Cavity	Number of cells	β	k_{cc}
ESS medium beta	6	0.67	1.55
SNS medium beta	6	0.61	1.52
TESLA	9	1	1.87

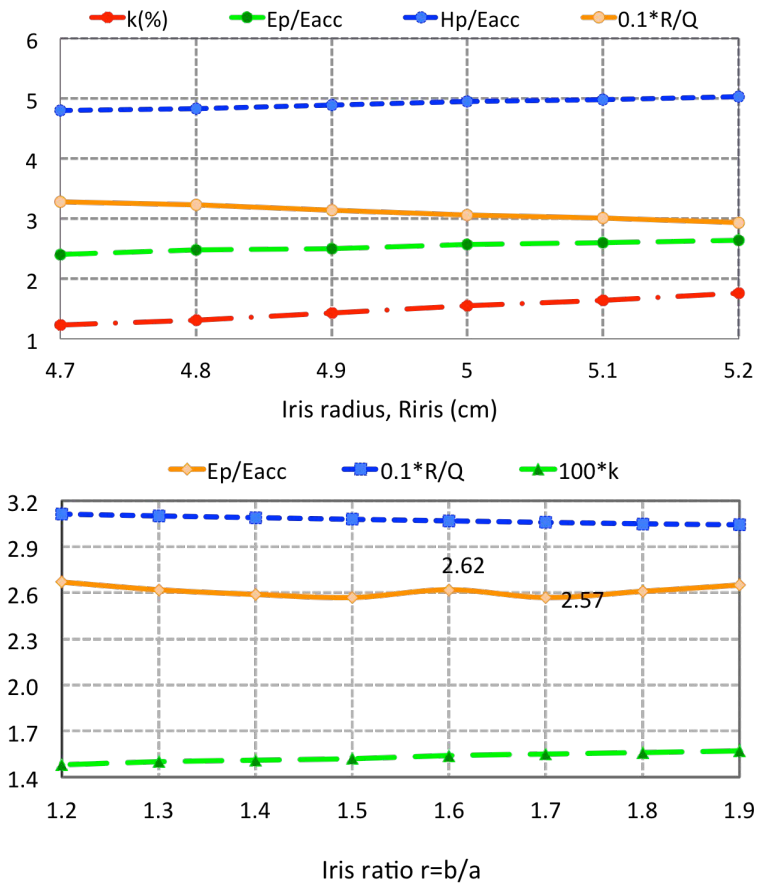

Figure 4.2 Inner HC (Up) iris radius effect on, (Down) iris ellipse ratio effect on, cavity RF parameters **[68]**

Figure 4.2 (Up) shows the effect of R_{iris} change on k_{cc}, E_{peak}/E_{acc}, H_{peak}/E_{acc} and R/Q. A higher R_{iris} is also advantageous because higher order modes (HOMs) are less likely to be trapped in the middle cells of the cavity. The iris ellipse ratio is explored to minimize E_{peak}/E_{acc}. **Figure 4.2** (Down) illustrates E_{peak}/E_{acc}, k_{cc} and the R/Q versus iris ellipse ratio. Setting the iris ellipse ratio to 1.7 minimizes E_{peak} and maintains k_{cc} at 1.55%. Moreover decreasing the half-cell sidewall angle increases the electric volume part of the half-cell and slightly decreases E_{peak}. This also negatively affects the chemical etching and high pressure rinsing of the cavity. Setting the sidewall angle at less than 6 degrees will further complicate the surface treatment of the cavity. For the

ESS medium beta cavities, the sidewall angle for the inner-half-cell and end-half-cell are 7 and 8.4 degrees, respectively.

Generally, multicell elliptical cavities are composed of two different half-cells: end-half-cell and inner-half-cell. The inner-half-cells form inner cells of the cavity and the end-half-cell connects the beam pipe to the inner cells. Nevertheless in the ESS medium beta cavity, there are three different half-cells: inner-half-cell, pen-half-cell and end-half-cell. The pen-half-cell stays between the inner-half-cell and the end-half-cell. The pen-half-cell provides a spherical equator for the first and last cells of the cavity. Therefore, the diameter of the end-half-cell is slightly larger than the inner-half-cell to provide the spherical shape without reducing the sidewall angle.

Table 4.2.
Nominal RF parameters of the medium beta cavity

Parameters	value
Geometric beta	0.67
Frequency (MHz)	704.42
Acceleration length (m)	0.855
Cell-to-cell coupling	1.55
Pi–5pi/6 separation (MHz)	0.7
G (Ω)	198.8
Optimum beta (β_{opt})	0.705
Max *R/Q at* β_{opt}	374
E_{peak}/E_{acc}	2.55
E_{peak} *(MV/m)*	42.6
B_{peak}/E_{acc} (mT/MV/m)	4.95
Q_0 at nominal gradient	> 5E9
Q_{ext}	7.8E5

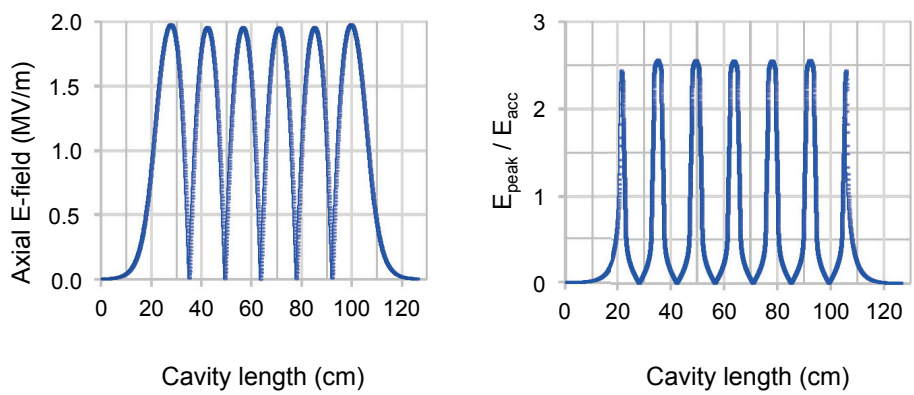

Figure 4.3. Superfish simulation result for (Up) *E*-field on cavity axis. (Down) Ratio of E_{peak} over E_{acc} surface

Table 4.2 illustrates the main RF parameters of the medium beta cavity. Furthermore the *E*-field on the cavity axis and E_{peak}/E_{acc} versus the cavity axis length are demonstrated in **Figure 4.3**. The cavity design assumes 100% field flatness to provide uniform energy gain per cell and minimize E_{peak} over the cavity surface. The maximum values of the E_{peak} are on the cavity irises.

4.1.1 Q_{ext} of the coupler and pickup ports

Depending on the type of the cavity test (vertical or cryomodule), there are two different antennas for the cavity coupler port: a probe antenna and a fundamental power coupler (FPC). Before cavity integration in the cryomodule, RF is measured with a probe antenna. After cavity integration in the cryomodule, RF is measured through the fundamental power coupler. Two prototypes of the ESS medium beta cavity were fabricated and measured before serial production of the medium beta cavities: one with fine grain, the other with large grain. From this point on, the fine-grain prototype cavity will be referred to as MB001.

The Q_{ext} of the coupler port explains the amount of coupling between the cavity and the coupler antenna. The Q_{ext} calculation for this port is based on nominal beam current. Ideally, this value is adjusted for no power reflection from the coupler port at the nominal beam current path through the cavity. From [69], the Q_{ext} value for the FPC in an SRF cavity is given by:

$$Q_{ext} = \frac{V_{acc}}{\frac{R}{Q} I_b \cos(\varphi_s)}, \tag{4.2}$$

where φ_s and I_b are the synchronous phase and beam current, respectively. The distance between the fundamental power coupler antenna tip to the cavity axis tunes the coupler Q_{ext}. For the ESS medium beta cavity, this resulted in determining the Q_{ext} of the fundamental power coupler between $5.9 \cdot 10^5$ and $8 \cdot 10^5$. **Figure 4.4** shows the Q_{ext} change of the fundamental power coupler versus the distance of the coupler antenna tip to the cavity axis. There is higher coupling (less Q_{ext}) for the longer antenna length. Based on the ESS cryomodule interface documents, the distance between the fundamental power coupler antenna tip to the cavity axis is 61.26 mm, corresponding to $Q_{ext} = 7.8 \cdot 10^5$.

In a cavity, the pickup antenna Q_{ext} value determines the amount of power coupled out of the cavity to monitor the cavity field with low-level RF

(LLRF) electronics. For the medium beta cavity, a pickup antenna with 7 mm diameter and 17.7 mm length would provide Q_{ext} =2.4·10^{11}. **Figure 4.5** shows the Q_{ext} change versus the antenna length in the medium beta cavity for the pickup antenna.

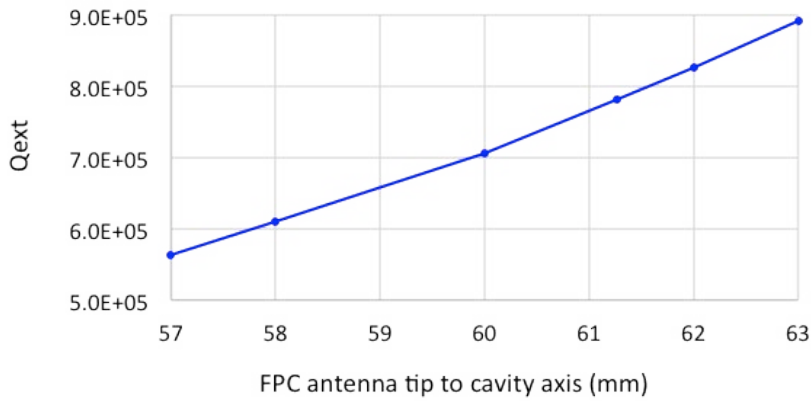

Figure 4.4. The Q_{ext} change for the fundamental power coupler versus antenna tip distance from the cavity axis

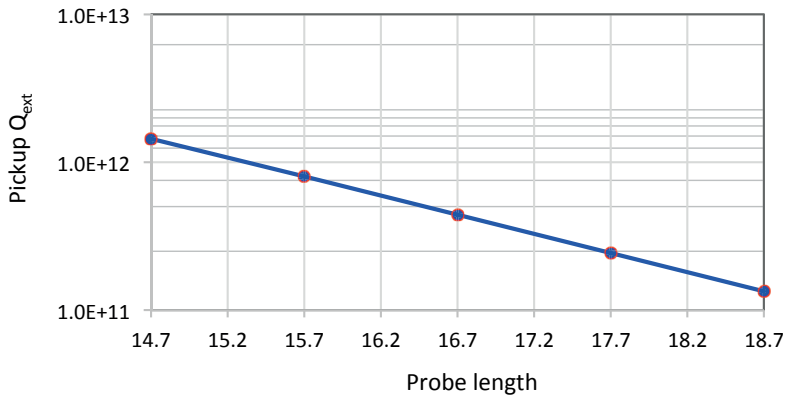

Figure 4.5. Q_{ext} change for the pickup antenna versus the antenna length

Table 4.3.
Simulation and measurement results for the Q_{ext} of the coupler and the pickup antennas

	Simulation	Measurement
Fundamental power coupler	7.8·10^5	7.37·10^5
Probe antenna (vertical test)	9·10^9	6.6·10^9
Pickup antenna	2.4·10^{11}	9·10^{10}

A comparison between the simulation and the measurement results (both vertical and cryomodule tests) for the coupler and pickup antennas is presented in Table 4.3. For the fundamental power coupler, there is very good correspondence between the simulation and measurement results. There is a 25% difference between the simulation and measurement results for the coupler probe in the vertical test. For the pickup antenna there is a big gap between the simulation and measurement results.

Pickup Q_{ext} error study

To find the source of such a big difference in the pickup Q_{ext} measurement, the sensitivity of the pickup Q_{ext} to the cavity geometry errors is assessed through a systematic error study. The six cells of the medium beta cavity resulted in a large degree of freedom in the geometry error study. For simplicity it is critical to introduce certain procedures for the geometry error study. In the medium beta cavity fabrication process, the field flatness-tuning machine[10] compensates for geometrical errors by length tuning the cells for the cavity acceleration mode.

Due to the influence of geometry of the cells on the field flatness, its effect in the pickup Q_{ext} error study is included. The error study is conducted by inserting errors in the ellipse radiuses of the equator and iris (A, B, a, b), R_{iris} and D. (introduced in **Figure 4.1**). The following describes the main steps of the error study for the equator radius of the cell-1[11] on the pickup Q_{ext}:

- First, inser an error in the equator radius of cell-1. The cell-1 π-mode frequency will change due to this error.
- Tune the cell-1 π-mode frequency to its nominal value by tuning the length
- Calculate pickup Q_{ext} and field flatness of the medium beta cavity with the updates in cell-1 geometry
- Repeat the same procedure with similar equator radius error on cell-2 and cell-3. Due to the symmetry in geometry and π-mode EM field, we only need to study three cells (half of the cavity)

The results showed that the deviation in the pickup Q_{ext} value from its nominal design value due to cavity geometrical errors could be due to:

[10] - Field flatness tuning is explained in section 4.2.2

[11] - Cell-1 is the cell adjacent to the pickup port

- Mechanical errors in the cavity cells
- Mechanical errors on the cavity beam pipe on the pickup side (including its attachments, such as the pickup port and pickup antenna)

Preliminary results showed that a large error in the pickup Q_{ext} measurement comes from mechanical errors on the beam pipe (pickup side). The effect of cells geometry errors on the cavity axial E-field will be compensated by field flatness tuning. **Figure 4.6** (left) and **Figure 4.7** (left) show the results of the error study for the Q_{ext} change by a 2 mm error in the equator radius and iris radius, respectively. The field flatness changes for both cases are illustrated in **Figure 4.6** (right) and **Figure 4.7** (right). These results indicate that a 1 mm change in the iris and 2 mm in equator radius values in the different cavity cells results in less than 10% variation in the Q_{ext}.

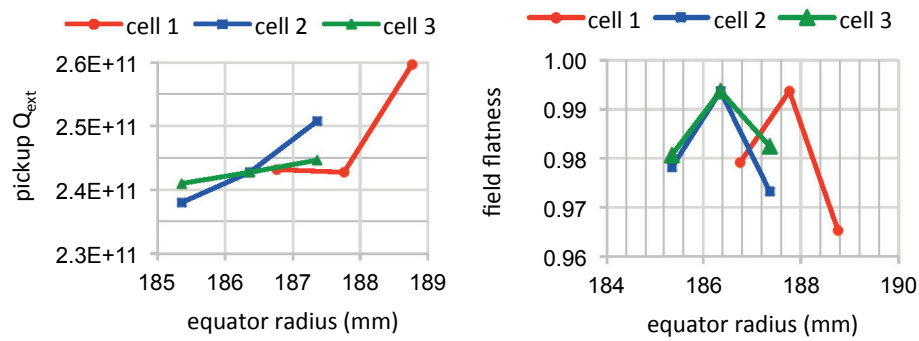

Figure 4.6. (Left) The pickup Q_{ext} variation based on equator radius change, (Right) field flatness check for the equator radius error study

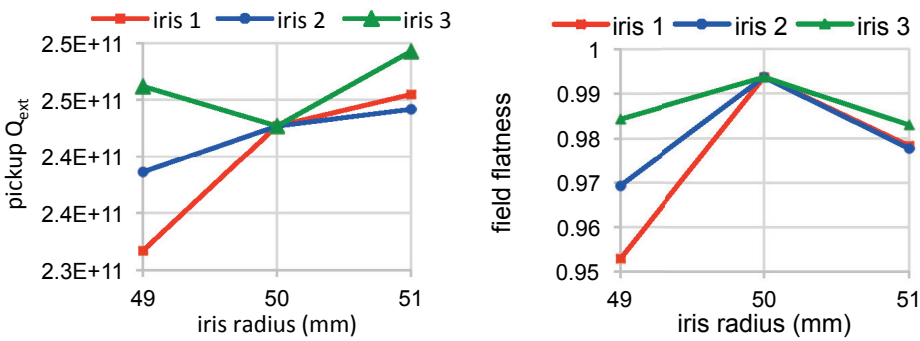

Figure 4.7. Qext variation based on (Left) iris radius change, (Right) field flatness change

Figure 4.5 and **Figure 4.8** show the pickup Q_{ext} change as a result of geometrical errors on the beam pipe side. The most significant effect is related to errors in the pickup antenna. As illustrated, the antenna length and diameter effects are roughly 90% and 25% per millimeter, respectively. Meanwhile, Q_{ext} change due to the length error for a distance between middle of the pickup port and the end-half-cell plane is roughly 10% per millimeter.

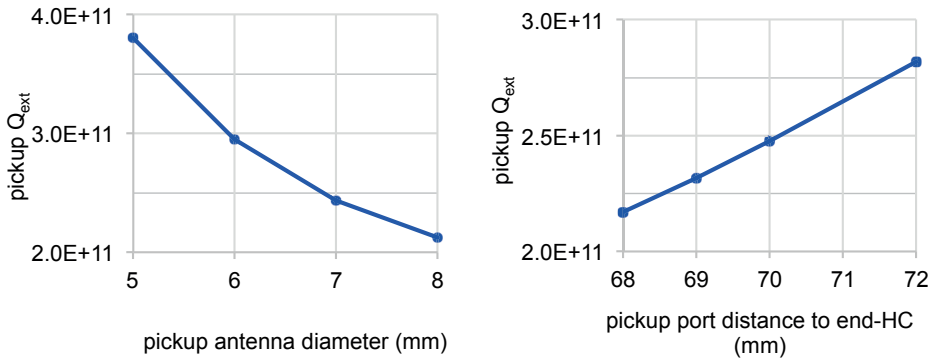

Figure 4.8. Pickup antenna Qext change based on (Left) pickup antenna diameter, (Right) distance between end-HC to pickup port

4.1.2 Field flatness variation effect on coupler Q_{ext}

In the medium beta cavity, the field flatness correction and the vertical test are managed with a probe antenna. The Q_{ext} measurement for the fundamental power coupler is only available after the cavity is integrated into the cryomodule. In the ESS medium beta cavity, the Q_{ext} of the fundamental power coupler is close to its upper limit. Given the importance of this Q_{ext} on the power reflection, it is critical to have some estimation of the Q_{ext} variation.

The medium beta cavity has six resonators (six cells) coupled to each other. Field flatness is 100% in the cavity design if the coupling between the cells is correct. However, there are unavoidable geometrical errors in the cavity fabrication, which break the proper coupling between the cells and reduce the field flatness. Field flatness is tuned after cavity fabrication to provide levels higher than 93% (specified by the ESS).

In a multicell elliptical cavity, coupling between the fundamental power coupler antenna and the cavity cells determines the Q_{ext} of the coupler. Consequently changing the field flatness of the cavity cells or a geometrical

change in the coupler side will change the Q_{ext}. The geometrical change in the coupler side results by a change in the beam pipe geometry, the coupler port, and the gap distance between the antenna tip and the cavity axis. By considering no geometrical error in the coupler side, variations in field flatness (due to the geometry error in cells) will be the source of the Q_{ext} change.

Studying the effect of the cavity field flatness variation on the Q_{ext} of the fundamental power coupler will deliver a typical boundary for the Q_{ext} variation. This study uses a cavity simulation in the CST. For simplicity, only four field flatness patterns are considered, as illustrated on the right side of **Figure 4.9** (a, b, c and d). To enhance the visual demonstration, the field flatness in these figures is exaggerated.

In this study, the cavity cells are stretched and squeezed to generate the desired field flatness pattern. Stretching the length of a specific cell in a multicell elliptical cavity elevates the level of the axial *E*-field of that cell and reduces the level of the axial *E*-field on the other cells. This is because of the increase in the volume and stored energy in the stretched cell compared with other cells. The Q_{ext} sensitivity to the field flatness developed is then studied. For instance, the field flatness pattern shown in **Figure 4.9** (a-right) is achievable by stretching the length of cells one and six, or by squeezing the length of cells three and four while other cavity geometries are kept at their nominal value. **Figure 4.9** (a-left) contains the calculated coupler Q_{ext} and field flatness values related to the four stretching values for cells one and six. The calculated Q_{ext} and field flatness values related to the four-squeezed length values for cells three and four are also presented. **Figure 4.10** illustrates a block diagram of the assessment process.

The coupler Q_{ext} versus the field flatness for the other three field flatness patterns in **Figure 4.9** (b, c and d) are also studied in a similar way to **Figure 4.9** (a). In this study, cell 1 is the cell adjacent to the power coupler port, and cell 6 is the cell closest to the pickup port. **Figure 4.9** (b and d) illustrates two possible cases in which the fundamental power coupler Q_{ext} will exceed $8 \cdot 10^5$. The estimated Q_{ext} for 93% field flatness in **Figure 4.9** (b) and (d) are roughly $8.5 \cdot 10^5$ and $8.3 \cdot 10^5$ respectively. In conclusion, it is recommended to avoid these two field flatness patterns.

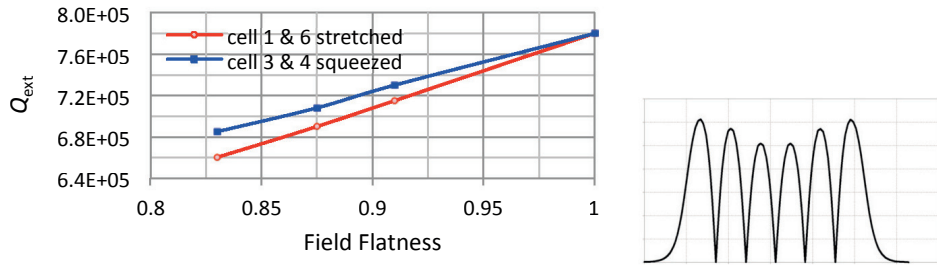

(a)

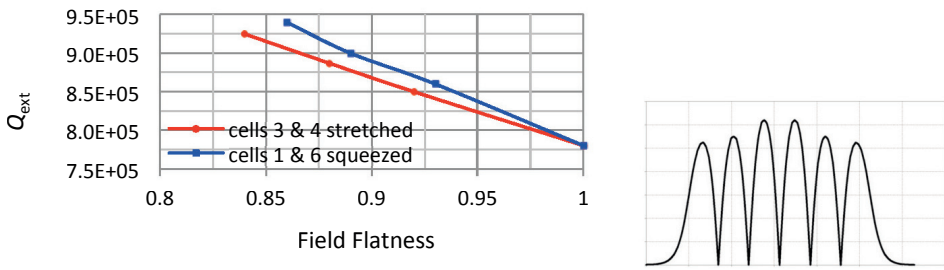

(b)

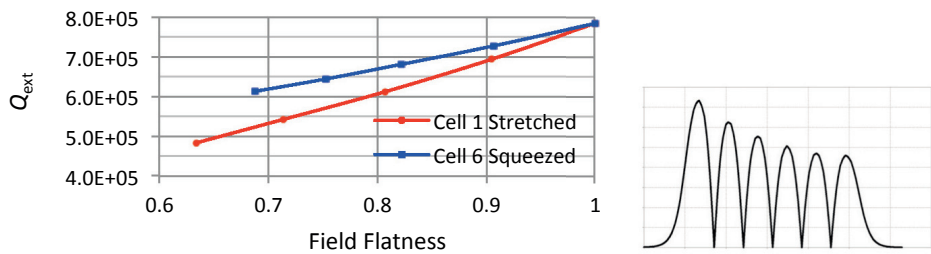

(c)

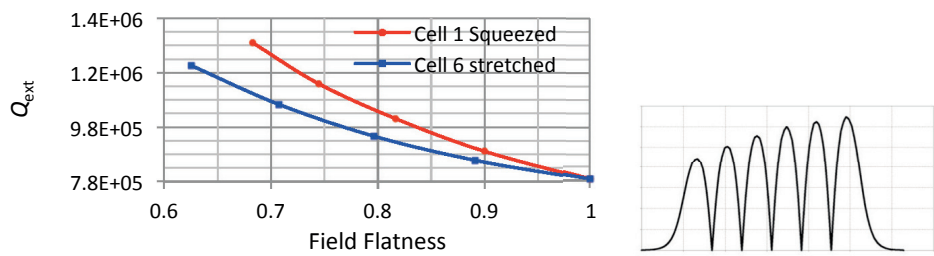

(d)

Figure 4.9. The Q_{ext} change vs. field flatness. (a) for 1st field flatness (b) for 2nd field flatness (c) for 3rd field flatness (d) for 4th field flatness

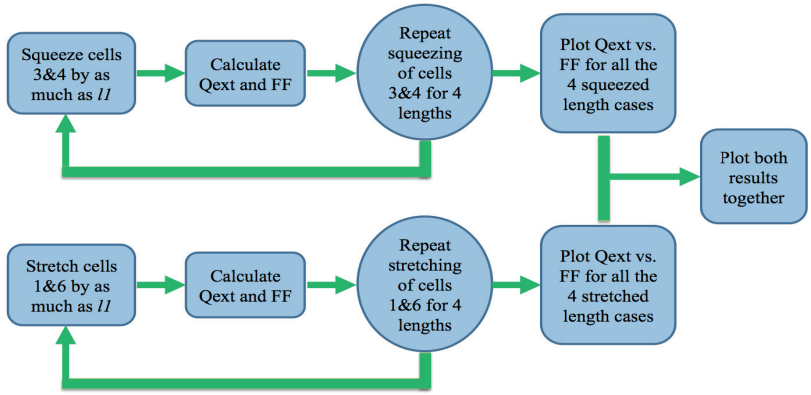

Figure 4.10. Q_{ext} vs. field flatness study block diagram

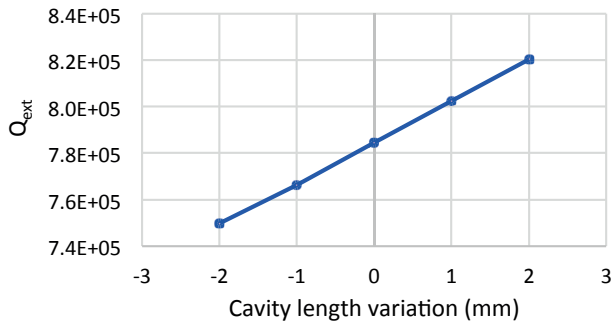

Figure 4.11. Cavity frequency tuner effect on Q_{ext} of the fundamental power coupler

Another source for the coupler Q_{ext} change after cavity assembly in the cryomodule is the cavity frequency tuner. The medium beta cavity mechanical simulation shows that 1 mm cavity length squeezed by the cavity tuner will result in 0.146 mm length reduction for cells 1 and 6, and 0.177 mm length reduction for the other cells. A cavity Q_{ext} change for the FPC in the result of the frequency tuner effect is illustrated in **Figure 4.11**, and shows that the frequency tuner reduces the Q_{ext} value.

4.2 Cavity fabrication

A multicell elliptical cavity mechanical fabrication is done in 300 K, whereas its nominal EM design and operation is in 2 K. This requires another EM

design to be prepared for the cavity at 300 K that considers temperature change, dielectric change from vacuum to air and chemical etching effect. The 300 K design provides a monitoring tool for the cavity frequency change during its fabrication process.

Forming niobium sheets to the half-cells and then welding them to each other is the procedure that was used to fabricate the ESS elliptical cavity, mainly because of the quality and price of modern forming and welding techniques. In the cavity fabrication, the niobium ingot is first cut by water jet to 4.5 mm-thick thin sheets after which the niobium sheets are shaped into half-cells using deep drawing. After deep drawing, some extra length on equator and iris sides is necessary for the welding process and for tuning their frequency before welding (Explained in following section). Further extra length on the iris and equator is trimmed.

The next step entails degreasing treatment and a few μm etching by buffered chemical polishing (BCP). The half-cells are then electron beam welded (EBW) through their iris to form the inner dumbbells, the pen dumbbells and the end-groups. Then the dumbbells and end-groups are welded to form the full six cells of the cavity. The main steps of the medium cavity fabrication—cavity geometry evolution, field flatness tuning and surface treatment—are explained below.

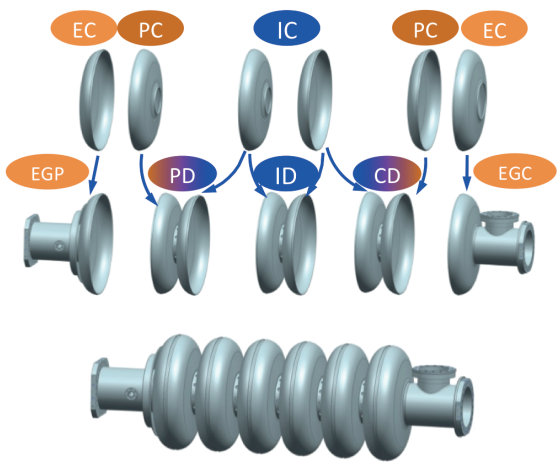

Figure 4.12. Sketch of the six-cell cavity with its subcomponents

4.2.1 Cavity geometry evolution

Once the half-cells have been formed, they are machined, leaving 0.35 mm and 2.5 mm extra length in the iris and the equator, respectively. To control the quality of the deep drawing, the Coordinate Measuring Machine (CMM) measures the half-cells. **Figure 4.12** shows a sketch of the medium beta cavity and its subcomponents. Inner dumb bells (ID) are composed of two inner-half-cells; terminal dumbbells (PD and CD) are made of one inner half-cell and one pen-half-cell; and an end-group is a beam pipe welded to an end half-cell.

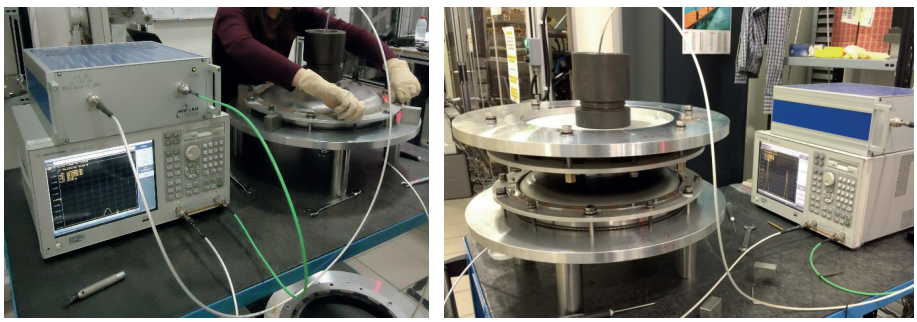

Figure 4.13. The half-cell and the dumbbell installation on the measurement tool for RF check. (left: half-cell check; right: dumbbell check)

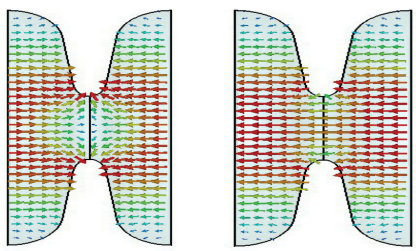

Figure 4.14. *E*-Field distribution in the dumbbell for the π mode and the 0-mode

The RF frequency and quality factor measurements are quality control checks for cavity subcomponents before welding. RF controls are carried out using a dedicated tool. **Figure 4.13** illustrates the measuring set-up during half-cell and dumb-bell RF tests. In the RF measurement tool, cavity subcomponents are placed between two niobium plates. The niobium material selection keeps cavity parts free from undesired material intrusion before welding. RF fingers on the external border of niobium plates are for better RF contact. The screws

and nuts in **Figure 4.13** are for contact enhancement and to press two niobium plates to the cavity parts during frequency measurement. An antenna on each niobium plate is connected to a vector network analyzer (VNA) for RF measurements. The test is repeated twice for each component. A second measurement is done after a 180-degree rotation of the beam axes. The frequency difference of the two measurements must be less than 200 kHz. The mode quality factor is measured as an index of the quality of the measurement. For these conditions, the quality of contact is acceptable if the measured Q factor is higher than 3000. The frequency of the cavity subcomponents must be measured with particular care to keep them free from scratches and foreign material. Because of boundary limitations, there are following cavity modes for the cavity subcomponents:

- For half-cells, only 0-mode frequency
- For dumb-bells, both 0 and π modes
- For end-groups, only π mode

Figure 4.14 shows the *E*-field distribution for the π mode and 0 mode in a dumbbell. The π-mode sign of *E*-field changes in adjacent cells, corresponding to a 180-degree phase difference, whereas for the zero mode the sign is the same in both cells.

To reach nominal 704.42[12] MHz accelerating mode frequency for the six-cell cavity at 2 K and in vacuum, it is essential to consider the effect of temperature change, dielectric change, and chemical etching on the cavity frequency change. This results in the capability to monitor the cavity frequency change during the fabrication process.

To cut the overlength on the iris and equator, a reference must be established. This is provided by a frequency sensitivity study of the cavity subcomponents versus their overlength on the iris and equator. The frequency of the cavity subcomponents is measured at room temperature and in the air. Therefore, in the first step, frequency corrections related to temperature and dielectric constant change (from air to vacuum) must be considered. To calculate the cavity frequency change due to temperature variation, we use the niobium integral linear expansion coefficient:

[12] - The frequency tuner effect, 200 kHz, is not considered

$$\frac{\Delta f}{f} = -\frac{\Delta l}{l}\Big|_{T_1}^{T_1+\Delta T}, \quad (4.3)$$

where Δl, Δf and ΔT are the cavity length change, frequency change and temperature change, respectively. The middle column of Table 4.4 shows the niobium linear expansion coefficient percentage calculated by [73], whereas the right column shows the frequency change of the 6-cell cavity π mode as a function of temperature variation. This data illustrates a 1.028 MHz frequency increase caused by a temperature drop from 300 K to 2 K (**Figure 4.15**). The resonant frequency increase between 80 K and 2 K is not linear as it is caused by the nonlinear behavior of the expansion coefficient value in this boundary.

The resonant frequency change due to filling the cavity with 1 bar air with 50% humidity (ε_r=1.000664) is:

$$\frac{\Delta f}{f} = (\frac{1}{\sqrt{\varepsilon_r}} - 1). \quad (4.4)$$

Table 4.4.
Temperature variation effect on niobium length variation percenatage and on 6-cell cavity frequency change

Temperature	$\frac{dl}{l}$%	$\Delta f\,(kHz) = f \times -\frac{dl}{l}$
300	0	0
290	-0.057	40.15194
260	-0.265	186.6713
230	-0.47	331.0774
200	-0.65	457.873
170	-0.845	595.2349
140	-1.021	719.21282
110	-1.175	827.6935
80	-1.34	943.9228
50	-1.41	993.2322
20	-1.45	1021.409
8	-1.46	1028.4532
4	-1.46	1028.4532
2	-1.46	1028.4532

This results in a roughly 233.4 kHz frequency decrease in the cavity π–mode resonant frequency. The cavity 0-mode frequency is calculated from its π-mode frequency by:

$$\frac{f_\pi}{f_0} = \frac{1}{\sqrt{1-2k}} \ , \tag{4.5}$$

where k=1.55% is cell coupling. The inner half-cell frequency change due to uniform chemical etching is calculated using the cavity simulation in BuildCavity. It is -3.28 kHz/μm for the π-mode and -4.45 kHz/μm for the 0-mode. More realistic values retrieved from bulk BCP processes reveal that the RF etching coefficient is about -3 kHz/μm. Table 4.5 illustrates the frequency evolution from the inner half-cell 0-mode to the six-cell cavity π-mode, based on the considerations explained.

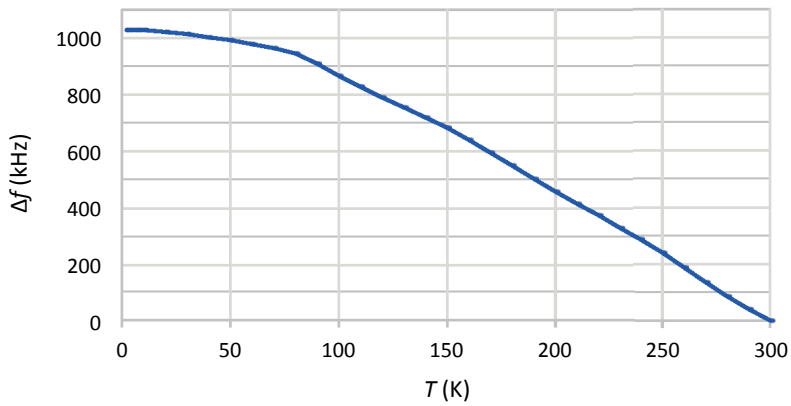

Figure 4.15. The medium beta cavity temperature change from 2 K to 300 K effect on the cavity π-mode frequency variation

Table 4.5.
Frequency evolution from the inner half-cell 0-mode to the six-cell cavity π-mode

Effect	Δf [kHz]	f_π [MHz]	f_0 [MHz]
Cavity @ 2K in vacuum		704.42	n.a.
Cavity @ 300K in vacuum	-1028.45	703.39	n.a.
Cavity @ 300K in air	-233.41	703.16	n.a.
HC after BCP			692.17
HC before 150um BCP		703.65	692.84

4.2.2 Cavity field flatness tuning

In a multicell elliptical cavity, the cavity EM design provides 100% field flatness so maximize the net accelerating voltage and minimize the pickup *E*-

field on the cavity surface. In a six-cell cavity such as the medium beta cavity, geometrical errors in the cavity cells are inevitable (see fabrication procedure explained in previous section). Field flatness tuning is a solution to compensate for geometrical errors and correct the field flatness for the cavity acceleration mode. For the medium beta cavity, field flatness tuning is applied in two steps during the fabrication:

- After the EBW of the cavity subcomponents and realization of the 6-cell cavity
- After the bulk chemical etching and cavity heat treatment

Figure 4.16 shows the tuning machine used for the MB001 cavity field flatness tuning. The tuning machine consists of two metallic plates, which move together and push or pull the sides of a cell. These are installed on the sides of the cell that is to be tuned. There is a half-circle cut in each plate matching the external diameter of the iris; the pair of plates with the aperture in the middle is fitted to the cavity iris. An automated bead-pull measurement system is embedded in the tuning machine. The resonant frequency is monitored via a VNA connected to the cavity coupler and pickup ports. A computer program sets up the VNA, reads the resonant frequency for the cavity mode, then moves the bead and plots the *E*-field profiles.

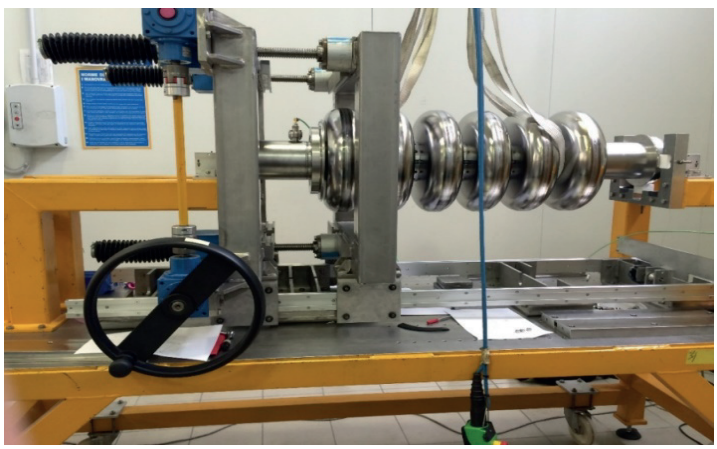

Figure 4.16. Tuning machine for cavity field flatness tuning

For a cavity resonating at f_0 frequency and with U_0 stored energy, field flatness is measured by perturbing the *E*-field of the accelerating mode. From the Boltzman/Ehrenfest theorem adapted to the RF cavities we have:

$$\frac{d\omega}{\omega_0} = \frac{dU}{U_0} . \tag{4.6}$$

The cavity E-field is perturbed using a metallic bead put on a nylon string. The metallic bead moves along the cavity axis, where the magnetic field is zero, so from (4.6), $\delta f \propto E^2$ [74]. Therefore, maximum E-fields in each cell ($E \approx \sqrt{|\delta f|}$) will be derived along the longitudinal axis of the cavity. In the case of the MB001 cavity, the first field flatness tuning after EBW modified the cavity field flatness from 70% to 97%. The bulk BCP and its subsequent heat treatment reduced field flatness to 91.5%, second field flatness tuning then increased the field flatness value to 97.5% (**Figure 4.17**).

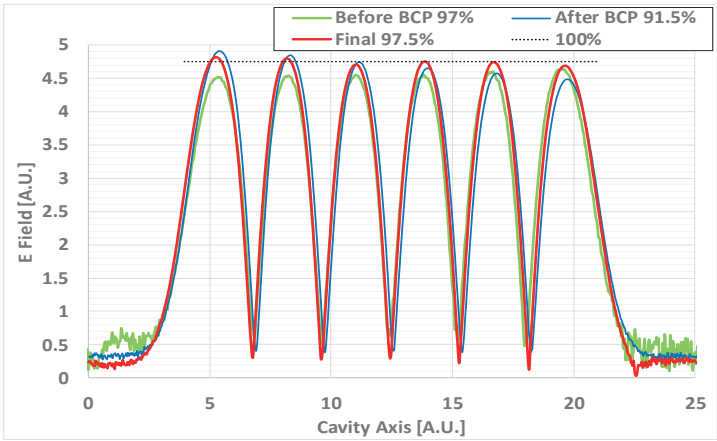

Figure 4.17. Field profile evolution of MB001 cavity

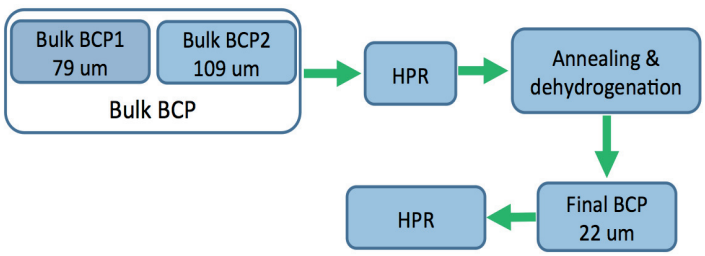

Figure 4.18. Surface treatment block diagram performed for MB001 cavity

4.2.3 Cavity surface treatments

For the best performance, the cavity RF surface in the SRF cavities must be free from damage and dust. Contaminations on the SRF cavity surface result in unexpected hot spots and field emission. Damaged and contaminated layers can be found on the cavity surface due to the cavity fabrication scheme and exposure of the cavity surface to air, oil and moisture. Surface analysis studies illustrate that the niobium surface is covered with a few monolayers of hydrocarbon, a few nm of Nb-pentoxide (Nb_2O_5) layers, and, underneath the pentoxide, monolayers of niobium sub-oxides (NbO, NbO_2) [75]. BCP and electropolish (EP) are techniques that remove such damaged layers. Whereas EP results in a smoother surface, BCP is simpler.

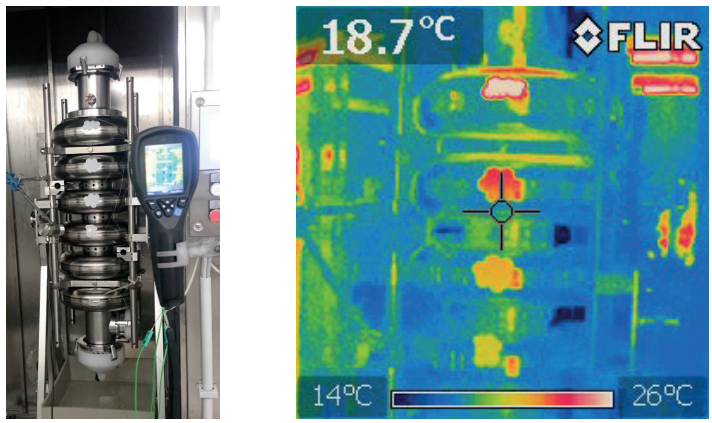

Figure 4.19. (left) MB001 cavity under BCP, (right) Infrared camera picture

Chemical etching

A surface treatment block diagram for the MB001 cavity is shown in **Figure 4.18**. The BCP is a mixture of one part hydrofluoric acid, one part nitric acid, and two parts phosphoric acid (1:1:2). The etching rate for this acid mixture on a flat surface is roughly 2.5 μm/min. For a multicell cavity (such as MB001) the cavity volume necessitates a large volume of acid. Therefore, instead of immersing the cavity in the acid, it is more efficient to design and implement a closed circuit system for the acid. This fills the cavity with the cold acid from a tank with pumps then drains the warm acid. At the end of the BCP cycle, the cavity is rinsed with ultra-pure water. The cavity is etched in two main steps: bulk and final BCP.

- Bulk BCP is done after EBW of the cavity parts and cavity realization. The etching amount for the MB001 cavity at this stage is roughly 188 μm. The aim is to remove damaged and polluted layers from the cavity surface.
- Final BCP is performed after a 600 ºC cavity heat treatment to remove possible pollutions that adhere to the cavity surface during its time in the furnace. The etching amount for the MB001 cavity is roughly 22 μm.

As illustrated in **Figure 4.19**, the BCP is done vertically. There is a higher etching rate for the lower cells. To compensate for this effect, the bulk BCP is divided into bulk BCP1 and bulk BCP2. In the bulk BCP2, which takes 90 minutes, the cavity is rotated 180 degrees. During chemical etching, the acid reaction on the cavity surface generates heat[13] and the acid temperature increases. In the meantime, due to the exponential dependence of the diffusion constant of the gases to the temperature, hydrogen diffusion increases in the cavity bulk. To prevent an unexpected Q drop due to Nb-hydride precipitation on the RF surface of the cavity, it is essential to control the temperature increase during BCP. In the MB001 cavity, the acid temperature is monitored via a set of 6-thermocouple sensors: three are on cell-1 and three are on cell-6 (**Figure 4.20** (right)). The cavity acid outlet is cooled by a heat exchanger. **Figure 4.20** (left) shows the recorded temperature change in the six sensors during the bulk BCP2. The temperature is stable for all sensors except for a few minutes at the beginning and end of the BCP cycle. By filling the cavity with acid at the beginning of the BCP, there is no acid flow and no extraction of warm acid from the cavity acid outlet. As such, there is only heat generation and no heat transfer. In contrast, during the final few minutes of the BCP cycle, as the acid flow stops, the heat transfer process is stopped again and heat is generated only, resulting once again in a temperature increase on the cavity surface.

Orange peeling on the cavity surface is an inevitable BCP effect, but due to its smooth texture will not lead to any excess in field emission. The BCP increases the inner volume of the cavity, thus reducing the resonant frequency of the cavity modes. The acid flow in the cavity etches the iris, the equator, and the wall between them in different amounts. The acid flow around the iris is higher than around the equator, so the etching rate on the

[13] - Process is exothermic

iris is higher. Based on cavity geometry, the wall etch has an average etching value between the iris and equator. To estimate the amount of etching on the iris, the equator, and the wall between them, for simplicity we firstly consider a uniform etching condition. The average etching thickness is calculated using the internal cavity surface (=1.8 m^2), the niobium density (=8.57 gr/cm^3), and the cavity weight change before and after BCP.

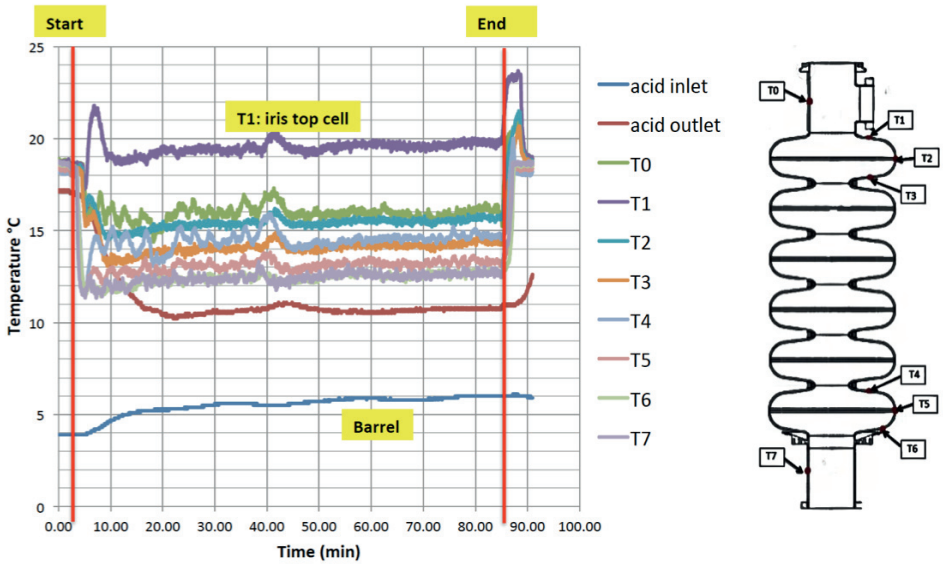

Figure 4.20. The BCP temperature control through thermocouple sensors for 20 minutes during BCP1 A

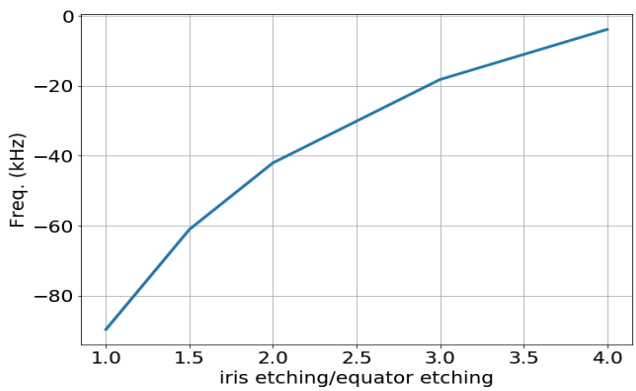

Figure 4.21. Cavity frequency change versus iris etching ratio over the equator etching (average etched is 28 μm)

Table 4.6 shows the uniform etching value for the three BCP steps. BCP1 is divided into BCP1-A and BCP1-B to provide better monitoring during etching and to retrieve more data for cavity weight and frequency change. The ratio of iris etching over equator etching for the three BCP steps is also illustrated. The etching ratio is determined based on the change in cavity resonant frequency (as a result of BCP). **Figure 4.21** illustrates the MB001 cavity frequency change versus the ratio of iris etching over equator etching. BuildCavity has been used to calculate the etching ratio. The same acid is used for all the three BCP steps. This reduced the etching ratio from 1.5 to 1.2 due to acid purity degradation. After each BCP stage, a high-pressure rinsing (HPR) cycle cleans the cavity. HPR has a significant effect on improving the cleanliness of the RF surface by removing dust and residual acid on the cavity surface, and results in less field emission and a higher accelerating gradient.

Table 4.6.
Etching calculation summary for the 3 steps of bulk BCP for MB001.

	Freq. change (kHz)	Weight change (g)	Average etching (μm)	Freq. sensitivity (kHz/μm)	Etching ratio (iris/equa.)
BCP1 A	-62	434	28	-2.2	1.5
BCP1 B	-155	795	51	-3.0	1.1
BCP 2	-306	1685	109	-2.8	1.2

Heat treatment

For 10 hours 600 ºC heat treatment in the vacuum furnace is applied for the MB001 cavity to remove hydrogen contamination from the niobium bulk. Through this procedure, the cavity will be safe from yield strength drop and grain size growth. The vacuum furnace temperature and pressure during cavity temperature treatment vs. time are illustrated in **Figure 4.22** (Up). The effect of 10 hours baking on the reduction of diffused hydrogen in the niobium is represented by the significant pressure drop illustrated in **Figure 4.22** (Down).

4.3 Cavity Measurements

In the SRF cavity vertical test, the cavity is immersed vertically in liquid helium. The cryogenic operation starts by filling the cryostat with liquid

helium, on which the temperature changes from 4.2[14] K to 2 K because of the lower pressure. The cavity may or may not have a helium tank. The vertical test checks the main parameters of the cavity, such as Q_0 versus E_{acc}, field emission onset and surface resistance. In the vertical test, the cavity probe antenna stays close to critical coupling condition to minimize the amount of RF power reflection. In this case a low-level RF (LLRF) is designed to track the cavity RF frequency.

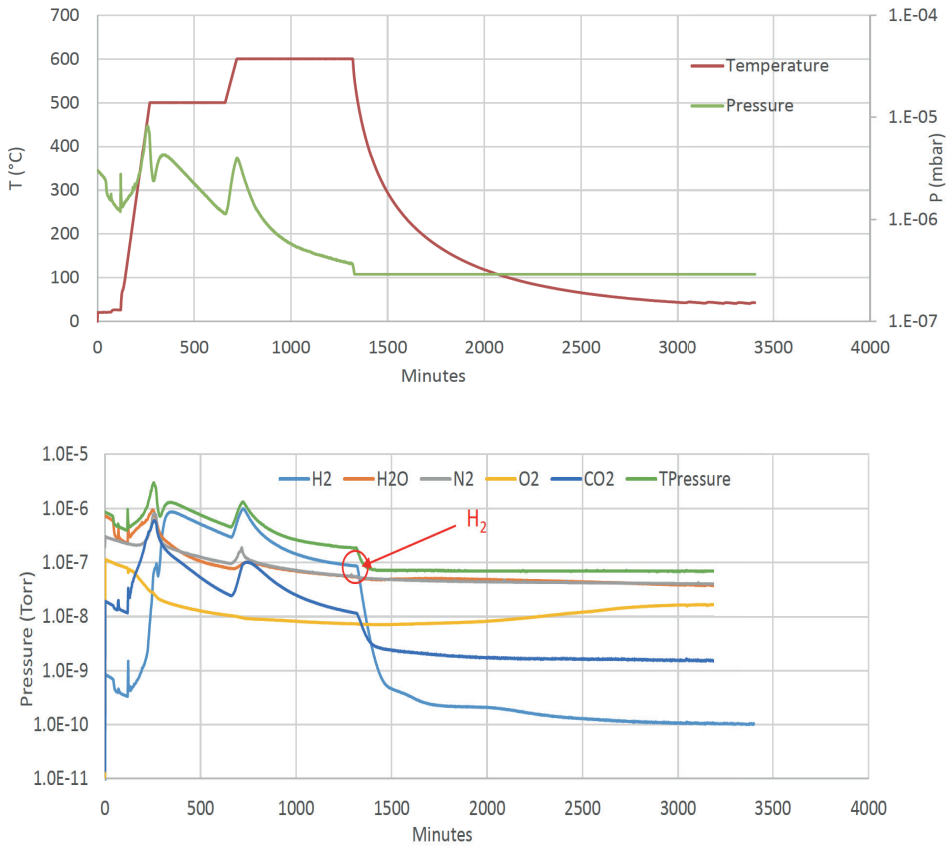

Figure 4.22. (Up) Vacuum furnace temperature and pressure monitoring vs. time (Down) Different gas pressure levels in vacuum furnace during MB001 heat treatment

In the cryomodule test, a few cavities (four in the ESS) are normally placed inside the final cryomodule. Cavities are equipped with a helium tank and

[14] - Liquid helium temperature at normal atmospheric pressure

placed horizontally. Due to beam loading considerations the cavity coupler is highly over-coupled. In this case, the LLRF drives the cavity in a fixed frequency operation mode and frequency is tuned with frequency tuner system designed for the cavity.

Figure 4.23 (left) shows the MB001 cavity ready to be installed in the vertical test cryostat. **Figure 4.23** (right) shows the upper part of the LASA vertical cryostat, with vacuum system, sub-cooling pumps and signal cables connected to the top flange of the insert. The internal surface of the cryostat is covered with mu-metal to reduce the residual magnetic field to less than 8 mG in the cavity region. The cool-down rate is roughly 0.5 K/min when crossing the critical temperature of 9.2 K. In the following, the vertical test methodology, test results for the MB001 cavity and uncertainty in the cavity RF measurement are discussed.

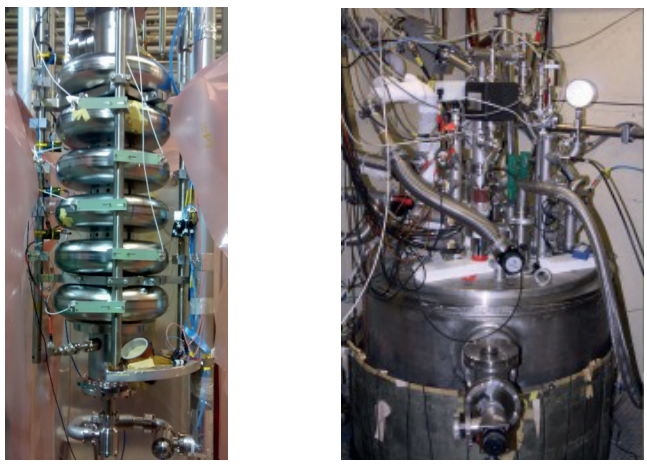

Figure 4.23. (Left) Cavity prepared form the vertical test cryostat, (Right) upper part of vertical cryostat.

4.3.1 Testing methodology

The vertical test for an SRF cavity is typically performed in three main steps: cable calibration, pulsed operation measurement (for the cavity decay time) and continuous wave operation (for E_{acc} versus Q_0 measurement). In practice, cavity parameters are calculated by measureable signals. A typical block diagram for a cavity vertical test is shown in **Figure 4.24**. Power traveling along the transmission line toward the cavity (P_{fwd}), power coupled out from the cavity coupler port (P_{ref}), and power coupled out through the pickup port

(P_t) are available for measurement by attaching power meters and directional couplers.

Pulsed operation measurement

In the cavity pulsed operation, we have for the decay time measurement:

$$\frac{dU}{dt} = -P_{tot} \quad \rightarrow \quad U(t) = U_0 \, exp\,(\frac{-\omega_0 t}{Q_L}) \,, \tag{4.7}$$

where U_0 and Q_L are decaying stored energy and the loaded quality factor, respectively. The decay time is equal to:

$$\tau_d = \frac{Q_L}{\omega_0} \,. \tag{4.8}$$

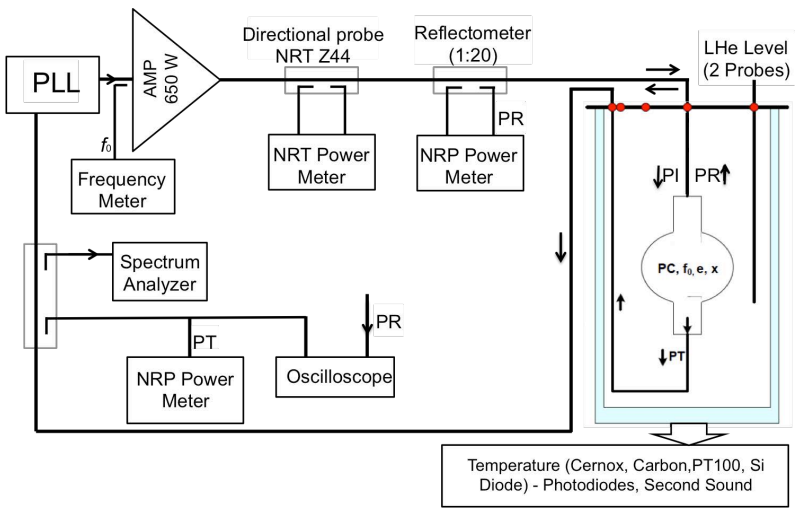

Figure 4.24. Block diagram of RF system in vertical test [97]

Monitoring the P_{ref} is a practical way to measure cavity decay time. **Figure 4.25** shows typical measureable signals for P_{fwd}, P_{ref} and P_t in undercoupling (β<1), critical coupling (β=1) and over-coupling conditions (β>1). In the SRF cavities under operation in accelerator machines (due to the high amount of required beam power), the cavity is highly over-coupled. Based on equation (3.20), β_i and β_t need to be measured to calculate Q_0. Following [32], when the cavity is in a steady-state condition (cavity stored energy change is zero) and its coupler is over-coupled:

$$\beta_i = \frac{1+\sqrt{\frac{P_{ref}}{P_{fwd}}}}{1-\sqrt{\frac{P_{ref}}{P_{fwd}}}}, \tag{4.9}$$

also

$$P_{diss} = P_{fwd} - P_{ref} - P_t, \tag{4.10}$$

$$\beta_t = \frac{P_t}{P_{diss}}. \tag{4.11}$$

We can calculate Q_0 through the cavity power measurement.

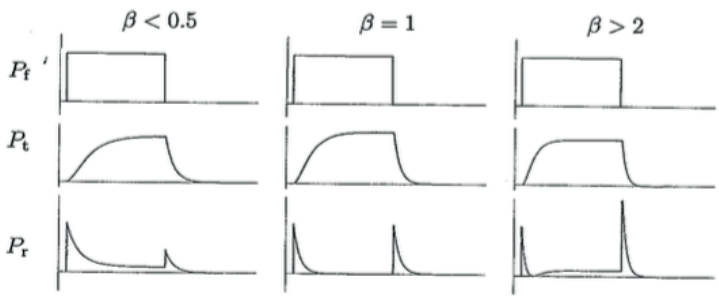

Figure 4.25. Pattern of P_{fwd}, P_t and P_{ref} measurement in SRF cavity power test [32]

Setting probe antenna length

As there is no beam before cavity integration in the cryomodule, it is preferable to have the minimum power reflection (β=1) for the antenna on the cavity coupler port. In contrast, the probe antenna design should intentionally be a little over-coupled. This allows the benefit of zero crossing of the reflected power envelope during cavity charging (see **Figure 4.25** for P_r waveform for β>2). Critical coupling is achieved at the highest E_{acc} values when, due to increased P_{diss}, the Q_0 factor goes down, minimizing the amount of P_{ref}. The correct length of the probe antenna is set up in two steps:

- Calculation of the probe antenna length via CST
- Probe antenna length tuning by Q_{ext} measurement at room temperature

After deriving the proper length of the probe antenna by Q_{ext} calculation in CST, the final probe antenna length will be set by its Q_{ext} measurement at room temperature. In this case, an extra antenna with a coupling close to β=1 will be assembled on the beam pipe cut-off on the opposite side of the cavity coupler port. **Figure 4.26** is a schematic view of the cavity antennas for setting the length of the probe antenna at room temperature. First, we tune the antenna length on the beam pipe cut-off to have enough 3dB bandwidth for a reliable Q_{ext} measurement on this port. Considering the cavity beam pipe length, we set the length of the antenna on the beam pipe cut-off as a compromise between the low frequency perturbation (less than 10 kHz) on the cavity mode and sufficient coupling to have measurable S_{11} graphs. Measuring transmission signals from the probe antenna to the antenna on the beam pipe cut-off performs the length adjustment. For the MB001 cavity with an arranged set up (copper tube with L = 170 mm, r = 10 mm), the coupling factor for the port on the beam pipe cut-off is β_i = 0.57. To obtain this value, a Smith Chart or SWR graph can be used, with which $Q_i = Q_0 / \beta_i$ is obtained. Once the Q_{ext} of the antenna on the beam pipe cut-off is available, the Q_{ext} of the probe antenna will be obtained using the following equation:

$$\frac{P_t}{P_i} = \frac{(2Q_L)^2}{Q_{ext1}\, Q_{ext2}} . \qquad (4.12)$$

where Q_L is the cavity loaded Q, Q_{ext1} belongs to the probe antenna, and Q_{ext2} is for the antenna on the beam pipe cut-off. P_t/P_i is the S_{21} transmission signal measured between these two antennas. Repeating this process for a few antenna probe lengths will result in a proper estimation on the probe antenna length. For the MB001 cavity, the probe antenna is tuned for Q_{ext} = $9 \cdot 10^9$, where a Q_0 =$2 \cdot 10^{10}$ is expected at 2K temperature. The graph in **Figure 4.27** shows a summary of the measurements for MB001 when length of the probe antenna is correctly set. Room temperature measurement results are consistent with the CST simulation for Q_{ext}. A correct antenna length is 9 mm, i.e. the distance between the antenna tip to the surface of the flange.

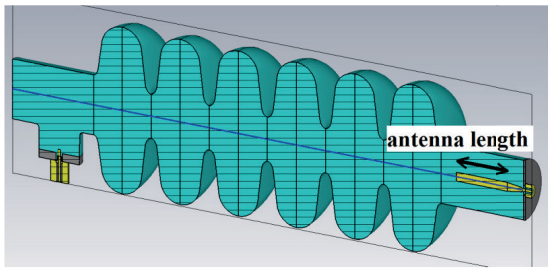

Figure 4.26. Schematic view of antenna assembled on cavity axis for tuning the probe antenna length on cavity coupler port (at room temperature)

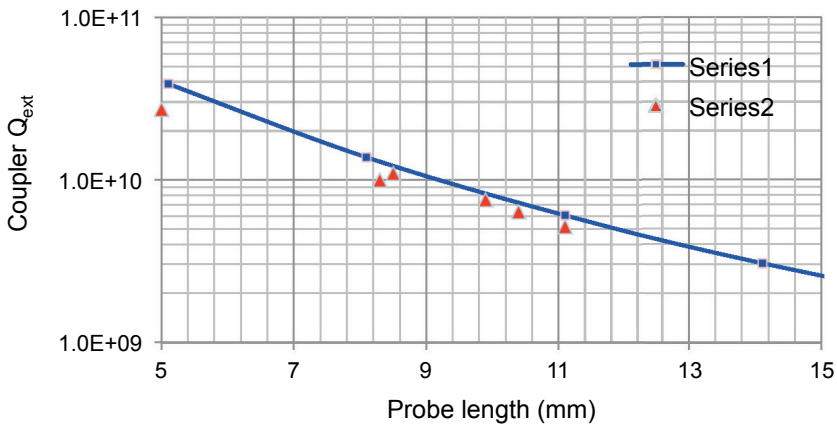

Figure 4.27. Q_{ext} of probe antenna implemented for vertical test vs. antenna tip penetration depth (series 1) CST simulation result. (Series 2) Room temperature measurement result with antenna on beam pipe cutoff plane.

4.3.2 Cavity measurement results

During cavity cool down, the cavity π-mode frequency is monitored to check cavity behavior. **Figure 4.28** illustrates the tracked cavity resonant frequency as a function of temperature. Even between 4 K and 2 K, there is no significant thermal contraction in the cavity geometry; however, because of the increase in helium pressure in the cryostat, there is some frequency increase for the cavity. **Figure 4.29** illustrates the frequency of the six modes of the cavity TM_{010} band. The cavity π-mode is successfully set at 704.213 MHz (A 0.2 MHz frequency shift from the goal is the range left for the tuner preload operation) and the π-mode is 0.76 MHz away from the 5/6 π mode.

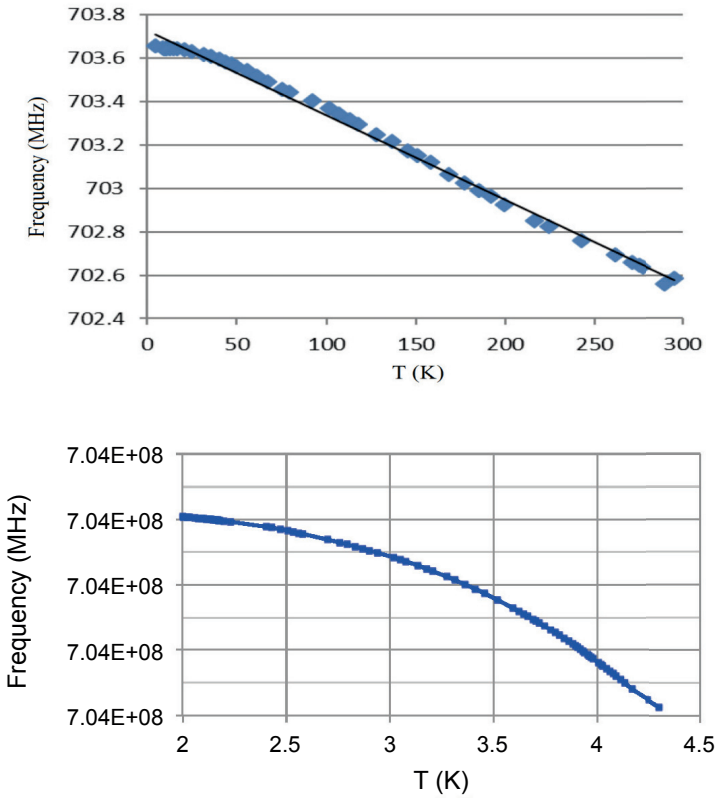

Figure 4.28. Cavity frequency measurement (Up) from 300 K to 4.2 K, (Down) from 4.2 K to 2 K.

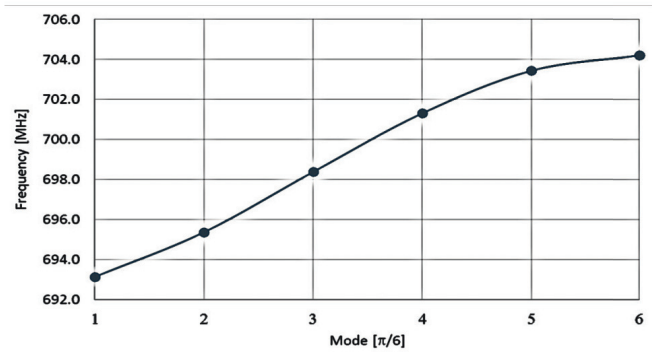

Figure 4.29. Measured mode frequencies of first cavity band

Continuous wave (CW) measurement

For a cavity vertical test, a solid-state power amplifier is required as an RF source and a circulator is needed for RF source protection. Incident and reflected powers are sampled through a reflectometer, whereas a power meter monitors the real amplifier power output and loading conditions via a power directional probe. The pickup antenna is used to monitor the cavity field. All power transmitted from the cavity is carried out from the cryostat through high-screened cryogenic coaxial cables. Finally, coaxial cables with high phase stability are used to transmit the cavity powers to and from the external electronic devices and instrumentation. The accelerating field and quality factor Q of the cavity are measured by accurately reading the input and reflected powers and the entire power transmitted by the cavity, in CW and pulsed modes. The measurement set up is calibrated at low field, where low field means E_{acc} level where there is no field emission and multipacting, and Q_0 is acquired by measuring the cavity decay time in pulsed mode. We calculate Q_0 by equation (3.20) and E_{acc} by:

$$E_{\mathrm{acc}} = \frac{\sqrt{P_{\mathrm{diss}} Q_0 \frac{R}{Q}}}{L_{\mathrm{eff}}}. \tag{4.13}$$

We then define a calibration constant K_E as:

$$K_E = \frac{E_{\mathrm{acc,low\,field}}}{\sqrt{P_{\mathrm{t,low\,field}}}}. \tag{4.14}$$

After which we perform the power rise test. The RF power rise will be implemented in fixed steps. For each step, Q_0 and E_{acc} will be measured using the following equation:

$$E_{\mathrm{acc}} = \sqrt{P_{\mathrm{t}} K_E}\,, \tag{4.15}$$

$$Q_0 = \frac{(E_{\mathrm{acc}} L_{\mathrm{eff}})^2}{P_{\mathrm{diss}} \frac{R}{Q}}. \tag{4.16}$$

Registering measured values derived by (4.15) and (4.16) in a cavity power raise, result in Q_0 versus E_{acc}. This is an essential characteristic for an SRF cavity and demonstrates its high power performance. We then calculate the Q_0 of the cavity at a moderate value of the accelerating field and determine the calibration constant before the power rise. The coaxial cables that connect

the test signals to the read-out instrumentation must be very accurately calibrated (within some tenth of a dB) before starting the test. Due to high Q (narrow bandwidth) resonance in the SRF cavity, a Phase Locked Loop (PLL) is required for the vertical test. Moreover after installation of the FPC, we use the following equation for E_{acc} calculation:

$$E_{\mathrm{acc}} = \frac{\sqrt{4\frac{R}{Q}Q_{\mathrm{L}}P_{\mathrm{fwd}}}}{L_{\mathrm{eff}}}. \qquad (4.17)$$

When looking at the nominal Q_0 definition (ratio of cavity stored energy to cavity wall power loss), we expect a constant Q_0 as long as the cavity power loss increase is proportional to the stored energy. Nevertheless, normally in the cavity high power test this doesn't happen. **Figure 4.30** shows the power test measurement result for the MB001 cavity without a helium tank. The measured Q_0 and radiation are demonstrated versus E_{acc}. Multipacting and field emission result in Q_0 degradation. Both field emission and multipacting have non-linear loss increase characteristics in comparison with the stored energy of the cavity.

Although the ESS specification for the maximum E_{acc} is 16.7 MV/m, for the MB001 the E_{acc} reached to 21.6 MV/m at $Q_0 = 6\cdot10^9$. An observed increase in *X*-ray radiation for E_{acc} 9–12 MV/m on the first power rise is a sign of soft multipacting. It has been resolved after a few minutes of RF processing. At the second power rise, again the level of *X*-ray radiation increased, but this time the multipacting passed without RF processing. In both power rises, from 18 MV/m up to the cavity quench, an increase in *X*-ray radiation due to field emission is noticeable. After integrating the naked cavity with a helium tank, a flash BCP and HPR are performed on the cavity. This surface treatment causes the multipacting and field emission issues observed during the naked cavity measurement to disappear. **Figure 4.31** illustrates the MB001 cavity power test results for Q_0 versus $\mathrm{E_{acc}}$ after cavity integration in a helium tank and further surface treatments. Q_0 at low field is $1.78\cdot10^{10}$, and is $0.6\cdot10^{10}$ for 22 MV/m. The cavity began to quench at accelerating gradients higher than 22 MV/m.

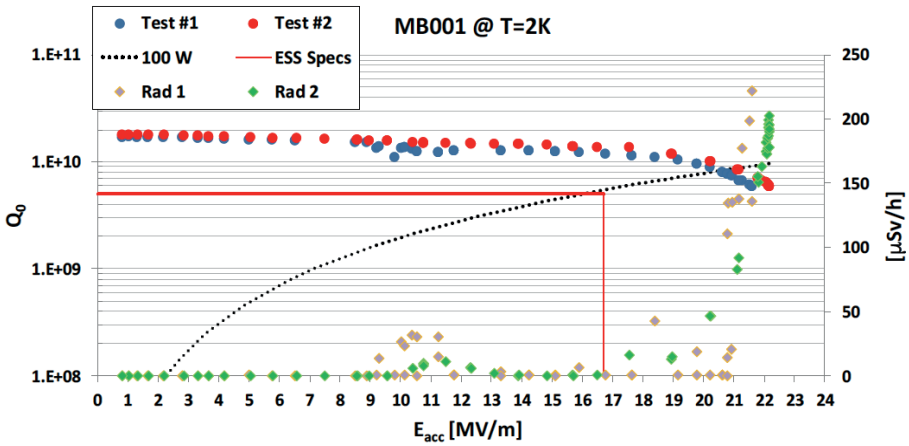

Figure 4.30. MB001 cavity Q_0 and radiation measurement vs. E_{acc} without He Tank

4.3.3 Surface resistance

Superconductors do not show dc resistivity. However, for microwave frequencies, Cooper pairs do not expel the microwave field completely. In an SRF cavity, a time-varying magnetic field of a cavity mode induces a time-varying *E*-field in the skin depth of the SRF cavity. Coupling the *E*-field to unpaired electrons, accelerating and decelerating them, produces dissipation. Equation (2.3) shows a surface resistance influence on the power dissipation. Sources of surface resistance for an SRF cavity when the temperature is below T_c are:

- Unpaired electrons (R_{BCS})
- Residual resistance (R_{res}).

R_{BCS} is temperature-dependent, whereas R_{res} is temperature-independent and depends on foreign material inclusion within the penetration depth of niobium, grain boundaries, surface defects, hydrogen adsorption and trapped dc magnetic flux. R_s and R_{BCS} are calculated by:

$$R_s = R_{\mathrm{BCS}} + R_{\mathrm{res}} = \frac{G}{Q_0} \tag{4.18}$$

$$R_{BCS}(T) = A_s \omega_0^2 \, exp\left(\frac{-\Delta(0)}{k_B T}\right) = \frac{2\times10^{-4}}{T}\left(\frac{f_0}{1.5}\right)^2 exp\left(\frac{-17.67}{T}\right). \tag{4.19}$$

G is the geometry factor, the exponential term shows the number of unpaired electrons, k_B is the Boltzmann constant, Δ is the energy gap and A_s depends on material properties, such as Fermi velocity, London penetration depth, electron mean free path and coherence length. Equation (4.19) shows that the superconducting transition temperature (T_c) and RF frequency influence on R_{BCS} are $1/T_c$ and f^2, respectively. **Figure 4.32** shows the measured R_s and R_{BCS} for the MB001 cavity as a function of temperature from 4.2 K to 2 K subcooling. At 2 K, the dominant term in surface resistance is R_{res}.

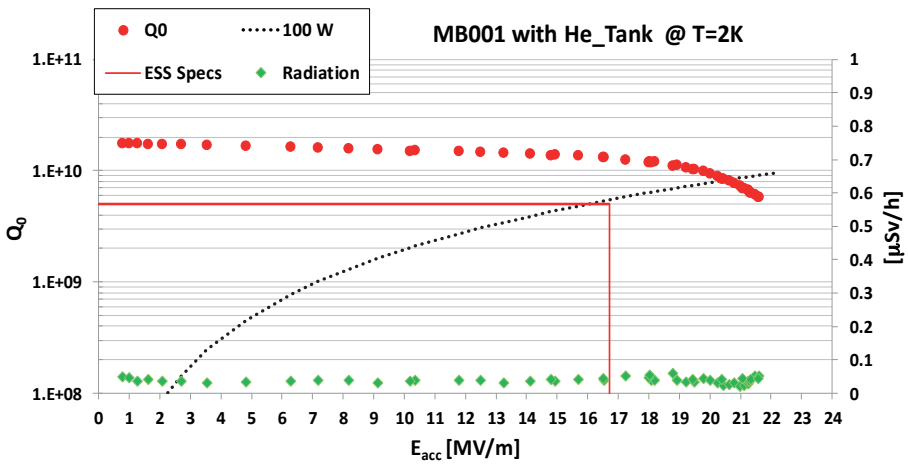

Figure 4.31 MB001 cavity Q_0 and X-ray radiation vs. E_{acc} measurement result with He Tank

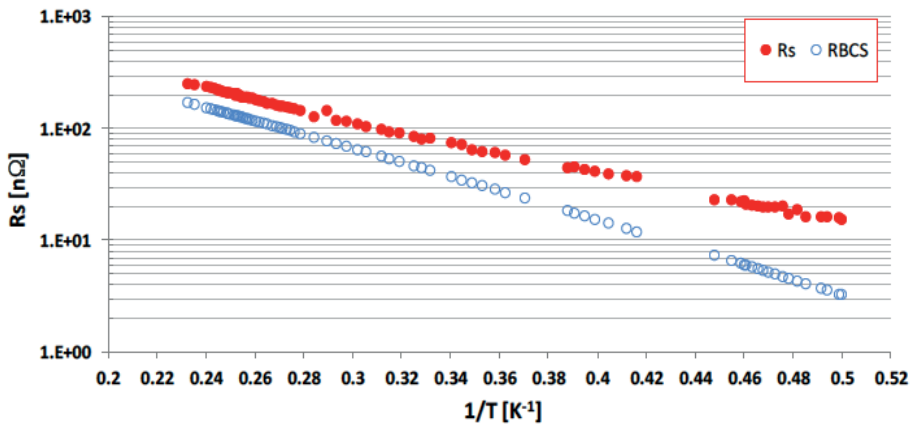

Figure 4.32. Surface resistance behavior vs. temperature between 4.2 K to 2 K

4.4 Uncertainty in cavity RF measurement

Efforts are ongoing to deliver SRF cavities with better performance, as well as lower fabrication and operating costs by producing new cavity surface treatment recipes and applying new alternatives to bulk niobium. A proper measurement error analysis—to understand the nature and amount of the measurement uncertainty—is essential to evaluate the significance of any improvement achieved in each R&D case. This section explains the error analysis in RF measurement of an SRF cavity for the Q_0 measurement. Q_0 is considered due to its importance in an SRF cavity. Generally, SRF cavity performance is evaluated by a vertical test. The procedure explained in this section for uncertainty assessment is for the vertical test. This section is mainly developed by following the content in [76], [77] and [78].

The Q_0 in an SRF cavity test is a function of different measured variables. Considering parameter x as a function of *u* and *v* ($x=f(u, v)$), the variance of the x (σ_x^2) based on the error propagation equation in [80] is derived as:

$$\sigma_x^2 = \sigma_u^2\left(\frac{\partial x}{\partial u}\right)^2 + \sigma_v^2\left(\frac{\partial x}{\partial v}\right)^2 + 2\sigma_{uv}^2\left(\frac{\partial x}{\partial u}\right)\left(\frac{\partial x}{\partial v}\right), \tag{4.20}$$

where the first two terms relate to the deviation of *x* from its true value as a result of independent uncertainty in *u* and *v*, respectively. The third term implies correlation between *u* and *v* in deviating *x* from its true value. The σ_{uv}^2 is zero for no correlation between u and v (this is for parameters measured with different devices). Based on $Q_0 = Q_L(1+\beta_i+\beta_t)$, the Q_0 measurement in pulse mode is a function of the cavity decay time (due to Q_L) and coupling factor measurement values. Since the measurement uncertainties of decay time and coupling are uncorrelated, the Q_0 variance is derived as:

$$\sigma_{Q_0}^2 = \sigma_\beta^2\left(\frac{\partial Q_0}{\partial \beta}\right)^2 + \sigma_\tau^2\left(\frac{\partial Q_0}{\partial \tau}\right)^2 . \tag{4.21}$$

This results in measurement uncertainty of Q_0 as [78]:

$$\left\langle\left(\frac{\Delta Q_0}{Q_0}\right)^2\right\rangle^{1/2} = \left[\left\langle\left(\frac{\Delta\tau}{\tau}\right)^2\right\rangle + \frac{1}{(1+\beta^{-1})^2}\left\langle\left(\frac{\Delta\beta}{\beta}\right)^2\right\rangle\right]^{1/2} . \tag{4.22}$$

For the Q_0 measurement in a continuous wave mode test, equation $Q_0=(E_{acc}L_{eff})^2/(P_{diss}(R/Q))$ is used. R/Q and L_{acc} values taken from the cavity

simulation with ideal geometry also affect Q_0. From [77], the expected error in a real cavity with possible variation in the cavity geometry is in the order of 1%. In the vertical test for measuring the Q_0, it is essential to measure forward power (P_{for}), reflection power (P_{ref}) and transmission power (P_T).

In a vertical test there are random and systematic uncertainty error sources. Operator errors and cable bending (result of cable reflection change) are random errors. The main systematic uncertainty error sources are:

- Finite precision and sensitivity of the power meter
- Cable loss
- Finite directivity of a directional coupler
- Power reflection from the circulator

These issues are explained in the following.

Cable calibration in a vertical test stand

To lower the measurement uncertainties in a vertical test, the VSWR mismatch and power loss of the cables need to be measured and considered in power measurements. Procedures for cable calibration in a vertical test are explained in [76] and [77]. The calibration constants due to cable loss for P_{for}, P_{ref} and P_T are C_{for}, C_{ref} and C_T, respectively. Here "*for*" accounts for incident power from the generator to the cavity; "*ref*" means power coupled out from the cavity to the generator; and "*T*" refers to power coupled out from the pickup to the power meter. An actual power is related to power meter measurement as:

$$P_{actual} = C_i P_{power.meter}, \tag{4.23}$$

where C_i can be C_{for}, C_{ref} or C_T. The cable calibration can be performed by a vector network analyzer or by an RF power injection through a reference source in one side of the cable and power measurement by a power meter on the other side.

In a vertical test, part of the cables stay inside the helium bath and their calibration is only possible from one of their sides, i.e. from the connectors placed on the cryostat top plate side. The losses of such cables are measured through a two-way return loss measurement procedure. A block diagram of cables and power meters of a vertical test is illustrated in **Figure 4.33**. In the following, an example of a possible way to calibrate cables is explained.

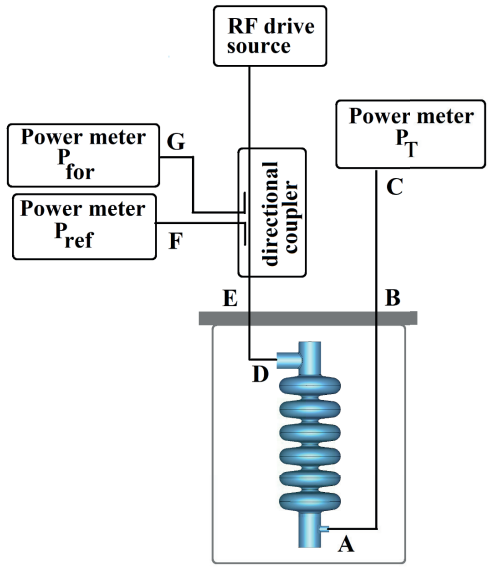

Figure 4.33. A block diagram of cables and powers meters in a vertical test

Three RF power measurements need to be corrected based on the cable loss (P_{for}, P_{ref} and P_T) and require power loss measurement along A-C, D-F and D-G lines. The power loss along A-C is obtained first by a power loss measurement along B-C and then by a return loss measurement along A-B.

- For the power loss along B-C, first the RF source needs to be directly connected to the power meter and register power as P_1. Then the reference RF source is connected to the power meter through the B-C line and registers power as P_2. The power loss along B-C is P_1-P_2.
- A two-way return loss along A-B will indicate power loss along A-B. In this case, it is required to measure the power of the reference source directly through a circulator with a power meter as P_3. Then the output port of the circulator needs to be connected to point B. The measured return loss (P_4) is two-way return loss along A-B. To limit signal flow inside the cable, it is important to have a 10 to 20 kHz frequency shift in the RF drive source with respect to the cavity resonant frequency (the cavity is partially detuned). Then the calibration coefficient along the transmission line (A-C) is equal to:

$$C_T = P_1 - P_2 + \frac{P_3 - P_4}{2}. \quad (4.24)$$

For the power loss along D-F and D-G, first the power loss along E-F and E-G will be measured followed by the power loss along D-E.

- To measure power loss along E-F, the power meter is connected to E and the reference RF source is connected as illustrated in the **Figure 4.33**. P_{for} is measured through the specified power meter for the incident signal flow. The power measured by the reference power meter is P_5, and P_{for} is P_6. The reference power meter and reference RF source are swapped and the measurement repeated. The reference power meter is registered as P_7 and P_{ref} as P_8.
- To measure power loss along D-E, connect the combination of reference RF source, directional coupler and power meters for P_{for} and P_{ref} to point E and measure the two-way return loss for the cable D-E. To limit signal flow inside the cable in this measurement, it is important to have a 10–20 kHz frequency difference between the RF drive source and the cavity resonant frequency (so the cavity is detuned and all power reflected back). In this step, the power measured by the P_{for} power meter is P_9 and that measured by P_{ref} is P_{10}. Calibration coefficients along D-F and D-G are thus equal to:

$$C_{for} = P_5 - P_6 + \frac{P_9 - P_{10}}{2}. \tag{4.25}$$

$$C_{ref} = P_7 - P_8 + \frac{P_9 - P_{10}}{2}. \tag{4.26}$$

Uncertainty due to directional coupler directivity

Based on the block diagram presented in **Figure 4.33**, the P_{for} and P_{ref} power signals are separated from each other by a directional coupler. There is some level of coupling between incident and reflection signals that are separated through a directional coupler. The amount of coupling between these two signals is determined by the directivity of the directional coupler, as explained in Appendix B. The directional coupler with higher directivity value provides better isolation between incident and reflection signals. The coupling between incident and reflection signals results in a systematic bias in P_{for}, P_{ref} and in the cavity coupling factor measurement. From equation (4.22), errors in the coupling factor measurement will affect the measurement uncertainty of the Q_0. Based on [78], the directional coupler affects the measurement uncertainty on the coupling factor as:

$$\left\langle \left(\frac{\Delta\beta}{\beta}\right)^2 \right\rangle^{\frac{1}{2}} \approx 10^{\frac{-D}{20}} \sqrt{1+\frac{(\beta+\beta^{-1})^2}{4}}, \tag{4.27}$$

for the MB cavity vertical test. The directional coupler applied[15] has directivity=35 dB and β=2.5. This results in $\Delta\beta/\beta$=0.03.

Uncertainty due to reflection from a circulator

The presence of a circulator after an RF source protects the RF source from high reflected power damages. Circulators rarely present a perfect impedance match to the transmission line connecting the load and the cavity. Reflections at the mismatch redirect energy from the reverse waveform back into the waveform incident on the cavity. Specifications for ferromagnetic circulators typically quote Voltage Standing Wave Ratios (VSWR) between 1.20 and 1.50. The magnitude of the reflection coefficient of a circulator based on its VSWR is derived as:

$$\Gamma = \frac{VSWR-1}{VSWR+1}. \tag{4.28}$$

This reflection can systematically bias the cavity decay time measurement. Energy re-reflected from the circulator can interfere constructively or destructively with the cavity field. Constructive interference will systematically bias measured decay times to values longer than the true cavity decay time. Destructive interference will systematically bias the measured decay times to shorter values. The systematic error added from circulator mismatch to the transmitted power discharge time is [78]:

$$\left\langle \left(\frac{\Delta\tau}{\tau}\right)^2 \right\rangle^{\frac{1}{2}} \approx \frac{\sqrt{2}(VSWR-1)}{(1+\beta^{-1})(VSWR+1)}, \tag{4.29}$$

for the MB cavity vertical test. The circulator VSWR is 1.2, therefore considering β=2.5 will result in $\Delta\tau/\tau$=0.09. From equation (4.22), $\Delta Q_0/Q_0$=0.09 is expected, which only include uncertainties from the directional coupler directivity and the circulator power reflection. **Figure 4.34** shows Q_0 versus E_{acc} measurement, for the MB001 cavity with tank at 2 K, with 9% uncertainty in Q_0 measurement.

[15] - The directional coupler is a Narda 3020A

The E_{acc} has a square root dependence on decay time. Thus, the error in the cavity decay time measurement has a more significant effect on the Q_0 uncertainty value than the E_{acc} uncertainty. In contrast, the power measurement error has a more significant effect on the E_{acc} value than Q_0 does. In the MB cavity prototype vertical test, frequency meter[16] accuracy for 704.42 MHz is 0.35 Hz. The power meter was Rohde & Schwarz NRP2 and the power probe was a three-path diode power sensor with 0.1 dB power measurement uncertainty.

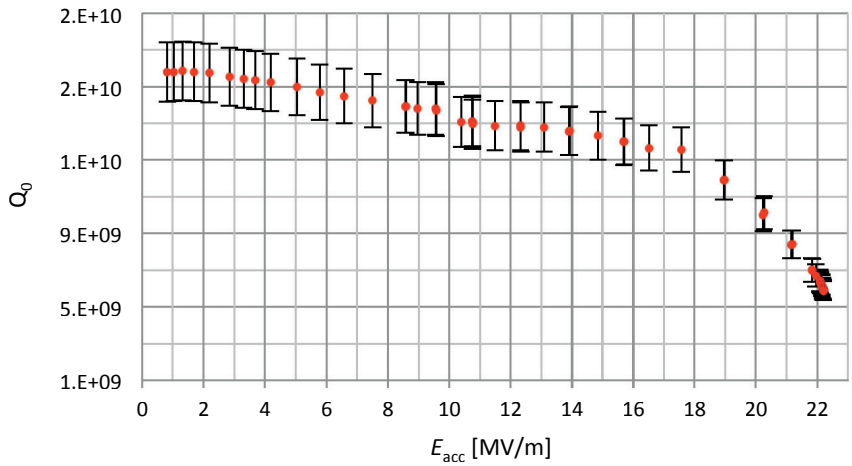

Figure 4.34. Considering 9% uncertainty in Q_0 measurement vs. E_{acc} for the MB001 cavity with tank at 2 K

[16] - The frequency meter is a Keysight 53220A

5 Higher order mode study

A charged particle beam passing through a cavity generates a wakefield. A wakefield excites the cavity's higher order mode (HOM), which can be decomposed into a series of cavity modes. These modes resonate in different frequencies and have different electromagnetic (EM) field distributions. HOMs with frequencies below the beam pipe cut-off frequency can become trapped in the cavity; these HOMs are considered and studied in this chapter. An HOM with a frequency higher than the beam pipe cut-off frequency will propagate out of the cavity. HOMs influence beam dynamics and reduce beam quality. Moreover, HOM power loss in the superconducting cavities is a concern. HOM power loss may lead to excessive heat load and early quench or extra dissipation, making the superconducting RF (SRF) cavity less efficient. Power induced by the dipoles, quadrupoles and higher order multipoles is much less than that of the monopole modes. The monopole study therefore receives more attention.

To investigate the effect of HOMs and RF errors on beam quality and stability, a series of bunch-tracking simulations were performed in [83]. This included modeling of superconducting linacs as a series of drifts and kicks. It showed that an HOM lying exactly on a machine line[17] has a critical effect and will lead to beam loss. Nevertheless, providing an HOM-free region of at least 3 MHz around the machine lines prevents significant beam quality degradation. HOMs with high R/Q that lie far enough from the machine line will not result in significant degradation in beam quality. An HOM lying exactly on a machine line is considered a trapped mode[18].

Using an HOM damper on the beam pipes placed on two sides of the cavity cells is a possible solution to couple out HOM energy. Generally, trapped modes have most of their stored energy in the middle cells of the multicell

[17] - Machine lines are created by repetition rate of bunching frequency

[18] - An explanation of how this results in a trapped mode is discussed in "HOM induced voltage section" in this chapter.

SRF cavities. This results in weak coupling to the HOM couplers, which are expensive and include extra complexities and problems such as field emission and multipacting in the vicinity of the coaxial damper [85]. Therefore trapped HOMs, with high Q_{ext}, need to be identified during cavity design. A better solution for the trapped HOM problem is to introduce some geometry change in the cavity cells and prevent the HOM frequency from crossing the machine lines. These considerations and further studies performed in [82] led ESS to build its SRF cavities without HOM dampers. Instead, ESS stipulated that HOM-free boundaries around the machine lines on its SRF cavities should be at least 5 MHz. After finalizing the ESS linac lattice, further studies in [84] showed that the specified 5 MHz HOM-free boundaries around the machine lines could be relaxed. Nevertheless, other HOM frequency shift mechanisms, such as the tuner effect on the cavity during its operation, made it reasonable to keep the 5 MHz HOM-free criteria around the machine lines.

The study of the beam dynamic effect of the transverse modes at the ESS, in [82], shows that the average beam growth due to transverse wakefield is negligible; thus transverse HOM will not be a problem for the ESS. For instance, angular offset of the cavity mechanical beam axis, compared with the cavity physical beam axis, might be much more problematic than cavity transverse HOMs.

In this chapter, HOM-induced voltage, HOM frequency distribution, and the mechanical errors effect on HOM frequency deviation from their nominal value for the ESS medium beta (MB) cavity are discussed. Further, the cavity simulation and measurement results are compared and discussed. The measurement results involve results from two prototype cavities, fabricated before serial production of the MB cavities. A brief review of HOM studies for the PIP-II LB650 cavity is presented at the end of this chapter.

5.1 HOM-induced voltage

A charged particle bunch passing through a cavity beam axis can excite all the monopole modes of the cavity. As these modes are orthogonal to each other, they can be considered separately. We assume no voltage is present in the cavity before the proton bunch passes. The HOM voltage analyses in this

section are based on the analytical explanations in [32], [86] and [87]. The induced voltage by a charged particle bunch with charge q is:

$$V_i = q\frac{\omega_i}{2}\left(\frac{R}{Q}\right)_i , \tag{5.1}$$

$$\frac{R}{Q} = \frac{\left|\int E_z(z)\, exp\left(i\omega_n z/\beta c\right)dz\right|^2}{\omega_n U} . \tag{5.2}$$

$(R/Q)_i$ is for a TM-monopole mode and is a shunt impedance of the mode normalized by the quality factor, whereas *i* refers to a specific HOM that is under consideration. Considering the induced voltage time oscillation and mode decay time effect, results in:

$$V(t) = V_i\, e^{-\frac{\omega_i}{2Q_L}t}\, e^{i\omega_i t} . \tag{5.3}$$

The first exponential term in (5.3) demonstrates voltage decay due to cavity ohmic loss and power coupled out to the cavity ports. The $2Q_L/\omega_i$ is the mode decay time (T_d). While the cavity is in a superconducting operation mode, Q_L is roughly equal to Q_{ext} for the fundamental power coupler (FPC). The Q_{ext} of the different modes is a measure of the mode power coupled out through the FPC. The study of the Q_{ext} for the cavity HOM shows that it changes over some orders of magnitude for different HOMs. Considering (5.3), the induced voltage from a continuous beam passing through the cavity is:

$$V = V_i \sum_{n=1}^{\infty} exp\left(in\omega_i T_b - n\frac{T_b}{T_{d,i}}\right) = \frac{V_i}{1-exp\left(i\omega_i T_b - \frac{T_b}{T_{d,i}}\right)} , \tag{5.4}$$

where T_b is the micropulse length. For HOM frequencies equal to k/T_b, the above equation will become:

$$V = V_i\frac{T_{d,i}}{T_b} = \frac{\omega_i}{2}\left(4.\frac{R}{Q}\right)_i I_b T_{d,i} = \left(\frac{R}{Q}\right)_i I_b Q_{L,i} . \tag{5.5}$$

This is a resonantly excited HOM by a machine line where $T_b << T_{d,i}$ and $I_b = q / T_b$ is the average beam current.

The ESS has a pulsed beam operation. The time structure for the ESS pulsed beam linac is illustrated in **Figure 5.1**. At the ESS, the bunch frequency is 352.21 MHz, resulting in a 2.84 ns micropulse length (T_b). The macropulse

time length is 2.86 ms (pulse on time), which results in 10^6 micropulses inside a macropulse. The mode decay time for a typical HOM at 1742 MHz and Q_{ext}=1.18·10^5 (this HOM will be introduced and discussed in the following sections) is 0.21 μs. As such, the induced voltage of this HOM from a microbeam pulse during the time interval between two successive micropulses will not decay, but add up with the next one. Induced voltage for a typical HOM from one macropulse with N micro-bunches inside, passing through a cavity is:

$$V = V_i \sum_{n=1}^{N} exp(i(n-1)\omega_i T_b) \,.\, exp\left(-\frac{(n-1)T_b}{T_d}\right) =$$
$$V_i(4.\frac{1-exp\,(-N\frac{T_b}{T_{d,n}}+iN\,\omega_i T_b)}{1-exp\,(-\frac{T_b}{T_{d,n}}+i\omega_i T_b)}). \tag{5.6}$$

Also, induced voltage after p macropulses pass through the cavity is:

$$V = V_i \frac{1-exp\,(4.\frac{-NT_b}{T_{d,n}}+i\omega_i\, NT_b)}{1-exp\,(\frac{-T_b}{T_{d,n}}+i\,\omega_i\, T_b)} \frac{1-exp\,(\frac{-p\,T_m}{T_{d,n}}+i\omega_i\, pT_m)}{1-exp\,(\frac{-T_m}{T_{d,n}}+i\omega_i\, T_m)}\,, \tag{5.7}$$

where T_{m} is the macro pulse length; in the ESS, this is 71 ms (14 Hz repetition rate). Considering (5.5) and (5.7), this shows that the pulsed operation mode and chopping bunch trail result in extra but weaker machine lines for HOM frequencies equal to k/T_m. These are called chopping machine lines.

Excitation of an HOM induces voltage and transfers power to the cavity. Induced power will dissipate on the cavity wall, affecting the beam passing through the cavity and part of it will couple out through the cavity ports. Transferred HOM power to the beam results in beam instability. Moreover dissipated power on the cavity wall and power coupled out by the cavity ports are:

$$P_{c,i} = \frac{V(t)^2}{R_i} = \frac{V(t)^2}{(4\frac{R}{Q})_i\, Q_{0,i}}\,, \tag{5.8}$$

$$P_{ext,i} = \beta\, P_{c,i} = \frac{V(t)^2}{(4\frac{R}{Q})_i\, Q_{ext,i}}\,. \tag{5.9}$$

Considering (5.5), for a resonantly excited HOM, turn (5.8) and (5.9) to:

$$P_{c,i} = (4.\frac{R}{Q})_i I_b^2 \frac{Q_{L,i}^2}{Q_{0,i}} \approx (\frac{R}{Q})_i I_b^2 \frac{Q_{ext,i}^2}{Q_{0,i}} \ , \tag{5.10}$$

$$P_{ext,i} = (4.\frac{R}{Q})_i I_b^2 \frac{Q_{L,i}^2}{Q_{ext,i}} \approx (\frac{R}{Q})_i I_b^2 \, Q_{ext,i} \ . \tag{5.11}$$

This shows how an HOM will be excited and induces power in the cavity. Such an HOM is considered a trapped mode.

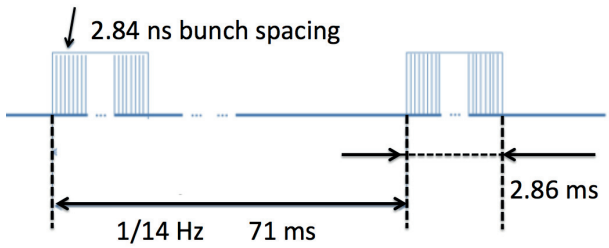

Figure 5.1. ESS Beam time structure in pulsed beam operation

5.2 HOM frequency spectrum

The ESS medium beta cavity beam pipe radius is 68 mm; its cut-off frequencies (f_{cut}[19]) for the TE_{11} and TM_{01} modes are 1.29 GHz and 1.69 GHz, respectively [79]. To find trapped modes inside the cavity, Superfish and CST are used to determine the HOM spectrum up to 1800 MHz. Simulations are performed by putting an electric wall boundary condition on the beam pipe ends. To reduce the mesh number, a symmetry plane passing through the middle of the beam pipes, cavity cells and FPC is considered. **Figure 5.2** shows the frequency spectrum and Q_{ext} of the HOMs derived by the CST; the different TE and TM modes are also distinguished from each other. The HOMs have a wide frequency spectrum, but our focus is on the monopoles that are close to the machine lines. The closest TM modes to the ESS machine lines are distinguished and specified in Table 5.1. To specify the distance of the modes from the machine lines and mode type, a short comment on the HOMs and on the 703.6 MHz mode (same order mode (SOM)) is made in Table 5.1. There are six TM_{010} modes in the first cavity

[19] - f_{TE-cut}= 1.841c/2πr and f_{TM-cut}= 2.405c/2πr

passband, frequency difference is small and modes are close to the cavity π-mode. The R/Q of these modes are derived as a function of the particle's relative velocity to the speed of light (β) and demonstrated in **Figure 5.3**. Only the R/Q of the 5/6 π mode at the beginning and end of the β range gets close to the R/Q of the π mode.

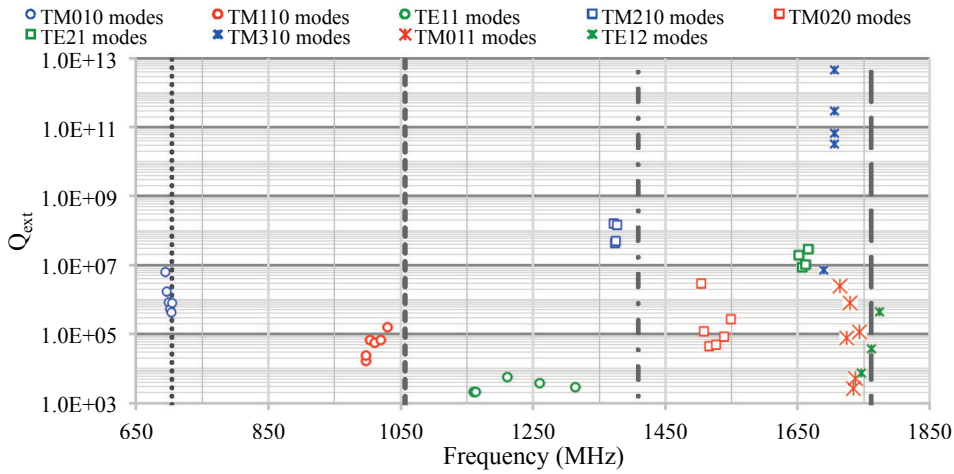

Figure 5.2. Frequency spectrum and Qext of MB cavity HOMs up to 1900 MHz derived by CST

Table 5.1.
Modes close to ESS machine lines in MB cavity

Superfish (MHz)	CST (MHz)	Comments
703.6	703.69	> TM010, 0.8 MHz from accelerating mode
1029.6	1029.65	> TM110, 26MHz from 3rd machine line
1376.7	1376.71	> TM210, 32MHz from 4th machine line
1742.7	1742.58	> TM011, 19MHz from 5th machine line

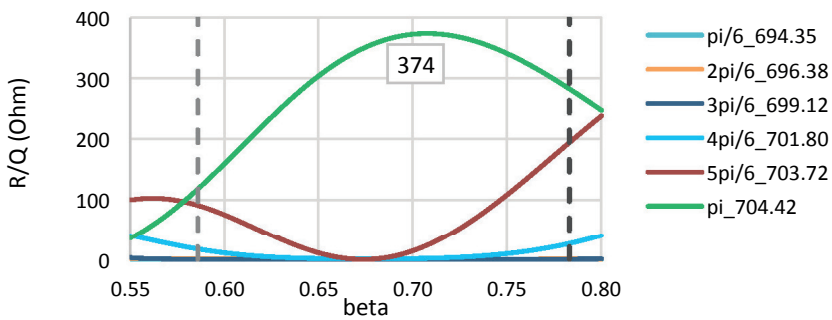

Figure 5.3. R/Q vs beta for TM_{010} modes derived by Superfish

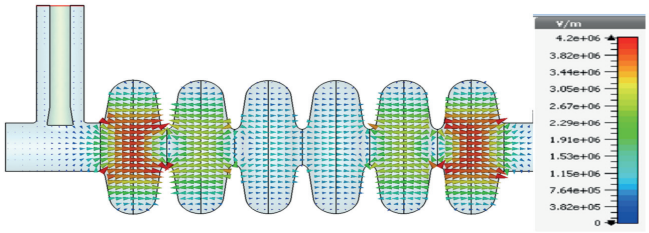

703.69 MHz, TM_{010}

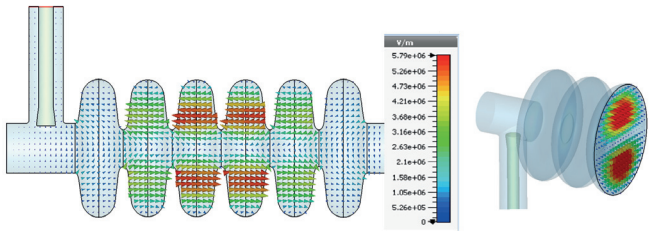

1029.65 MHz, TM_{110}

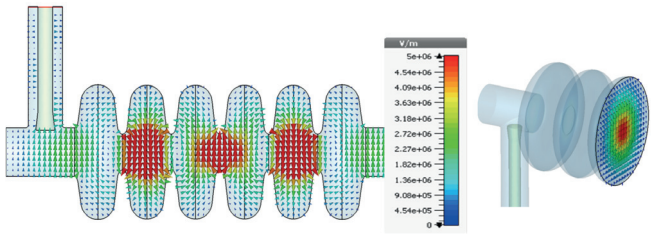

1314.12 MHz, TE_{11}

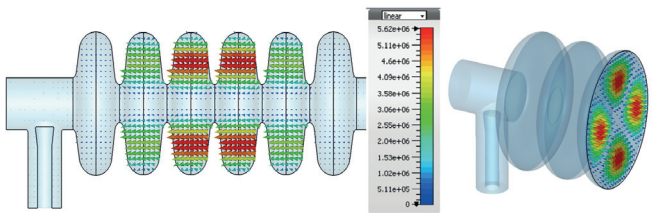

1376.71 MHz, TM_{210}

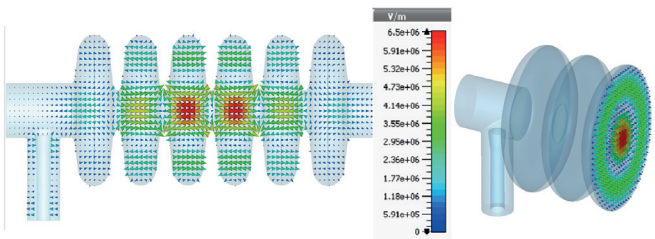

1549.20 MHz, TM_{020}

Figure 5.4. *E*-field configuration for 703.69 MHz, 1029.65 MHz, 1314.12 MHz, 1376.71 MHz and 1549.20 MHz HOMs

Figure 5.4 and **Figure 5.5** show the *E*-field configuration of the HOMs that are found in **Figure 5.2**. For each HOM band, only the last mode is presented, with the mode frequency and name. For instance, the TM_{011} HOM band is composed of six modes, but only the *E*-field configuration of the last mode in this band is shown. Even the TE_{12} modes are closer to the fifth machine line (one of them crossing the fifth machine line), but transverse modes are not the source of beam instability at the ESS. Considering the explanations demonstrated up to this point, the 1742.58 MHz TM_{011} monopole could be counted as a dangerous mode for the MB cavity due to its proximity to fifth machine line. This mode can increase cavity loss and degrade the quality of the proton beam if it is shifted on the fifth machine line.

5.3 Effect of mechanical error on HOM frequency deviation

There are different steps in fabricating the elliptical cavity, from the niobium sheet deep drawing to welding cavity parts to each other. To prevent too great a price rise in the cost of cavity fabrication, 0.2 mm shape and 0.1 mm length tolerances are inevitable. Higher mechanical errors in the order of 1 mm are also possible in some dimensions after cavity field flatness tuning and helium tank weld. After welding all cavity parts to each other with EBW, accelerating mode frequency and field flatness are tuned by stretching or squeezing the cavity cells. Stretching and squeezing of the cavity cells to tune the accelerating mode frequency and field flatness could result in significant changes in the HOM frequencies. The amount of cell stretching or squeezing is determined by the bead-pull measurement.

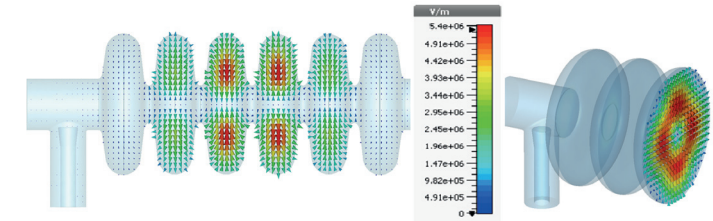

1666.11 MHz, TE_{21}

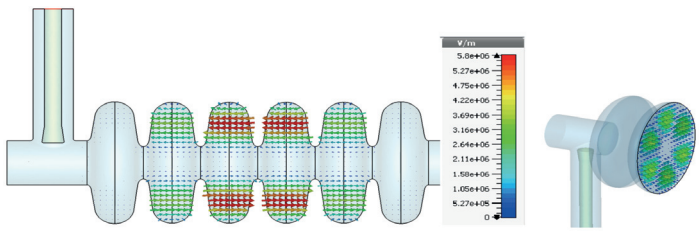

1705.58 MHz, TM_{310}

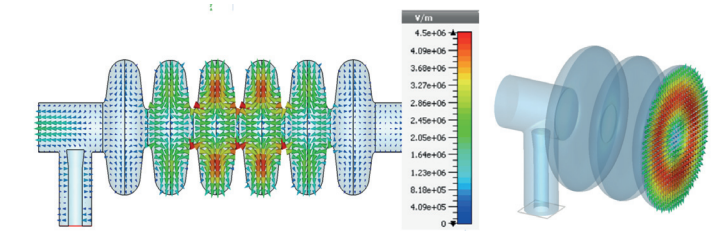

1742.58 MHz, TM_{011}

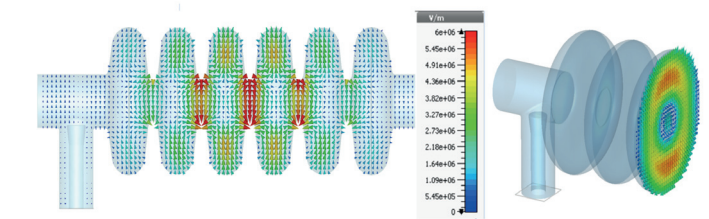

1773.84 MHz, TE_{12}

Figure 5.5. *E*-field configuration for 1666.11 MHz, 1705.58 MHz, 1742.58 MHz and 1773.84 MHz modes

To make a preliminary estimation of the effects of possible cavity geometry change on the accelerating mode (TM_{010} mode) and on the 1742 MHz mode (TM_{011} mode) that is distinguished as the dangerous mode, a single-cell elliptical cavity is assessed. **Figure 5.6**[20] illustrates seven independent

[20] - Same as **Figure 4.1** with less geometry parameters

geometrical parameters of an elliptical half-cell cavity. In the assessment, each of these parameters is changed separately and their influence on the frequency deviation of TM_{010} and TM_{011} modes of the cavity are analyzed. In each geometry parameter study, the rest of the geometrical parameters are kept at their nominal value. **Figure 5.7** shows the *E*-field patterns of the single cell cavity for these two modes. Table 5.2 shows a summary of the geometry error study for a single cell cavity. The change in geometrical parameters has a linear effect on the frequency change of the TM_{010} mode. Frequency changes for TM_{010} and TM_{011} modes due to the error in the cavity geometry are not always in the same direction (L, a and b), nor in the same order. Changes to the TM_{011} mode are more severe than those to the acceleration mode. Values in Table 5.2 are in agreement with the results reported in [90]. These results show that parameters A, and partially B, have a more intense effect on the TM_{011} frequency change than TM_{010}. A and B both belong to the magnetic field region of the cavity. This is compatible with the Slater perturbation theory. Considering [91], perturbing A and B results in bigger perturbation in the EM energy for the cavity in the TM_{011} mode than the TM_{010} mode, leading to a higher frequency change for the TM_{011} mode as a result.

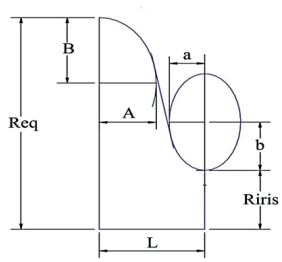

Figure 5.6. Schematic of 7 independent geometrical parameter in an elliptical cavity

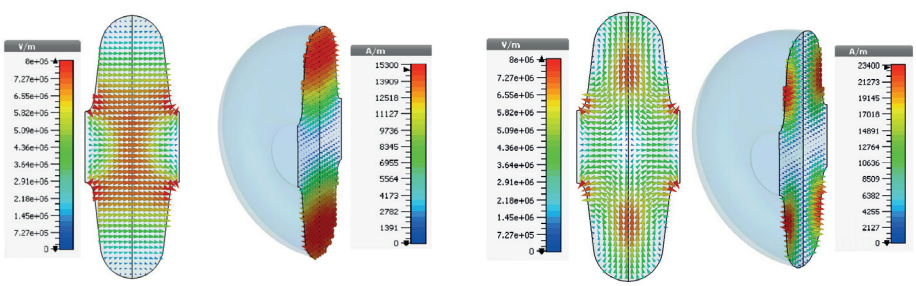

Figure 5.7. *E*-field and H-field patterns for (Left) single cell TM010 mode, (Right) Single cell TM011 mode

Table 5.2.
Frequency shift of 1st and 3rd modes in a single cell elliptical cavity

	1st monopole band (MHz / mm)	3rd monopole band (MHz / mm)
A	-0.03	-0.2
B	0.009	0.03
L	0.02	-0.08
a	-0.02	0.07
b	0.004	-0.005
R_{eq}	-0.04	-0.03
R_{iris}	0.01	0.01

The frequency change due to the EM energy change is given by:

$$\frac{\Delta\omega}{\omega} = \frac{\int_{\Delta V}(4.\mu_0 H^2 - \varepsilon_0 E^2)dV}{\int_V (\mu_0 H^2 + \varepsilon_0 E^2)dV} = \frac{\Delta U}{U} \quad . \tag{5.12}$$

Experimental measurements for two 5-cell elliptical cavities[21] mentioned in [92] showed a 16 MHz HOM frequency shift for both cavities despite the correspondence of measured accelerating mode characteristics with ESS requirements. Furthermore the 16 MHz frequency shift was observed on the HOM that was considered a dangerous mode for the 5-cell cavity. All these considerations clarify the importance of a systematic error study in a multicell elliptical cavity to be able to predict a possible frequency change of dangerous HOM. Such an error study will provide the amount of dangerous HOM frequency changes due to typical mechanical errors, as well as uncertainties due to surface treatment chemistry and field flatness tuning. Besides, the error study will distinguish geometrical parameters that are susceptible to result in intense frequency changes on dangerous HOMs.

5.3.1 Systematic error study

This section explains the systematic error study of the 1742 MHz (TM_{011}) HOM for the ESS MB cavity. When considering the six cells of the cavity, and large number of degrees of freedoms, it is of value to introduce certain assessment routines to simplify the entire error study. In this assessment[22]:

[21] - ESS high beta prototype cavities

[22] - Main steps of error study are distinguished by bullets

- In the first step, the end-cell of the cavity with its beam pipe will be separated from the cavity structure and be analyzed separately.
- The end-cell will be perturbed by one of its geometrical parameters (illustrated in **Figure 5.6**), except cell length, while the other geometries are at their nominal values. This perturbation will deviate the TM_{010} mode resonant frequency of the cell from its nominal value.
- The end-cell will then be tuned back to its nominal TM_{010} mode frequency before perturbation by cell stretching or squeezing. At this point, even the end-cell is perturbed and retains the nominal TM_{010} mode frequency, but the frequencies of its HOMs are no longer at their nominal values.
- For the next step, the modified cell will be put back in its position in the MB cavity structure. Now, instead of a single cell simulation, the total MB cavity is stimulated.

Even the end-cell is different from its nominal design dimensions, but as all the cells of the cavity are still in their nominal accelerating mode frequency, the frequency and the *E*-field flatness of the π mode on the 6-cell cavity will be roughly similar to the nominal. In this case, implemented perturbation will show its effect on the cavity HOMs. Our methods enable us to measure the 1742 MHz mode frequency change due to a predefined error in the end-cell. In this case, stretching or squeezing the end-cell to tune it back to its nominal frequency is similar to cavity field flatness tuning in the cavity fabrication.

- This procedure can be repeated by inserting an error into the other geometrical parameters of the end-cell.
- This same procedure can be repeated on the second and third cell of the cavity.

Based on the existing symmetry in the cavity geometry, and in the 1742 MHz HOM field distribution, it would be enough to perform the above-mentioned geometrical error study on only the first three cells of the cavity. Table 5.3 shows a summary of the error study results achieved by the CST. As illustrated, cell 3 has the highest sensitivity, and cell 1 the lowest, for the 1742 MHz frequency change due to mechanical errors. This is completely consistent with the 1742 MHz mode (TM_{011}) *E*-field pattern in **Figure 5.5**. From the Slater theory and equation (5.12), we conclude that the geometry perturbation in regions with the higher electric or magnetic field results in a

greater unbalance in the cavity's stored energy. As a result, a greater frequency change will occur. This could be used in cavity fabrication by placing dumbbells with lower mechanical errors in the central cells, and placing other dumbbells close to the end-groups to reduce the mechanical error effect on the 1742 MHz mode frequency change. Considering a 0.2 mm tolerance on all six geometrical parameters assessed in Table 5.3, adding them together, and considering the effect of the other half of the cavity leads to a less than 6.3 MHz mode frequency change for the 1742 MHz mode. This result is consistent with the Sundelin study (summarized in [93]) on SNS cavities to obtain a statistical estimation of the possible HOM frequency shift by:

$$\frac{f_{meas}-f_{sim}}{f_{sim}} \leq 0.0038\ , \tag{5.13}$$

due to mechanical errors and π-mode frequency tunings. The existing 19 MHz frequency gap between the 1742 MHz mode and the fifth machine line is sufficient to be confident that the standard mechanical tolerances during MB cavity fabrication will not excite a monopole mode in the 5 MHz boundary of the machine lines.

Table 5.3.
1742 MHz mode frequency shift due to geometrical errors on the first 3 cells of the MB cavity (kHz/mm)

	cell 1	cell 2	cell 3
R_{eq}	-40	-3300	-7200
R_{iris}	80	940	2100
A	-150	-2800	-7800
B	50	960	2200
a	-35	-190	-400
b	20	110	250

5.3.2 Measurement results

Before starting serial production of 36 MB cavities, two cavities were produced [94] with fine grain and large grain niobium material. In this section, the measurement results related to these two prototypes are discussed and compared with simulation results. The HOMs for both of the fine grain and large grain cavities are considered to measure the 1742 MHz mode. **Figure 5.8** illustrates measured S21 for both cavities. Measurement is performed after BCP, the first field flatness tuning, and while the cavity was at room temperature and filled with air.

Frequency deviation in HOMs due to mechanical errors is different from one HOM to another one. This is because of HOMs dissimilar sensitivity to various geometrical errors. Considering [92], the frequency deviation of HOMs from nominal values might be in the order of 16 MHz.

A reliable tool for detecting a specific HOM is to measure its axial *E*-field profile by bead pulling and compare it with the simulation field profile. Here, we first assess the 1738.7 MHz and 1732 MHz modes for the fine grain cavity. Next, we consider the 1728 MHz mode for the large grain cavity. Considering equations (4.3) and (4.4), the frequency changes of the 1742 MHz mode due to geometry shrinkage (temperature drop from 300 K to 2 K) and dielectric change are -2.54 MHz and +550 kHz, respectively. The expected frequency for this mode without considering mechanical errors and BCP effect is thus 1740.08 MHz. In **Figure 5.8**, the closest detected mode to 1740.08 MHz for the fine grain cavity is measured at 1738.7 MHz.

Figure 5.9 shows schematic view of the *E*-field distribution for the 1742 MHz mode, simulated axial *E*-field on the cavity axis for the 1742 MHz mode and bead-pull measurement for the 1738.7 MHz mode on the cavity axis. In **Figure 5.9**(c), placing the π-mode axial *E*-field measurement in the background allows better distinction on the HOM field variation over the six cells of the cavity. From the vicinity of frequency and similar field profiles, we believe that the 1738.7 MHz mode in **Figure 5.8**, is the TM_{011} mode. To increase the mode perturbation and sensitivity of the bead-pull measurement to the *E*-field changes on the cavity axis, a short and thick bead was used.

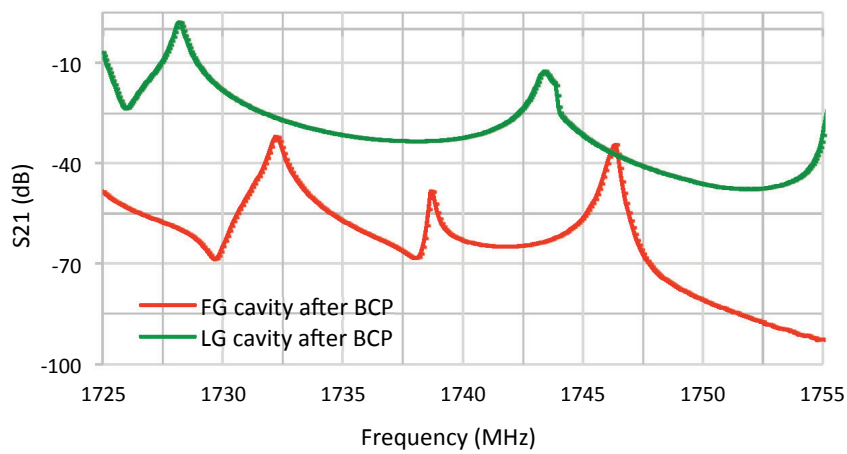

Figure 5.8. S21 measurement for fine grain and large grain cavities by VNA

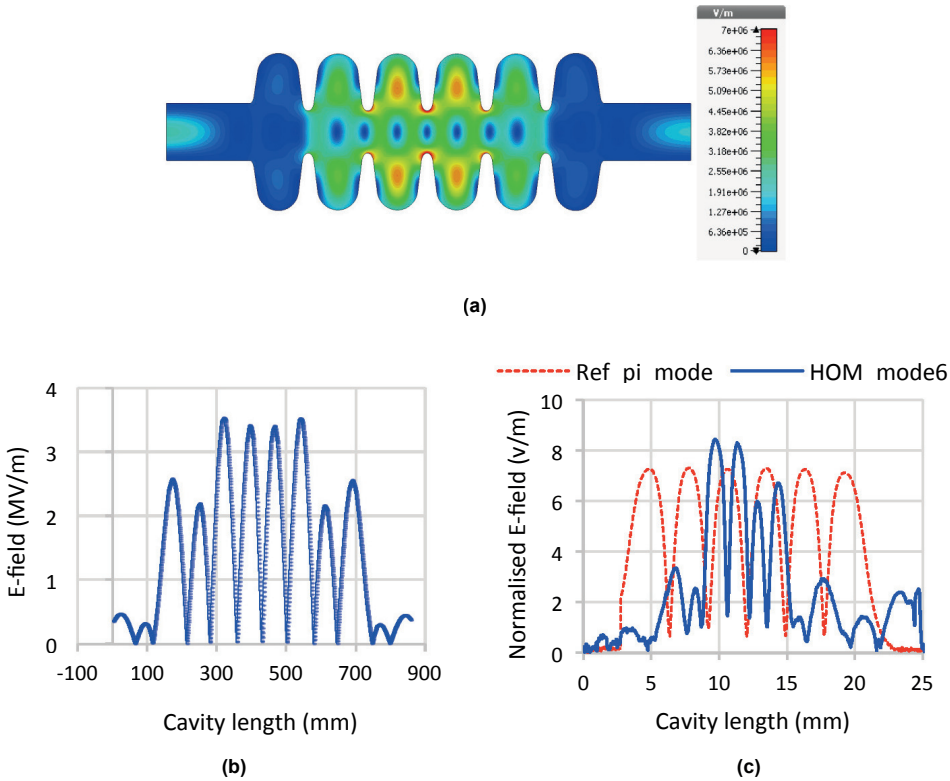

Figure 5.9. (a) 2D *E*-field pattern of the 1742 MHz mode, (b) simulated axial *E*-field result for the 1742 MHz mode, (c) Bead-pull measurement for 1738.7 MHz mode on cavity axis with π-mode axial field measurement in the background.

The other HOM frequency investigated from the fine grain cavity S21 measurement is 1732 MHz. **Figure 5.10** (c) shows the measured *E*-field on the cavity axis for this mode. If we only consider the mode frequency in ideal conditions with no geometry error, this mode is expected to be one of the TM_{011} modes. However, looking at the *E*-field pick-ups in the first, second, fourth, sixth and seventh irises, we believe this is the first TE_{12} mode with 1746 MHz (at 2 K and vacuum), as indicated in **Figure 5.2**. Including the temperature and dielectric change in the frequency result in the -2.55 MHz frequency change, there is roughly an 11 MHz frequency decrease for the TE_{12} mode. **Figure 5.10** (a) and (b), show *E*-field distribution of the 1746 MHz mode and the absolute component of simulation result for the *E*-field on the cavity axis.

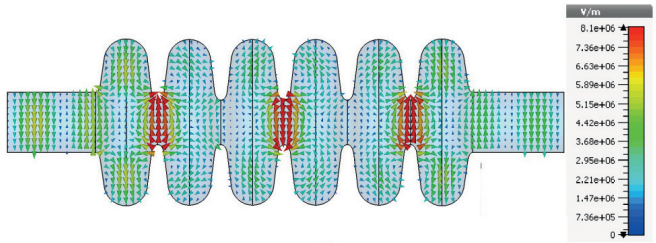

(a)

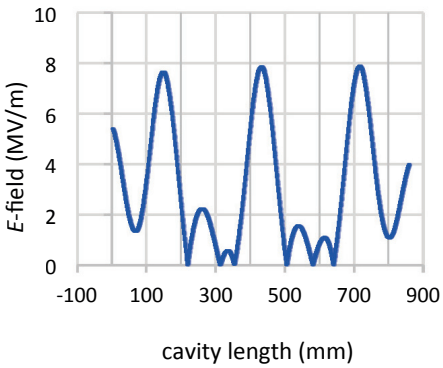

(b)

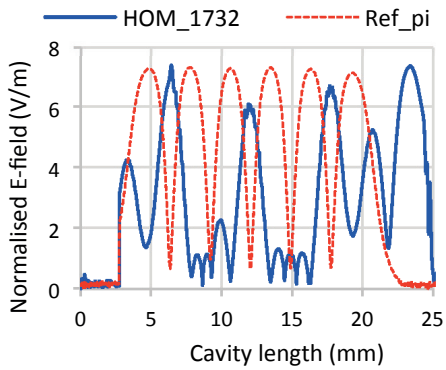

(c)

Figure 5.10. (a) *E*-field distribution of the 1746 MHz mode, (b) Absolute component of *E*-field on cavity axis (beam pipe field is not included), (c) Bead-pull measurement for *E*-field on cavity axis with π-mode axial field measurement in the background.

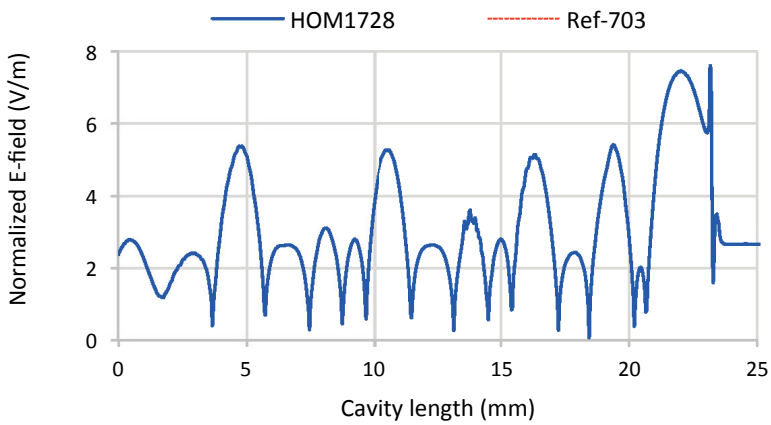

Figure 5.11. Bead-pull measurement for 1728 MHz mode *E*-field on cavity axis with π-mode axial field measurement in the background.

In the large grain cavity, we did not succeed in directly measuring the dangerous monopole TM_{011} mode. This mode is mainly concentrated in the middle cells of the cavity, and there is a low level of its *E*-field on the cavity beam pipe ports. To assess the HOMs of the large grain cavity, the 1728 MHz mode is measured using bead-pull. The 1728 MHz mode is similar to the 1732 MHz mode in the fine grain cavity mentioned above, but has a weaker *E*-field on its first iris. For the large grain cavity, the first TE_{12} mode frequency is the 15 MHz shifted down. **Figure 5.11** shows the bead-pull measurement for this mode's *E*-field in the large grain cavity. Due to the existing schedule for the vertical test of the cavities, there was insufficient time for a further HOM and bead-pull measurement.

Figure 5.12 illustrates the wide band HOM frequency measurement results for the fine grain cavity at 2 K, around the ESS's third, fourth and fifth machine lines. As predicted by simulation, there is no HOM close to the third and fourth machine lines. A 2.55 MHz frequency increase was expected for the 1738.7 MHz due to temperature and dielectric change. As such, the 1741 MHz mode, encircled by a red ellipse near the fifth machine line, is the mode tracked as the TM_{011} mode at room temperature via a bead-pull measurement. Three other modes are closer than the encircled mode to the fifth machine line. Taking the simulation results and further axial field measurements on the cavity, we see that these modes are not monopole and, as explained, will not cause concern.

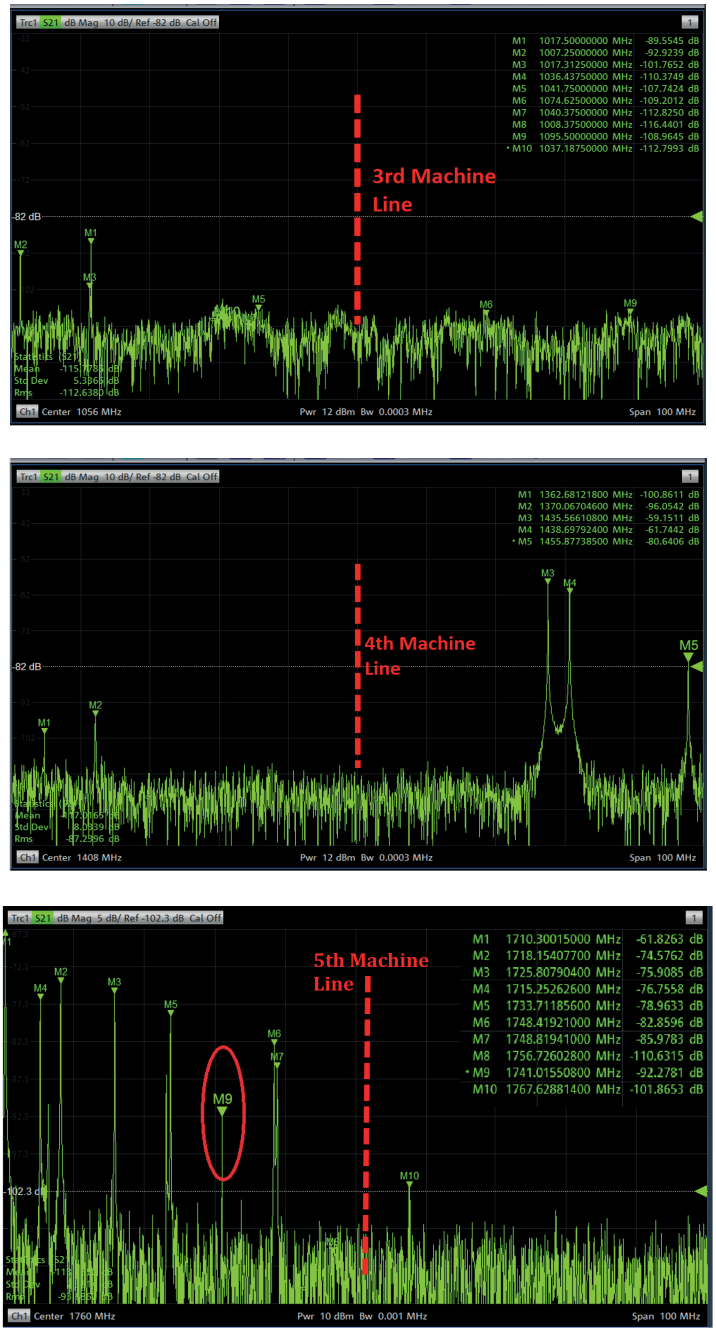

Figure 5.12. FG MB cavity wide band HOM measurement result at 2K around ESS (a) third, (b) fourth and (c) fifth machine lines.

5.4 HOM study for PIP-II LB650 cavity

The Proton Improvement Plan-II (PIP-II), the upgrade project for the Fermilab accelerator complex, will support a world-leading neutrino program over the next several decades by delivering the world's most intense beam of neutrinos to the international LBNF/DUNE project [95]. Involving substantial international participation, it has five types of SC cavities placed in a cryomodule. This section is a short overview of the HOM characteristics of the 650 MHz cavity with β=0.61, called LB650. The main RF parameters of the cavity are illustrated in Table 5.4. In this section, however, only the HOM characteristics of the LB650 cavity are discussed. The cavity beam pipe radius is 59 mm, with a cut-off frequency for TM_{01} of 1945 MHz. HOMs with a frequency below f_{cut} can become trapped in the cavity. The SRF linac section bunch repetition rate is 162.5 MHz. As mentioned above, the main HOM concerns are beam instabilities and their induced cryogenic loss. In PIP-II, due to the relatively low beam current (2 mA in SRF linac), we do not expect beam instabilities as a result of HOM to lead to a significant degradation in beam quality. However, cryogenic loss induced by monopole HOMs close to the machine lines must be specifically considered. Monopole HOMs around the machine lines are required to fulfill [96]:

$$\frac{R}{Q}Q_{ext}^2 \ll 3\times10^{16}. \tag{5.14}$$

Table 5.4.
RF parameters of the 650 MHz cavity

Parameters	Value
Frequency (MHz)	650
$G\ (\Omega)$ @ β_{opt}	193
β_{opt}	0.65
E_{peak} / E_{acc} @ β_{opt}	2.4
$R/Q\ (\Omega)$ @ β_{opt}	340

Based on this, all HOMs in the LB650 cavity up to f_{cut} are searched for to track trapped monopole HOMs. The study shows that below f_{cut}, two pass bands of monopoles are close to the machine lines. A power loss effect of these two bands, and their resonance excitation, are assessed. CST and Superfish are used for the R/Q and Q_{ext} calculations related to these HOMs. **Figure 5.13** illustrates the calculated $Q_{\text{ext}}{}^2 \times R/Q$ for these monopoles HOMs.

They are all much smaller than 3×10^{16}. Furthermore, the 1470.5 MHz and 1618.5 MHz modes may become trapped in the middle cells of the cavity. The 1618.5 MHz mode may also have the highest power loss. **Figure 5.14** illustrates the *E*-field simulation configuration for both of these modes.

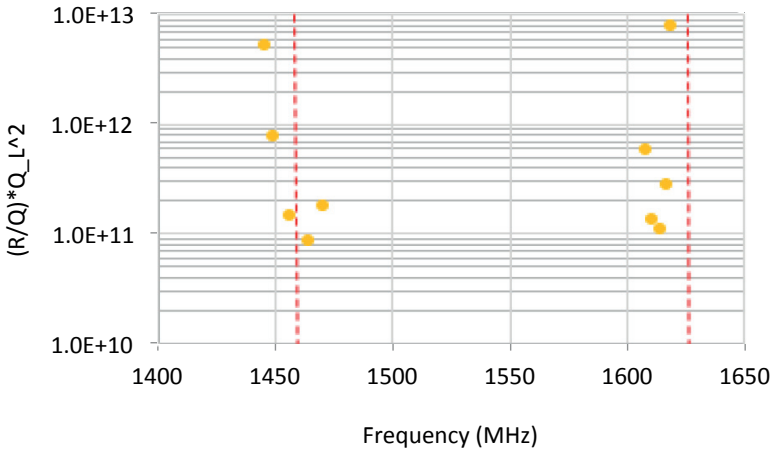

Figure 5.13. Calculated $\frac{\mathbf{R}}{\mathbf{Q}}\mathbf{Q}_{\mathbf{L}}^{\mathbf{2}}$ for the two HOM monopoles bands under $\mathbf{f}_{\mathbf{cut}}$ frequency

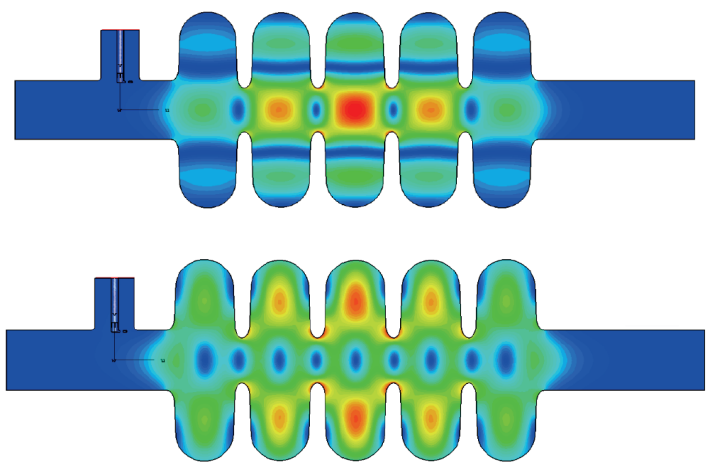

Figure 5.14. *E*-field configuration of (Up) 1470.5 MHz monopole HOM (Down) 1618.5 MHz monopole HOM mode.

6 Field Emission

One of the important limitations in increasing a cavity-accelerating gradient (E_{acc}) is field emission. This is the emission of electrons from regions with a high surface *E*-field. Emitted electrons absorb RF power, can generate dark current, increase cavity losses, generate radiation and even push the cavity to quench. The cavity surface *E*-field decreases the level of the work function barrier on a metal surface, so electrons of metal, due to their quantum-wave-like nature, will be able to tunnel out into a vacuum. The Fowler-Nordheim study for field emission current calculation, explained in [75], resulted in:

$$j(E) = \frac{A_{\mathrm{FN}} E^2}{\phi} exp\ (-\frac{B_{\mathrm{FN}} \phi^{3/2}}{E}) \tag{6.1}$$

j (A/m^2), ϕ and E are the emission current density, metal work function (eV) and the surface *E*-field (MV/m) respectively; A_{FN}=1.54×10^6 and B_{FN}=6.83×10^3 are current density constants. Experimental results on the SRF cavities demonstrate that there is a functional dependence between the Fowler-Nordheim prediction for the field emission current and the *X*-ray intensity outside of the cavity, but measurement results are much higher than the predicted value. To improve the Fowler-Nordheim prediction, a factor called field enhancement factor (β_{FN}) is introduced. Thus, β_{FN}E replaces E in the Fowler-Nordheim field emission current prediction. Then, the Fowler-Nordheim field emission current changes to:

$$I(E) = \frac{A_{\mathrm{FN}} A_e (\beta_{\mathrm{FN}} E)^2}{\phi} exp\ (-\frac{B_{\mathrm{FN}} \phi^{3/2}}{\beta_{\mathrm{FN}} E}) \tag{6.2}$$

I= jA_e is the current from the emitter and A_e is the effective emitting area. The field enhancement factor is related to the physical properties of an emitter. Certain sites on the inside surface of the cavity with a sharp projection or jagged surface enhance the surface *E*-field. The field-emitting particles have irregular shapes so both β_{FN} and A_e are empirical parameters. Considering studies summarized on [75] based on the properties of the

emitter, β_{FN}, and A_e could stay between 10–300 cm^2 and 10^{-15}–10 cm^2, respectively. As the cavity *E*-field oscillates, a sine wave for the *E*-field vs. RF phase results in a change in field emission current density over time. In **Figure 6.1**, we demonstrate the *E*-field and RF phases by applying the Fowler-Nordheim current density estimation for the ESS MB cavity, and by considering β_{FN}= 100 and ϕ= 4 eV as functions of the cavity surface. There is an exponential change versus the surface field, with an approximate Gaussian trend versus the RF phase. Considering 100 for β_{FN} is just a logical estimation (between 10 and 300); values higher than 100 result in a steeper slope of the current density increase, whereas lower values result in the opposite. The current exponential density increase starts from 35 MV/m, which is equivalent to E_{acc}=13.7 MV/m. Considering fabricated prototypes and cavities available from serial production, four cavities present a field emission start of 14–16 MV/m [97]-[98], which is a good Fowler-Nordheim estimation for the exponential increase in field emission current (Table 6.1). Enhancing the surface *E*-field, in addition to an exponential growth in the emission current density, also results in a significant increment in the density of field emitting sites. Thus, in the presence of the field emission, it becomes difficult to raise the field level without processing emitter sites. This clarifies the importance of clean room assembly, chemical etching, and HPR to minimize the presence of emitters on the cavity surface.

An intense field emission results in a Q_0 drop with a sharp slope. *X*-ray measurement and temperature maps are typical diagnostic tools that detect field emission. Placing thermometers on the external wall of the cavity can show the heat resulting from the field-emitted electrons bombardment. Intense field emission can even result in thermal breakdown. Metallic particles are common emitters in SRF cavities. Copper, stainless steel, iron, and titanium are some typical metallic field emitters that can be tracked to various stages of cavity production. Copper may come from the RF probe tips or copper gaskets; stainless steel and iron may come from vacuum pipes or assembly tools; and titanium may come from sputter ion vacuum pumps. Silicon and carbon are two possible non-metallic field emitting contaminations that may exist on the cavity surface. The field emitted electrons accelerate and receive energy through the *E*-field of the cavity mode. Furthermore, as demonstrated in (6.2), an emission current depends on the properties of the emitter. At this point, the impact energy of electrons and radiation generated due to their impact depend on the cavity field and properties of the emitter.

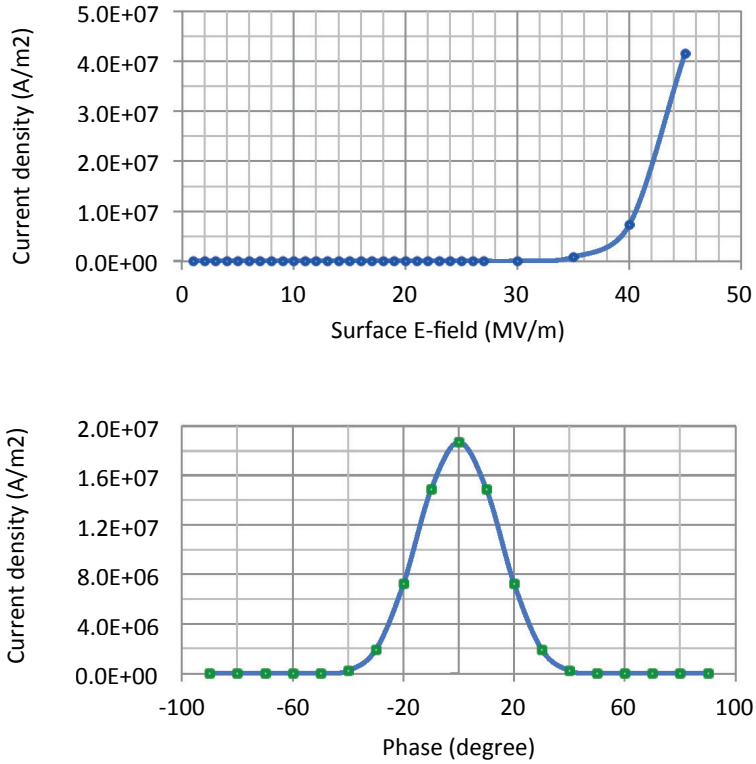

Figure 6.1. Fowler-Nordheim current density with respect to (Up) surface *E*-field, (Down) RF phase

This chapter provides a detailed understanding of the dynamics of the field emission in the MB cavity and its subsequent X-ray radiation. Although diagnostic tools for the electron activity inside the cavity are limited, computer simulation can be used to gain a deeper overview. Electron tracking by CST [59] is used to study an electron's trajectory and its impact energy. To provide an overview of the field emission for the ESS MB cavity, the field emissions for different emitter locations with different RF phases are checked. The goal of this study is to compare different possible emitter regions and the impact energy of emitted electrons with the number of electrons with the same impact energy from the emitters (to evaluate radiation dosage). Cavity field emission is simulated for 10 MV/m and 16.7 MV/m accelerating gradients because available field emission measurement results in these two accelerating gradients for the MB cavity. Both

measurements are used to check the process developed for calculating the maximum electron impact energy due to field emission.

Table 6.1.
List of cavities with exponential field emission rise around the Fowler-Nordheim estimation

Cavity	E_{acc} of cavity in field emission start (MV/m)
Fine grain prototype	16
M005 (CEA prototype for rototype cryomodule)	15
M005-CM01 (LASA series production)	15
M006-CM01 (LASA series production)	14

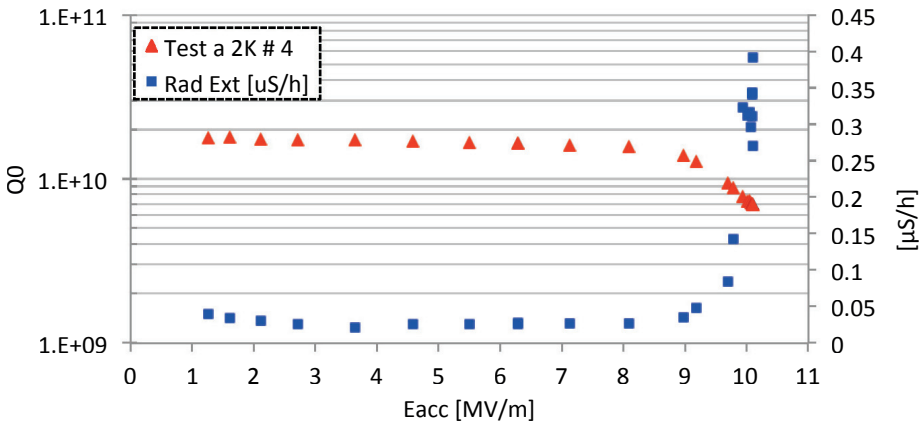

Figure 6.2. Q and radiation dose vs. E_{acc} for the LG cavity pi-mode **[99]**

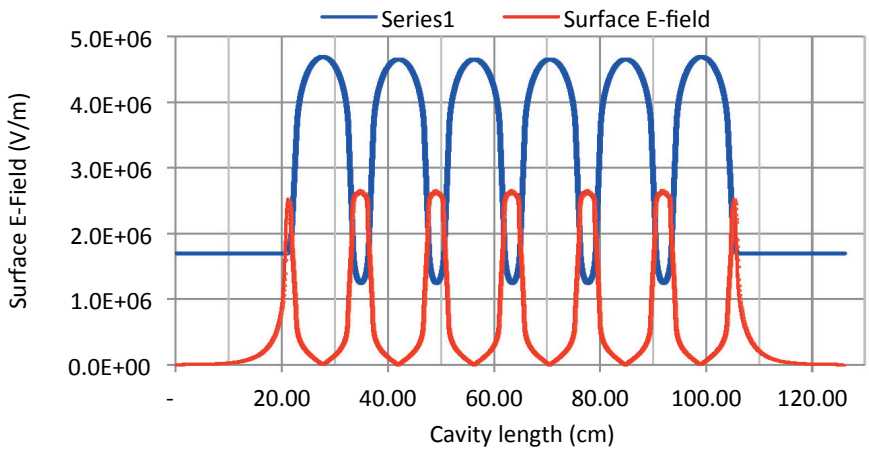

Figure 6.3. Projected MB cavity π-mode surface *E*-field (red line) on the cavity 2D geometry pattern (blue line)

6.1 MB cavity π-mode field emission

As explained, serial production of the MB cavities began after the fabrication and test of two prototype cavities. The fine grain cavity was tested up to E_{acc}=22 MV/m, but the large grain cavity quenched at 10 MV/m. **Figure 6.2** shows the Q and radiation dose of the large grain cavity versus E_{acc}. Up to 8 MV/m there is an almost flat Q curve. However, an exponential rise in field emission appears, followed by a Q drop and quench.

6.1.1 Simulation, data analysis and measurement

The cavity surface *E*-field is one of the two essential issues in driving field emission. Therefore, the calculation of the cavity surface *E*-field over the cavity geometry is the first consideration in the field emission study. **Figure 6.3** is the projected cavity π mode surface *E*-field on the MB cavity 2D geometry. It illustrates that the maximum cavity surface *E*-field is on the cavity irises and that there is a very steep slope change in the surface *E*-field from the iris to the equator. This issue may result in first-step simplification in the cavity field emission study by considering the area of the iris that occupies roughly 70% of the surface *E*-field. Therefore, 20 mm on each side of each iris symmetry plane (40 mm for each iris) is considered an active field emission area. Each 20 mm around an iris symmetry plane is studied separately. CST particle tracking is applied for the cavity π mode field emission study. The particle-tracking solver in CST calculates the movement of emitted electrons from the cavity surface based on the EM field of the cavity π mode. The particle tracking code uses the following relativistic equations of motion for tracking an electron with charge *q* and mass *m*:

$$\frac{dr(t)}{dt} = \frac{1}{\gamma}u(t), \tag{6.3}$$

$$\frac{du(t)}{dt} = \frac{q}{m}(E(r,t) + \frac{1}{\gamma}u(t)\times B(r,t)), \tag{6.4}$$

$$\gamma = \frac{1}{\sqrt{1-(\frac{v}{c})^2}}. \tag{6.5}$$

r(t) is an electron 3D position at time t, *E*(r,t) is an electric field, *B*(r,t) is a magnetic field, *v*(t) and *u*(t) is electron velocity (*v*(t)=*u*(t)/γ). The electron

track under the cavity field effect will continue until the trajectory crosses one of the cavity boundaries. As part of the particle-tracking settings, there is a homogeneous distribution of roughly 600 electrons on each side of the iris symmetry plane (1200 on each iris). A second simplification is to consider four irises as the active field emission area. Based on the symmetry in the cavity geometry and the π mode field distribution, we expect a similar field emission result for the symmetric irises (from a symmetry plane on the middle of iris 4). So only four irises of the total seven cavity irises are considered active field emission areas.

After particle tracking, the CST electron tracking output data is post-processed by Python to extract the impact energy of the emitted electrons and to count the number of electrons based on their impact energy. In the first step of the field emission study, 10 MV/m is considered the cavity E_{acc}. The large grain cavity quenched at this field in its first vertical test. Measurement data is available to check the simulation results.

Electron emission might occur in the different RF phases. Thus, electrons emitted from the same iris but in different RF phases will follow different emission trajectories. Electron tracking simulation is repeated with 10-degree steps in the RF phase. **Figure 6.4** and **Figure 6.5** demonstrate the simulation results for the trajectories, followed by the electrons from the active field emitting area on the irises. The active field emitting areas in **Figure 6.4** are: the right side of the first iris; the left side of the second iris; and the right side of the second iris. The active field emitting areas in **Figure 6.5** are: the left side of the third iris; the right side of the third iris; and the left side of the fourth iris. These tracking patterns are demonstrated to provide an overview of dark current originated by the cavity π mode, and to calculate its impact energy on the cavity surface. Each trajectory line illustrates an electron emitted from an active field emitter for E_{acc}=10 MV/m in the zero-degree RF phase. Secondary electron emission is omitted. It is good to use a wide emitter to obtain a general overview of the flow of the electrons, their impact energy, and their collision area. For all the cases demonstrated in **Figure 6.4** and **Figure 6.5**, the collision area for the majority of the emitted electrons is the wall of a cell where the emitter resides because the electrons are bent by the cell's magnetic field. These electrons have low impact energy. From the other side of the cavity, the accelerating axial field captures some electrons, which pass through several cells and eventually collide with the inner surface of the cavity with higher impact energy.

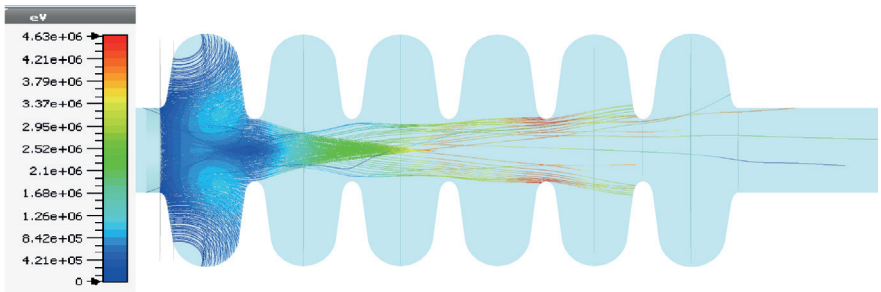

(a)

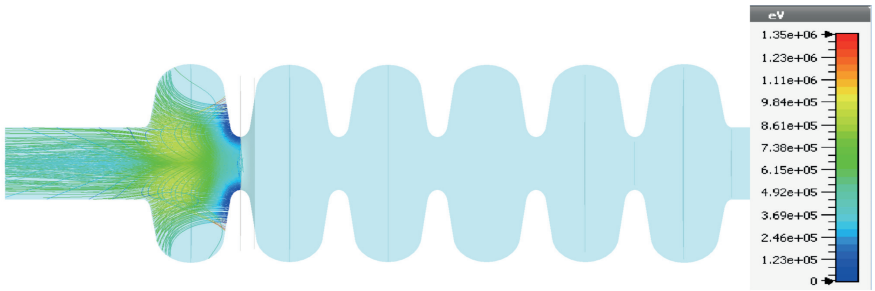

(b)

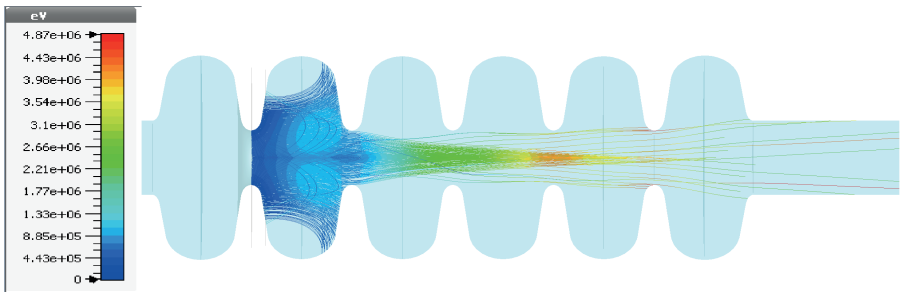

(c)

Figure 6.4. Electron tracking of the field emission for the 20 mm-wide emitter for the (a) right side of first iris, (b) left side of second iris, and (c) right side of second iris (E_{acc}= 10 MV/m, RF phase= 0 deg).

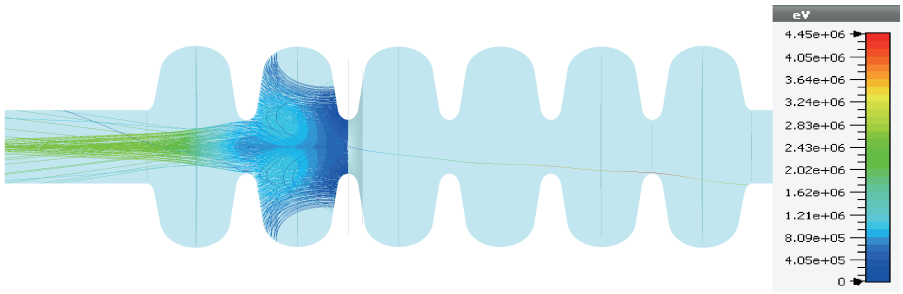

(a)

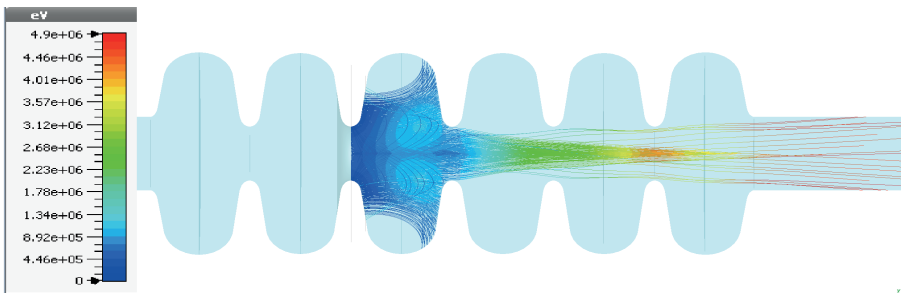

(b)

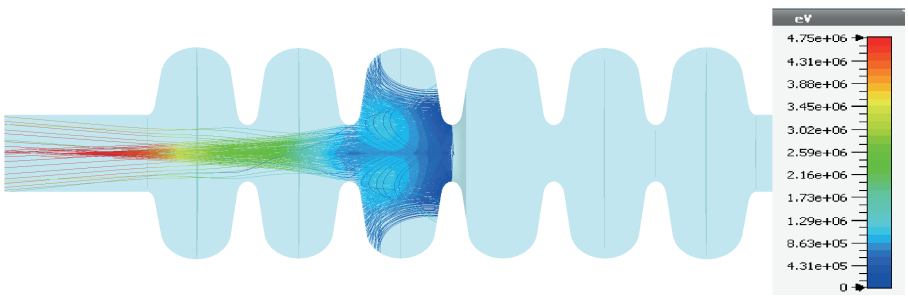

(c)

Figure 6.5. Electron tracking of the field emission for the 20 mm-wide emitter for the (a) left side of third iris, (b) right side of third iris and (c) left side of 4th iris (E_{acc}=10 MV/m 0 deg RF phase).

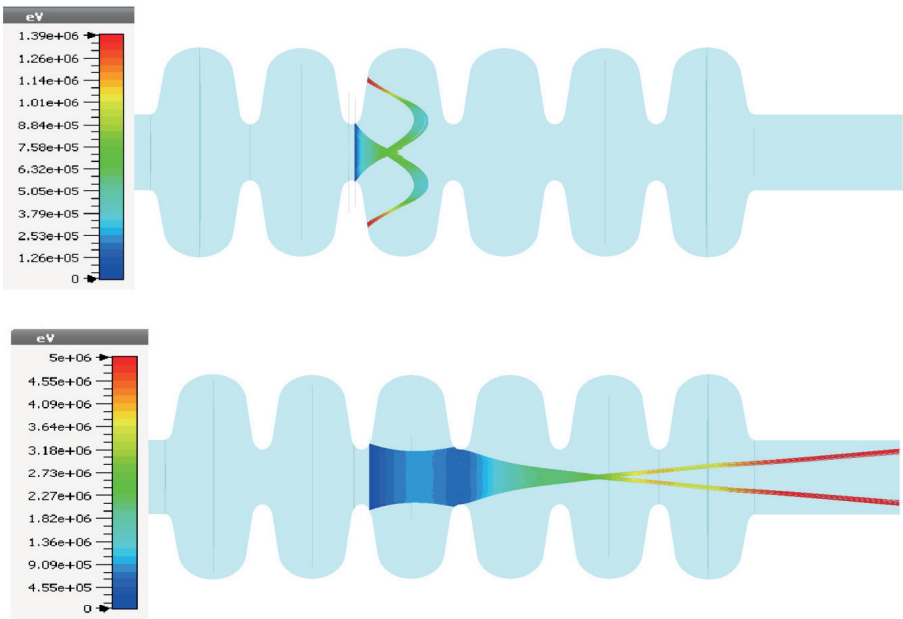

Figure 6.6. Electron tracking of the field emission for the 1 mm-wide emitter on the left side of the 4th iris for (Up), 4 mm away from the iris symmetry plane, and (Down) 10 mm away from the iris symmetry plane (E_{acc}=10 MV/m 0 deg RF phase).

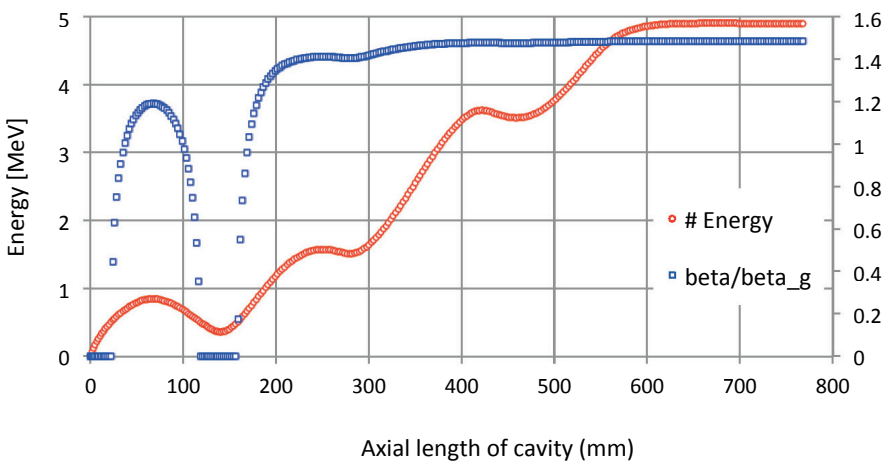

Figure 6.7. Energy gain and relative velocity change of the emitted electrons vs. axial length of the cavity

Field emitters are micron-size points. For a better view, the CST also tracks particles for the 1 mm-wide emitters on E_{acc}=10 MV/m. The 1 mm active

emitters are placed 2 mm away from each other with only one active emitter strip assessed in each electron tracking case. **Figure 6.6** shows the tracking simulation results for two emitter strips, where one of them is 4 mm and the other 10 mm away from the third iris symmetry plane. Although these emitters are on the same iris and their RF phases are similar, they have different emission angles and surface *E*-fields, which results in two different field emission patterns. The impact region for the emitted electrons from the emitter 4 mm away forms the third iris symmetry plane and is limited to the cell in which the emitter resides, whereas the electrons emitted from the other field emitter strip escape from the cell. These have been accelerated and collide at the end with the cavity beam pipe blocker.

Energy gain and relative velocity change of one of the electron trajectories illustrated in **Figure 6.6** (Down) that reaches the beam pipe blocker is illustrated in **Figure 6.7**. This is to provide a better overview of the electrons' energy gain when they pass the cavity cells. **Figure 6.7** demonstrates the energy gain of an electron up to 5 MeV, and its β/β_g change versus the axial length of the cavity. The β is the ratio of the electron velocity to the speed of light (v/c), and β_g is the cavity geometric beta. The ratio of β/β_g illustrates the synchronization between the *E*-field and electron velocity. Due to the asynchronous condition between electron velocity and the cavity (with β_g= 0.67) *E*-field, there is no linear energy gain pattern. The maximum energy gain for a particle passing several accelerating gaps is [91] and [103]:

$$\Delta W = q\, E_0\, L\, T, \tag{6.6}$$

$$E_0 = \frac{\int_0^L |E(0,z)| dz}{L}, \tag{6.7}$$

$$T = \frac{sin\,(^{\pi g}/_{\beta\lambda})}{^{\pi g}/_{\beta\lambda}}\, S(N, \frac{\beta}{\beta_g}) \tag{6.8}$$

$$S\left(N, \frac{\beta}{\beta_g}\right) = \begin{cases} (\frac{\beta}{\beta_g})^2\, \frac{(-1)^{N-1/2}}{N(\left(\frac{\beta}{\beta_g}\right)^2 - 1)}\, cos\left(\frac{\pi N}{2\frac{\beta}{\beta_g}}\right), & N\ odd \\ (\frac{\beta}{\beta_g})^2\, \frac{(-1)^{N+1/2}}{N(\left(\frac{\beta}{\beta_g}\right)^2 - 1)}\, sin\,(\frac{\pi N}{2\frac{\beta}{\beta_g}}), & N\ even \end{cases} \tag{6.9}$$

ΔW is the energy gain, q the electric charge, L the acceleration length, T the transit time factor, E_0 the average field, and S(N, β/β_g) is the reflecting number of the cavity cells and particle synchronization with the cavity geometric beta on the transit time factor. **Figure 6.8** illustrates S (N, β/β_g) change vs. β/β_g for the different number of accelerating gaps. Considering **Figure 6.6** (Down) and the relative velocity change of the electron in **Figure 6.7**, we conclude that for a cavity axial length of 300–592 mm (the last two cells of the cavity from the right) β/β_g is roughly 1.46, which corresponds to a normalized transit time factor of roughly 0.88. Thus for E_{acc}= 10 MV/m, L= 292 mm and transit time factor correction = 0.88, the energy gain will be 2.57 MeV. This value is roughly 20% less than the CST energy gain calculation for the cavity length of 300–592 mm points. The energy gain for the last two cells is due to their having an almost constant relative velocity in this boundary, which facilitates energy gain. As illustrated, there is a big change in the relative velocity for the fourth cavity cell (from the left).

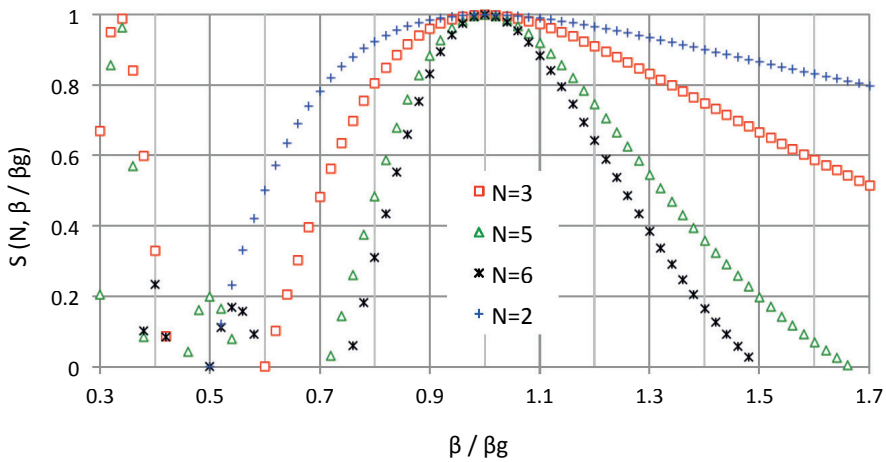

Figure 6.8. Normalized transit time factor for the different accelerating gaps vs. the normalized velocity β/β_g

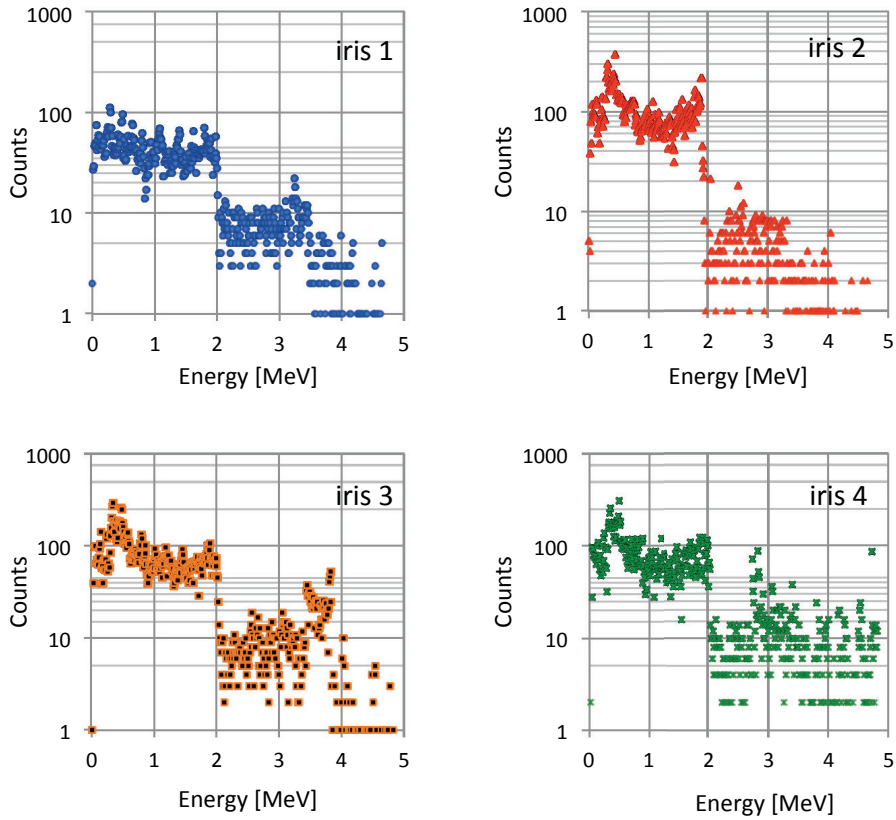

Figure 6.9. Impact energy (for irises 1, 2, 3 & 4 separately) of the emitted electrons vs. the number of electrons with the same impact energy for E_{acc}=10 MV/m (binding is done every 10 keV).

Another important characteristic related to the field emission, in addition to the maximum impact energy, is the number of electrons that reach maximum impact energy. **Figure 6.9** and **Figure 6.10** demonstrate post-processing of the CST electron tracking results by Python. In **Figure 6.9**, the impact energy spectrum versus the number of electrons with identical impact energy for irises 1, 2, 3 and 4 is presented separately. In each case, only one of these irises is considered an active field emitter. As most of the emitted electrons are trapped in the cell in which the emitter resides, the impact energy for the majority of the emitted electrons is up to 2 MeV. All the irises can be the source of field emission with an impact energy higher than 4 MeV, but the fourth iris provides a higher number of electrons with maximum impact energy due to the transit time factor effect, illustrated in **Figure 6.8**. This highlights the use of dumbbells with a better surface quality for the middle

iris of the MB cavity. **Figure 6.10** illustrates the collected effect for all four irises together.

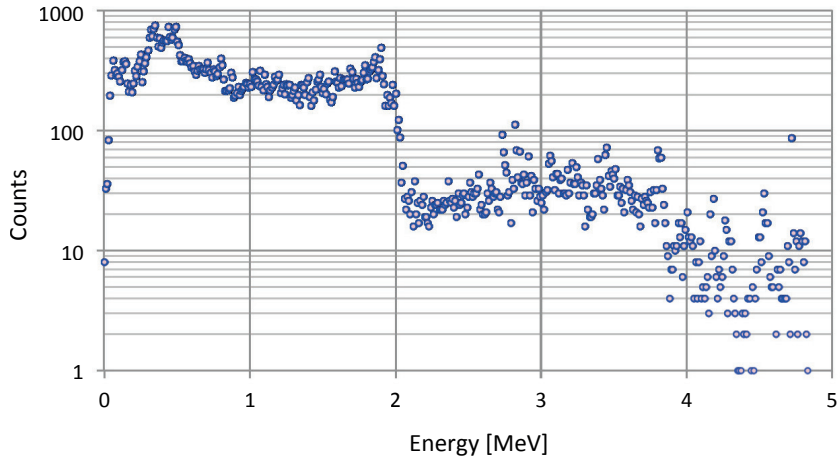

Figure 6.10. Impact energy (for irises 1, 2, 3 &4 together) of the emitted electrons vs. the number of electrons with the same impact energy for E_{acc}=10 MV/m (binding is done every 10 keV).

In a LASA vertical test, the external radiation dose is continuously measured every second by a proportional counter (Thermo Electron FH 40-G). It can measure a radiation dose up to 1 Sv/h, but for *X*-rays with energies higher than 1.3 MeV it has poor sensitivity. To measure *X*-rays generated by field emission, a NaI (Tl) scintillator detector is applied. The detector's spectra are measured every second and registered by LabVIEW. The internal radiation is measured by an array of 28 photodiodes, uniformly distributed around the cavity irises and beam tubes [100]. One of the diagnostics of field emission is X-ray detection with detectors outside of the cavity. Electrons strike an inner surface of the cavity due to Coulomb interaction with the heavy nucleus, which causes electrons to bend off and results in an emission of photons. Due to the continuous nature of a Coulomb interaction, there will be a continuous X-ray radiation spectrum. **Figure 6.11** illustrates the data collected by the scintillator before and after LG cavity processing at 10 MV/m. The data acquisition time was 60 seconds. The maximum measured *X*-ray energy for the first test is roughly 4.9 MeV, corresponding to the maximum (4.7 MeV) impact energy calculated by electron tracking. **Figure 6.11** shows an abrupt decrease in the field emission for the second RF conditioning, the effect of

cavity processing. The maximum *X*-ray measurement of 4.9 MeV is decreased to 2.5 MeV in the second RF conditioning for the same reason.

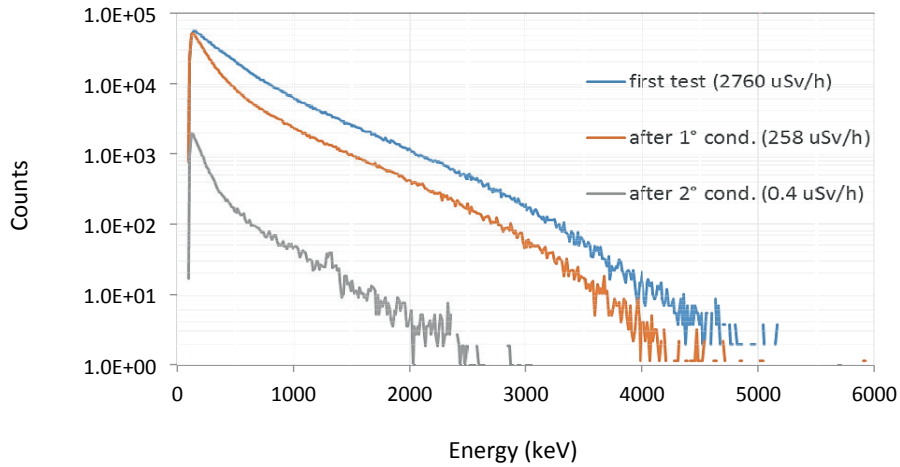

Figure 6.11. Scintillation spectra for the LG cavity at the quench field before and after conditioning for 10 MV/m E_{acc}. Acquisition time is 60 sec **[99]**.

To calculate the maximum impact energy of the field-emitted electrons in the MB cavity on its nominal E_{acc}, electron tracking for field emission is repeated for 16.7 MeV. **Figure 6.12** illustrates the calculated trajectories followed by the electrons from the four cavity irises previously mentioned. Here, 20 mm active field emitters are also considered. The maximum impact energy is increased up to 8 MeV. Electron tracking is simulated at each 10-degree RF phase (similar to the previous case). Python post-processing of the simulation results of the four aforementioned irises is summarized in **Figure 6.13** and **Figure 6.14**. In **Figure 6.13**, the impact energy spectrum versus the number of electrons with identical impact energy for irises 1, 2, 3 and 4 is presented separately. Similar to the 10 MV/m simulation case, we again see that most of the field-emitted electrons are trapped in the cell in which the active iris resides. A sudden reduction in the number of collisions counted for 3.3 MeV in **Figure 6.14** demonstrates this. Again, we note that the fourth iris provides the maximum number of electrons with high impact energy. The electrons hitting the beam pipe blocker can be transferred to the next cavity in the cryomodule plant.

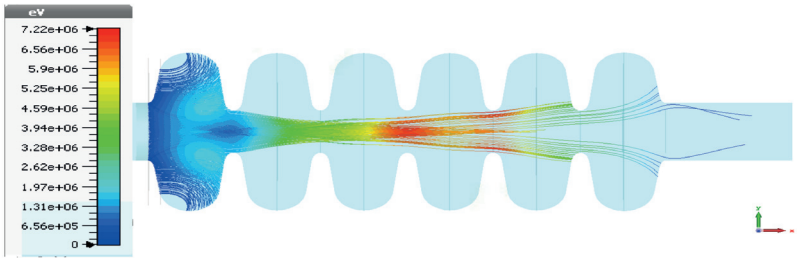

(a)

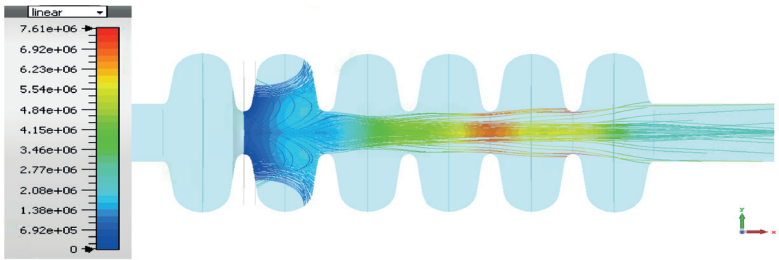

(b)

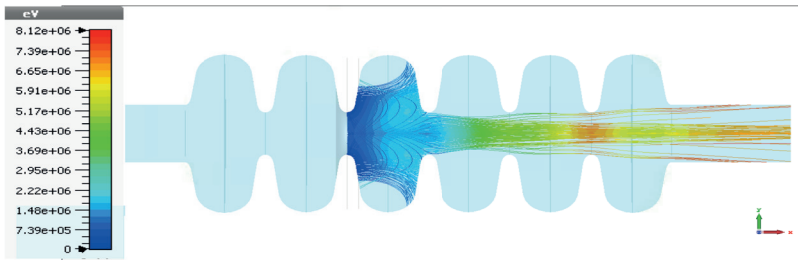

(c)

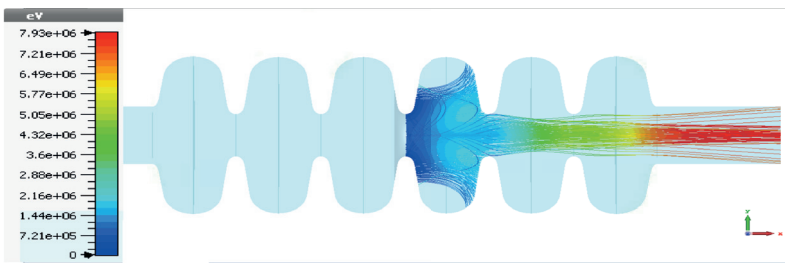

(d)

Figure 6.12. Electron tracking of the field emission for the 20 mm-wide emitter for the (a) right side of 1st iris, (b) left side of 2nd iris, (c) right side of 3rd iris, and (d) left side of 4th iris (E_{acc}=16.7 MV/m 0 deg RF phase).

Scintillator measurement results for the technical demonstration of the medium elliptical cavity cryomodule (MECCTD) in CEA-SACLAY during a MB cavity operation with E_{acc}= 16.7 MV/m, 3.6 ms RF pulse length and 14 Hz repetition rate are presented in **Figure 6.15**. The end point energy spectrum of the Bremsstrahlung spectrum is roughly 6 MeV, which corresponds with the result presented in **Figure 6.14** from post-processing the electron tracking. The field emission analysis presented by the Fishpact particle tracking code [102] for the second and fourth irises of the MB cavity, in [101], shows that most of the emitted electrons in the field will be trapped by the cell in which the emitter resides. Further, the fourth iris is more susceptible generating *X*-rays due to field emission with high impact energies. This corresponds with the study results presented in this chapter.

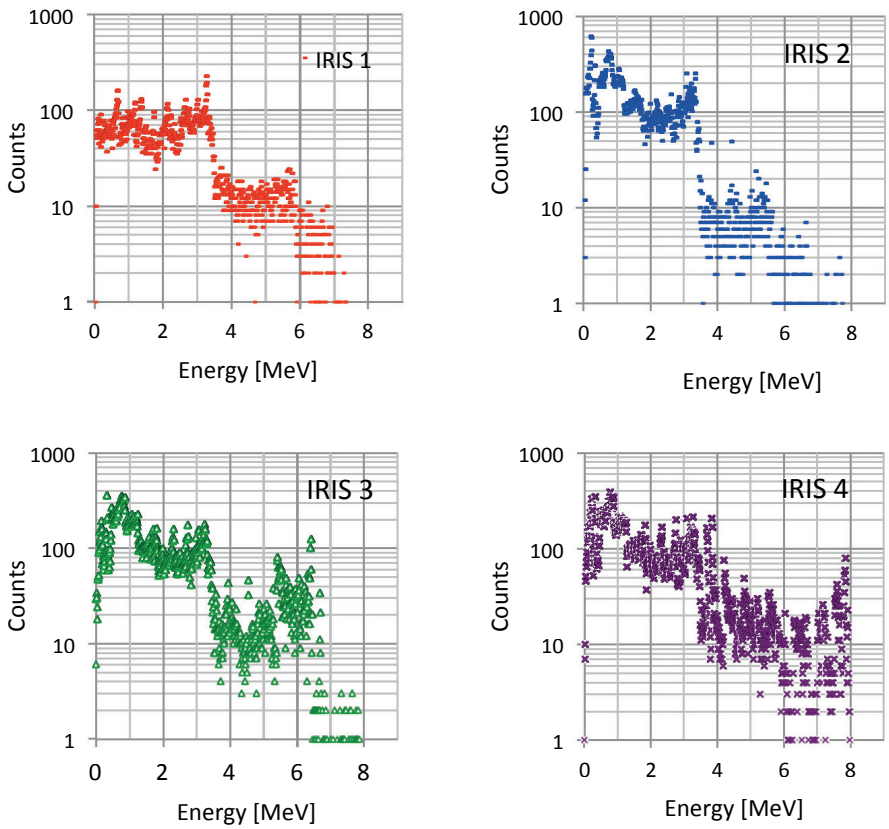

Figure 6.13. Impact energy (for irises 1, 2, 3 & 4 separately) of the emitted electrons vs. the number of electrons with the same impact energy for E_{acc}=16.7 MV/m (binding is done every 10 keV).

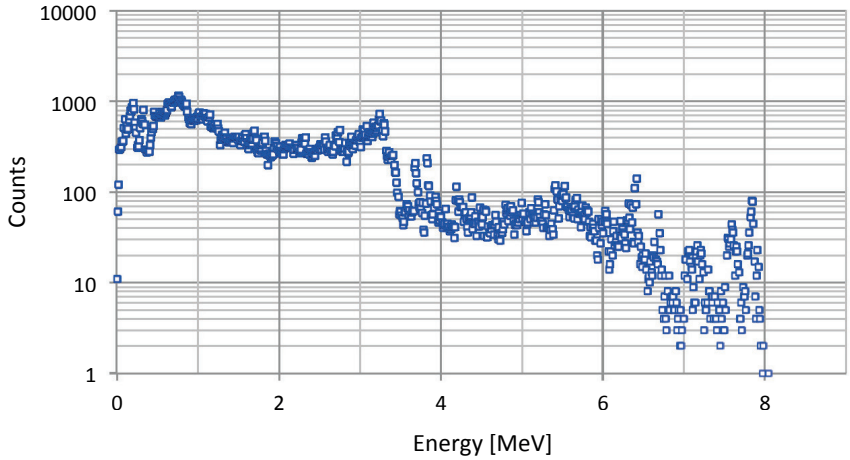

Figure 6.14. Impact energy of the emitted electrons vs. the number of electrons with the same impact energy for E_{acc}=17 MV/m. (bining is done every 10 keV).

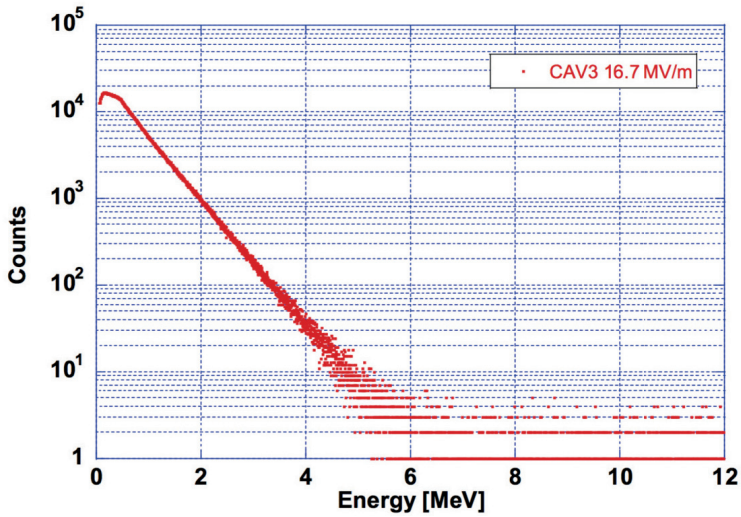

Figure 6.15. Scintillation spectra measured in CEA-SACLAY for CAV3 operation, E_{acc}= 16.7 MV/m with 3.6 ms length RF pulse and 14 Hz repetition rate **[101]**.

7 Conclusion

This thesis is a study of the ESS medium beta cavity. Work began after the basic design geometry for the cavity in INFN-LASA was completed. The main focus of the study was to resolve certain issues that arose in the basic geometry design during cavity fabrication and test procedures. The original studies, which have been conducted by the author independently or through major collaborations are: field flatness variation effect on coupler (FPC) Q_{ext}; major collaboration in the fabrication and test process of the cavity; higher order mode measurement and field emissions. The following is a brief explanation of these topics.

Field flatness variation effect on coupler (FPC) Q_{ext}

Based on the ESS specification, the Q_{ext} for the fundamental power coupler (FPC) in the medium beta cavity needs to remain within $5.9 \cdot 10^5$–$8 \cdot 10^5$. The cavity EM simulation shows that the nominal design value for the Q_{ext} is $7.8 \cdot 10^5$, close to the upper limit of specification. A systematic study was conducted to determine how mechanical errors in the cavity geometry may influence the Q_{ext} of the FPC.

In a multicell elliptical cavity, the geometrical errors in the cavity cells break the correct cell-to-cell coupling, reduce field flatness and change the Q_{ext} of the FPC. The field flatness and Q_{ext} of the FPC are correlated. Therefore, studying the changes in Q_{ext} versus field flatness variation for some typical field flatness patterns will provide an estimate of the amount of the changes in Q_{ext}. In this case, four field-flatness patterns (Figure 4.9) were chosen to demonstrate how the Q_{ext} is increased and decreased as a function of field flatness. The study shows that for two typical field flatness patterns—even with 95% field flatness—the Q_{ext} will pass the ESS upper limit and reach roughly $8.3 \cdot 10^5$. This systematic study is applicable for any multicell elliptical cavities.

Fabrication & test

As the multicell elliptical cavity is fabricated in 300 K, a 300 K geometry design is required in addition to the 2 K design. The 300 K geometry design is based on the cavity geometry changes due to thermal expansion, and changes in the dielectric coefficient of the medium (from vacuum to air) and changes in the dimension due to chemical etching. Furthermore, the evolution of the medium beta cavity geometry from half-cell to the final six-cell layout (for the frequency change and length corrections) is studied.

The methodology for the cavity RF measurement is explained and includes:

- Setting up probe antenna length by Q_{ext} measurement
- The Q_0 and E_{acc} measurement procedure for low-field pulsed operation
- The Q_0 and E_{acc} measurement procedure for CW case

Subsequently, cavity measurement results for the fine grain prototype are reported.

Following [76], [77] and [78], uncertainty in the cavity RF measurement is studied. The study considers systematic uncertainties originating from the finite directivity of the directional coupler and power reflection from the circulator. It shows 9% uncertainty in Q_0 measurement from these sources.

Higher order mode study and measurement

Passage of a charged particle through the cavity excites wakefield and is the source of the cavity higher order modes (HOM). An HOM excitation in a cavity may dilute beam quality. In an SRF cavity the HOMs could also lead to increased cryogenic heat load.

The HOM study in an accelerator facility begins with a series of bunch tracking simulations. This determines dangerous regions where HOM excitation may result in beam quality degradation. In the ESS, the bunch tracking simulation studies in [82], [83], [84] and [90] shows that:

- To prevent significant beam quality degradation, ESS SRF cavities need to have at least a 5 MHz HOM free boundary around the ESS machine lines
- A monopole HOM resonating exactly on a machine line results in beam loss

- A transverse HOM is not a problem for beam stability

The beam pipe cut-off frequency (TM_{01} mode) for the medium beta cavity is 1.69 GHz. Consequently, by examining the fifth machine line frequency, the HOM frequency spectrum for the medium beta cavity is studied up to 1.8 GHz to detect modes that may be able to stay on a machine line. The study showed that the TM_{011} mode with 1742 MHz frequency is a monopole HOM, which requires further investigation due to its proximity to the fifth machine line.

To control costs in the fabrication of the medium beta cavity there is an error budget defined, and further geometrical errors need to be prevented. Such errors may be as much as 1 mm after cavity field flatness tuning and welding of the helium tank in some dimensions. Even after field flatness corrections for geometrical errors for the acceleration mode, these errors may result in further frequency deviation of the HOMs. For instance, a 16 MHz HOM frequency shift was reported in two high beta cavity prototypes in [92].

The frequency shift caused by mechanical errors for the 1742 MHz mode is studied systematically through an error study, which estimates the effect of error in the geometrical dimensions specified in Figure 5.6 for all cavity cells. It showed that the maximum frequency deviation for this mode, given a 0.2 mm geometrical error (in all geometrical dimensions, except length), will result in a 6.3 MHz frequency deviation on the 1742 MHz HOM. Similar to the cavity fabrication process, cell length is used in this systematic error study to correct cell frequency in the accelerating mode. The proposed method is applicable to other multicell elliptical cavities for a specific HOM frequency assessment.

The HOMs of the two prototype cavities are measured to check the simulation results. As predicted in the HOM frequency spectrum section, there are enough HOM free frequency boundaries around the third and fourth machine lines. A bead-pull measurement is used to search for the TM_{011} mode with 1742 MHz (nominal frequency at 2 K and under vacuum).

Field emission

Field emission is one of the main causes in limiting the acceleration gradient in SRF cavities. An exponential increase in the field emission current is a barrier in increasing the cavity acceleration gradient. The Fowler-Nordheim study (including field enhancement factor) calculates field emission current.

The field emission current depends on the surface quality of the cavity and the surface *E*-field. Using a logical value for the field enhancement factor shows that the exponential increase in the field emission current for the medium beta cavity starts from 35 MV/m (surface *E*-field), equivalent to E_{acc}=13.7 MV/m. Moreover, the medium beta cavity measurement results show four cavities with an exponential rise in their field emission current with an E_{acc} of 14–16 MV/m.

Electron tracking simulation using CST was used to study the dynamics of the field emission in the medium beta cavity, making it possible to study the electron trajectory in the field emission and the impact energy calculation for the emitted electrons. Post-processing of the electron tracking simulation results by Python shows that a number of field emitted electrons may have different impact energies. Electron tracking was simulated for E_{acc}=10 MV/m and 16.7 MV/m due to the available measurement results of the vertical test at INFN-LASA (in 10 MV/m) for the large grain prototype cavity and the fine grain prototype cavity cryomodule test at CEA-SACLAY (in 16.7 MV/m).

In an elliptical cavity, the maximum surface *E*-field remains on the cavity irises. Therefore, only areas with fields above 70% of the surface *E*-field, located near the irises, are studied. The field emission study shows that most of the emitted electrons are trapped in the cell where the emitter resides. Only an emitted electron captured by the axial *E*-field of the cavity reaches high impact energy and produces a high *X*-ray energy. The study shows that the maximum impact energy for E_{acc}=10 MV/m and 16.7 MV/m is roughly 4.9 MeV and 8 MeV, respectively.

Appendix A

Frequency sensitivity of half-cells

Half-cells provided by deep drawing are not similar to each other and there is a spread in their 0-mode frequency measurement. Half-cell frequency sensitivity to overlength cuts in the iris and equator is calculated in Superfish. A linear dependence of the frequency shift on trimmed length is not precise enough to determine the trimming length over a large range on equator or iris extra length. Therefore, a quadratic function is used to calculate frequency sensitivity. **Figure A.1**-A.3 and Table A.1-A.3 show the frequency sensitivity results for the inner half-cell, pen half-cell and end half-cell, respectively. The formula in the last row of these tables calculates the final goal frequency after overlength trimming at the iris and equator. This formula has been verified by applying it during the MB001 cavity half-cell trimming process. Half-cells are welded through the iris, so their length is trimmed on the iris side only. In the next stage of welding, the dumbbells (or end-groups) will be welded through the equator, similar to the half-cell RF frequency checks. Length tuning before a weld is essential.

Table A.1.
inner half-cell 0 mode frequency sensitivity studies in 300 K, air with 50% humidity and before BCP

	x_{eq} (mm)	x_{iri} (mm)	Goal freq. (MHz)	Comment
Nominal	0	0	692.8	Air, 300 K before BCP
Considering overlength	+2	+0.35	689.73	Iris trimmed outside
Frequency sensitivity at x_{eq}=2, x_{iri}=0.35 (MHz/mm)	-1.55	0.46		
$f_0 = f_{meas} - \left(0.031x_{eq}^2 - 1.685x_{eq}\right) - \left(-0.02x_{ir}^2 + 0.469x_{ir}\right)$				

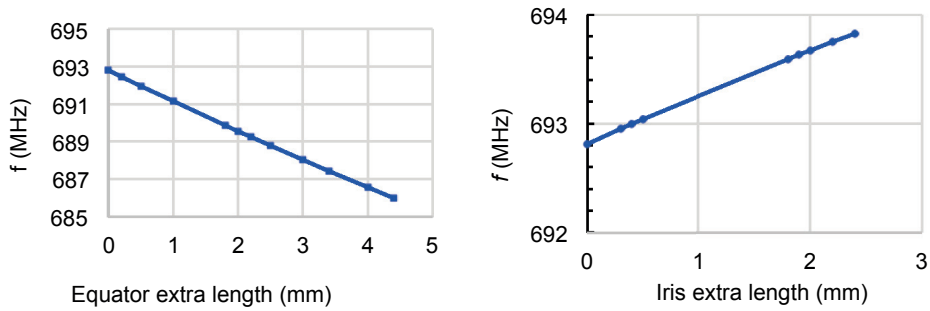

Figure A.1. Inner half-cell 0 mode frequency change vs. over length on Right: equator, Left: iris.

Table A.2.
Pen half-cell 0 mode frequency sensitivity studies in 300 K, air with 50% humidity and before BCP

	dLeq (mm)	dLiris (mm)	Goal f_0 (MHz)	Comment
Nominal	0	0	687.56	By simulation
Extra L for trimming, welding shrinkage	+2	+0.35	684.50	Iris trimmed
Freq. sens. at dLeq=2mm, dLiris=0.35 mm [MHz/mm]	-1.55	0.44		
$f_0 = f_{meas} - (0.031x_{eq}^2 - 1.673x_{eq}) - (-0.016x_{ir}^2 + 0.448x_{ir})$				

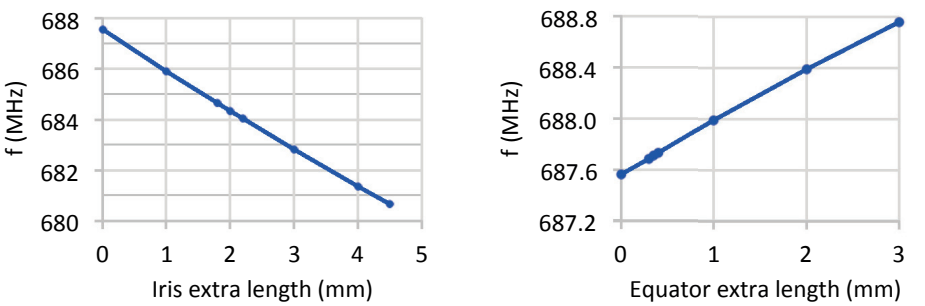

Figure A.2. Pen HC 0 mode frequency change vs. over length on Right: equator and Left: iris.

Table A.3.
End half-cell 0 mode frequency sensitivity studies in 300 K, air with 50% humidity and before BCP

	dLeq (mm)	**dLiris (mm)**	**Goal f_0 (MHz)**	**Comment**
Nominal	0	0	690.63	Air 50%, 300K
Extra L for trimming, welding shrinkage	+2.0	+0.35	687.82	Iris trimmed outside
Freq. sens. at dLeq=2mm, dLiris=0.35 mm [MHz/mm]	-1.55	1.16		
$f_0 = f_{meas} - (0.03x_{eq}^2 - 1.672x_{eq}) - 0.036x_{ir}^2 + 1.184x_{ir}$				

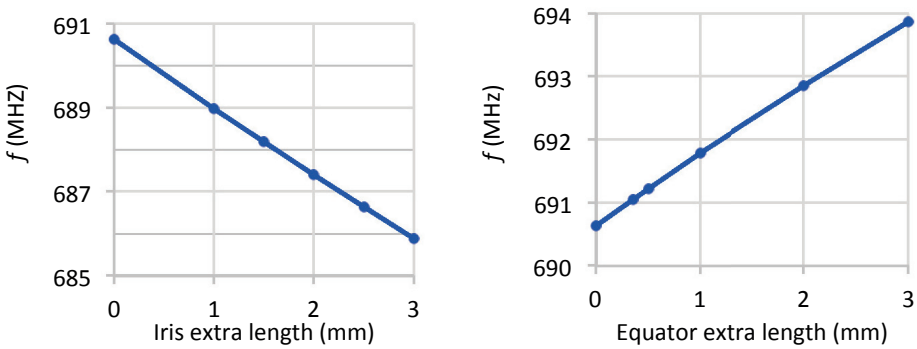

Figure A.3. End half-cell 0 mode frequency change vs. over length on Right: equator and Left: iris.

Table A.4.
Frequency sensitivity of inner dumbbell vs. side overlength calculated by Superfish

Overlength trimming in both sides of DB,	Frequency (MHz)
2+2	699.875
0.5+0.5	702.647
0+0	703.560
$y = 0.037x^2 - 1.922x + 703.57$	

Frequency sensitivity of dumbbells

Each dumbbell has 2 mm extra length on both sides. Frequency sensitivity versus overlength on the dumbbells is studied in a similar manner to that for the half-cell. Table A.4 and Table A.5 show the summary of this frequency sensitivity study for the inner dumbbell and pen dumbbell (PD and CD). They also show the π mode simulation frequency for 0, 0.5 and 2 mm overlength on both sides of the DB for the inner dumbbell and pen dumbbell, respectively. A trimming equation as a function of dumbbell length is presented in the fifth row of both tables. **Figure A.4** illustrates the frequency measurement spread for 0 mode and π mode in the dumbbells after length trimming: there are small variations from nominal frequency due to a fabrication error. This frequency error will be compensated for in the cavity field profile tuning.

Frequency sensitivity of end groups

Welding the end-HC to the coupler side beam pipe results in an EGC; there is 2.45 mm overlength in the equator side of this part. Table A.6 and **Figure A.5** present summaries of the frequency sensitivity study of the EGC by CST.

The EGC π mode simulation frequency for 0, 0.5 and 2.45 mm overlength, in addition to the trimming equation (as a function of the equator over-length), are presented. Welding the end-HC to the pickup side beam pipe results in EGT. The same procedure is applied for the EGT frequency sensitivity. Table A.7 and **Figure A.6** show the study results.

Table A.5.
Frequency sensitivity of pen dumbbells vs. side overlength calculated by Superfish

Overlength trimming in both sides of DB	Frequency (MHz)
2+2	697.8030
0.5+0.5	700.4980
0+0	701.4530
$y = 0.040x^2 - 1.903x + 701.45$	

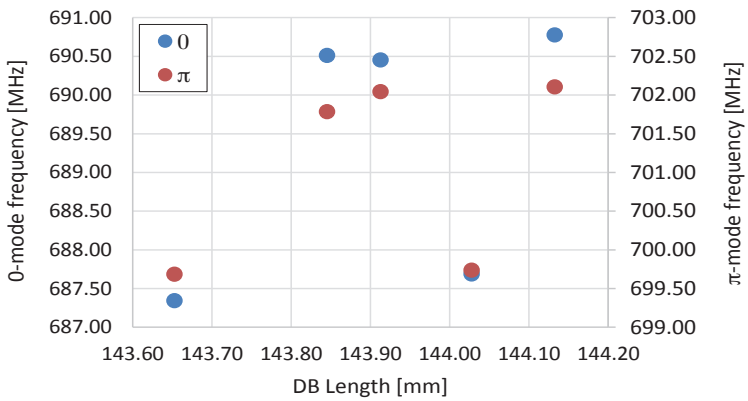

Figure A.4. Dumbbell modes frequency spectrum after trimming

Table A.6.
EGC frequency sensitivity vs. extra length calculated by CST

Extra L for trimming	Frequency (MHz)
2.45	704.0240
0.5	707.8010
0.0	708.8180
$y = 0.037x^2 - 2.049x + 708.82$	

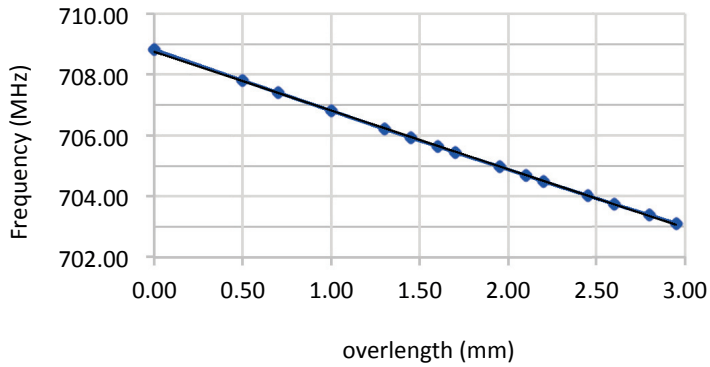

Figure A.5. EGC frequency sensitivity trend vs. side overlength calculated by CST

Table A.7.
EGT frequency vs. extra length Calculated by CST

Extra L for trimming in both sides of DB,	Frequency (MHz)
2.45	704.0140
0.50	707.7910
0.00	708.8070
$y = 0.037x^2 - 2.049x + 708.81$	

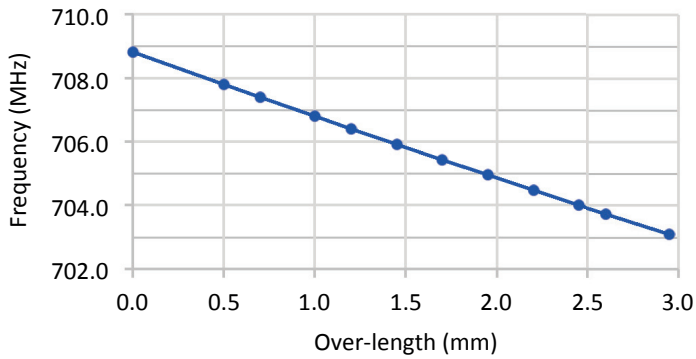

Figure A.6. EGT frequency sensitivity trend vs. side overlength calculated by CST

Appendix B

Directional coupler

A directional coupler is applied to achieve a non-disruptive measurement on forward and reflect waves along a transmission line. **Figure B.1** is a schematic view of a typical directional coupler. To characterize a directional coupler, its coupling, directivity and isolation quantities are used. These quantities are defined by:

$$C = 10\,log\frac{P_{in}}{P_{for}} = -20\,log|S_{13}|\,, \qquad \text{(B. 1)}$$

$$D = 10\,log\frac{P_{for}}{P_{ref}} = -20\,log\frac{|S_{13}|}{|S_{14}|}\,, \qquad \text{(B. 2)}$$

$$I = 10\,log\frac{P_{in}}{P_{ref}} = -20\,log|S_{14}|\,, \qquad \text{(B. 3)}$$

where C is the coupling factor, D is directivity, I is isolation, P_{in} is input power, P_{ref} is reflected power and P_{for} is forward power along the directional coupler. S_{13} is the transmission signal (S-parameter) measured between input and forward ports. Further, S_{14} is the transmission signal measured between input and reflection ports. Ideally, for power transmission in one direction (no power reflection), it is preferable to have infinite directivity and P_{ref}=0. This results in no coupling between forward and reflection ports. In practice, however, it is impossible and the directivity of a direction coupler demonstrates the level of power coupled between these two ports. Thus, forward and reflect power in a transmission line is measured by connecting two power meters to the forward and reflection ports of a directional coupler. Directivity shows the ability of a direction coupler to separate forward and reverse power waves; poor directivity will limit the accuracy of the power measurement.

This section is developed in line with [79].

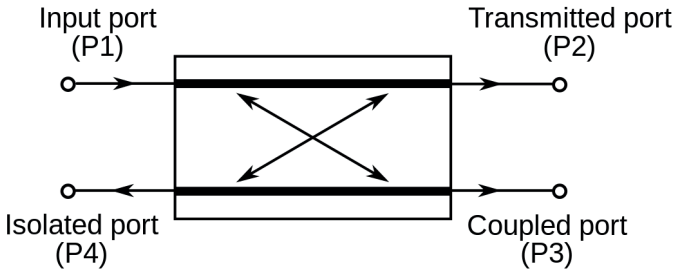

Figure B.1. Schematic view of a directional coupler

References

[1] ATLAS collaboration, “Observation of a New Particle in the Search for the Standard Model Higgs Boson with the ATLAS Detector at the LHC” Phys Lett B716, 2012, arXiv:1207.7214

[2] L. D. Lella, C. Rubbia “The Discovery of the W and Z Particles” in 60 Years of CERN Experiments and Discoveries. (World Scientific, 2015)

[3] A. Sessler and E. Wilson, ENGINES OF DISCOVERY-a Century of Particle Accelerators, World Scientific, 2007

[4] M. Ferrario, “Present and future accelerator options beyond the LHC” Ann. Phys. 528, No 1-2, 2016

[5] The International Linear Collider Technical Design Report, volume 1, Executive summary, 2013

[6] CLIC Conceptual Design Report, A Multi-TeV Linear Collider Based On Clic Technology, 2012

[7] B.T.M. Willis, C.J. Carlile, Experimental neutron scattering, Oxford University Press, 2009, ISBN 978-0-19-851970-6

[8] N. Watanabe, "Neutronics of pulsed spallation neutron sources", Rep. Prog. Phys. 66, pp. 339-381, 2003

[9] M. Lindroos, et al., Elementary Particles · Accelerators and Colliders, Landolt-Börnstein – Group, 2013, ISBN: 978-3-642-23052-3 (Print) 978-3-642-23053-0

[10] R. Garoby et al. “The European Spallation Source Design”, Phys. Scr. 93 014001, 2018

[11] H. Saugnac, et al., “The MYRRHA Spoke Cryomodule” proceeding LINAC2014, TUPP082

[12] ESS Technical Design Report, 2013, ISBN 987-91-980173-2-8

[13] ESS Conceptual Design Report, 2012

[14] R. Linander, “STATUS AND PLANS FOR THE ESS FACILITY” AccApp’17, Canada, 2017

[15] M. Vretenar, “Linear Accelerators” Proceedings of the CAS-CERN Accelerator School, 2013

[16] B. Aune et al. “The Superconducting TESLA Cavities”, Phys.Rev.ST Accel.Beams 3, 2000

[17] W. Leemans et al., “Multi-GeV Electron Beams from Capillary-Discharge-Guided Subpetawatt Laser Pulses in the Self-Trapping Regime”, Phys. Lett. 113, 2014

[18] M. Litos et al., “High-efficiency acceleration of an electron beam in a plasma wakefield accelerator”, Nature 515, 92–95, 2014

[19] R. Duperrieret al., “Frequency Jump in an Ion Linac”, PhysRev 10.084201, 2007

[20] C. Plostinar, et al., “FUTURE HIGH POWER PROTON DRIVERS FOR NEUTRINO BEAMS”, IPAC 2019

[21] L. Celona, “DESIGN ISSUES OF THE PROTON SOURCE FOR THE ESS FACILITY”, LINAC 2012

[22] L. Celona, “Microwave Discharge Ion Sources” arXiv:1411.0538 [physics], Nov. 2014, arXiv: 1411.0538.

[23] M. Eshraqi et al., “ESS LINAC BEAM PHYSICS DESIGN UPDATE”, IPAC 2016

[24] T. P. Wangler et al., “BEAM HALO IN PROTON LINAC BEAMS”, International Linac Conference, 2000

[25] R. Miyamoto et al., “BEAM PHYSICS DESIGN OF THE ESS MEDIUM ENERGY BEAM TRANSPORT”, IPAC 2014

[26] R. Miyamoto et al., “Tracking Based Courant-Snyder Parameter Matching in a Linac with a Strong Space-Charge Force”, LINAC 2016

[27] H.D. Thomsen, S.P. Moller, “The ESS HEBT Lattice Design after the 2013 Accelerator Revision”, ESS Technical Note

[28] H. Padamsee, “Design Topics for Superconducting RF Cavities and Ancillaries”, Cern Yellow Report, Cern-2014-005

[29] H. Padamsee, “50 years of success for SRF accelerators-a review”

[30] H. Alloul, Introduction to the Physics of Electrons in Solids, Springer 2011, ISBN 978-3-642-13564-4

[31] M. Vretenar, “DESIGN AND DEVELOPMENT OF RF STRUCTURES FOR LINAC4”, proceedings LINAC 2006, THP044

[32] H. Padamsee, J. Knobloch, and T. Hays, RF Superconductivity for Accelerators, Wiley & Sons, New York, ISBN 0- 471-15432-6, 1998.

[33] P. Hofmann, Solid State Physics-An Introduction, Wiley-VCH, 2015, ISBN 978-3-527-41282-2

[34] Dariusz Czerwiński, Modelling the critical parameters of high temperature superconductor devices in transient states, 2013, ISBN: 978-83-63569-50-1

[35] A. Facco, “Low- to medium-β cavities for heavy ion acceleration” Supercond. Sci. Technol. 30 (2017) 023002. http://dx.doi.org/10.1088/1361-6668/30/2/023002.

[36] S. Bousson, et al., “The ESS Spoke Cavity Cryomodules” AIP Conf. Proc. Adv. Cryogenic Eng., vol. 1573, pp. 665-672, 2014.

[37] J. R. Delayen, at al. “Design of Superconducting Spoke Cavities for High Velocity Applications” proc. PAC 2011, paper TUP100

[38] P. Duchesne, at al. “Design of the 352 MHz, Beta 0.50, Double-Spoke Cavity for ESS” proc. SRF2013, paper FRIOC01

[39] C. S. Hopper and J. R. Delayen, “Superconducting Spoke Cavities for High-Velocity Applications” Phys. Rev. Spec. Top. Accelerators Beams, 16 (2013), p. 102001. https://link.aps.org/doi/10.1103/PhysRevSTAB.16.102001

[40] N. Gandolfo, et al. “Deformation Tuner Design for a Double Spoke Cavity” proc. SRF2013, paper THP078

[41] Z. Cong, et al., “Multipacting Analysis for Half Wave Resonators in the China ADS” Chinese Physics C Vol. 39, No. 11, 2015

[42] T. Jiang, “Design and Test Result of a Superconducting Double-Spoke Cavity” Volume 51, Issue 3, June 2019, Pages 877-883, https://doi.org/10.1016/j.net.2018.12.007

[43] B. Mustapha , et al. “A Ring-Shaped Center Conductor Geometry for a Half-Wave Resonator” proc. IPAC2012, paper WEPPC037

[44] H. Podlech, et al., “The Proton Linac for the MYRRHA Project” 3rd International Workshop on Technology and Components of Accelerator-Driven Systems, 2016, Japan

[45] W. J. Schneider, et al., “Gradient Optimization for SC CW Accelerators” Proc. PAC 2003, 2863-2868 (2003)

[46] S. Posen and M. Liepe, “Nb_3Sn – Present Status and Potential as an Alternative SRF Material” Proceedings of LINAC2014, TUIOC03

[47] S. Posen and D L Hall, “Nb_3Sn Superconducting Radiofrequency Cavities: Fabrication, Results, Properties, and Prospects” Supercond. Sci. Technol. 30 033004, 2017

[48] Anne-Marie Valente-Feliciano “Superconducting RF Materials Other than Bulk Niobium: a Review” Superconductor Science and Technology, 29(11):113002, 2016.

[49] A. Miyazaki and W. V. Delsolaro, “Two Different Origins of the Q-Slope Problem in Superconducting Niobium Film Cavities for a Heavy Ion Accelerator at CERN” Phys. Rev. Accel. Beams 22, 073101, 2019

[50] S. Aull, et al., “On the Understanding of the Q-Slope of Niobium Thin Films” proceeding, SRF2015, TUBA03

[51] C. Benvenuti, et al. “Study of the Surface Resistance of Superconducting Niobium Films at 1.5 GHz”, Physica C 316, 1999

[52] S. Calatroni, “20 Years of Experience with the Nb/Cu Technology for Superconducting Cavities and Perspectives for Future Developments” Phys. C: Supercond. 441, 2006, pp. 95-101

[53] G. Bisoffi, et al. “ALPI QWR and S-RFQ Operating Experience” SRF 2007, MO404

[54] N. Jecklin, et al. “Niobium Coatings for the HIE-ISOLDE QWR Superconducting” SRF 2013, TUP073

[55] M. Transtrum, G. Catelani, and J. Sethna, “Superheating Field of Superconductors within Ginzburg-Landau Theory” Phys. Rev. B 83, 094505 (2011)

[56] S. Posen and D. L. Hall, “Nb_3Sn Superconducting Radiofrequency Cavities: Fabrication, Results, Properties and Prospects”, Supercond. Sci. Technol. 30 (2017) 033004

[57] SUPERFISH, http://laacg.lanl.gov/laacg/services/serv_codes.phtml

[58] J.F. Chen, M. Massimiliano, C. Pagani and P. Pierini, “Improvements of Buildcavity Code”. in Proc. SRF2015, pp. 1070-1072.

[59] CST Microwave Studio Solver, CST GmbH, 2018

[60] ANSYS, http://www.ansys.com, version 2016

[61] P. Pierini, D. Barni, A. Bosotti, G. Ciovati, C. Pagani , “Cavity Design Tools and Applications to the TRASCO Project”

[62] C. Pagani et al., “Design Criteria for Elliptical Cavities” Proceedings of the 10th Workshop on RF Superconductivity, 2001

[63] A. Bosotti, et al., “RF Tests of the Beta=0.5 Five Cell TRASCO Cavities” proceeding, EPAC 2004

[64] J.F. Chen, et al., “INFN-LASA Cavity Design for PIP-II LB650 Cavity ” SRF2017, Lanzhou, China

[65] G. Ciovat, et al. “Superconducting Prototype Cavities for the Spallation Neutron Source (SNS) Project” SRF 2001, Japan

[66] B. Aune et al, “Superconducting TESLA Cavities” Phys. Rev. ST Accel. Beams 3, 092001

[67] J. Sekutowicz, et al., “Low Loss Cavity for 12 GeV CEBAF Upgrade”, 2002

[68] J.F. Chen, et al., “ESS Medium and High Beta Cavity Prototypes” in Proc. IPAC2016, Korea

[69] J. Tuckmantel, “Cavity-Beam-Transmitter Interaction Formula Collection with Derivation” Tech. Rep. CERN-ATS-Note-2011-002, CERN, 2011

[70] C. Arcambal, et al., “Status of the Power Couplers for the ESS Elliptical Cavity Prototypes” proceeding, SRF2015, THPB078

[71] Cern Accelerator School, April 1991.

[72] A. Bosotti, et al., “RF Tests of the Beta=0.5 Five Cell TRASCO Cavities” EPAC, Switzerland, 2004

[73] H.J. Hucek, K.E. Wilkes, K.R. Hanby and J.K. Thompson, Handbook on material for superconducting machinery, January 1977

[74] L.C. Maier and J.C. Slater, “Field Strength Measurements in Resonant Cavities”, Journal of Applied Physics, vol. 23, Nr. 1, 1952, pp.68-77

[75] H. Padamsee, RF Superonductivity: Science, Technology and Applications, 2008.

[76] T. Powers, “Theory and Practice of Cavity RF Test Systems” IAEA-INIS 28.01, 2006

[77] O. Melnychuk, A. Grassellino, and A. Romanenko, “Error Analysis for Intrinsic Quality Factor Measurement in Superconducting Radio Frequency Resonators” Rev. Sci. Instrum. 85, 124705, 2014

[78] J. Holzbauer, et al., “Systematic Uncertainties in RF-Based Measurement of Superconducting Cavity Quality Factors”, Nucl. Instrum. Methods Phys. Res. A Accel. Spectrom. Detect. Assoc. Equip., vol. 830, no. 9, pp. 22-29, Sep. 2016

[79] D. M. Pozar, Microwave Engineering, Wiley & Sons, ISBN 978-0-470-63155-3, 2011

[80] P. R. Bevington, D. K. Robinson, “Data Reduction and Error Analysis for Physical Sciences”, 3rd ed., McGrw-Hill, 2002, ISBN 0-07-119926-8

[81] M. Bertucci et al. “Upgrade on the Experimental Activities for ESS at the LASA Vertical Test Facility” SRF2019, Dresden, Germany

[82] A.Farricker, R.M.Jonesa, S.Molloy “Beam Dynamics in the ESS Linac Under the Influence of Monopole and Dipole HOMs” Physics Procedia, Volume 79, 2015

[83] R. Ainsworth and S. Molloy “The Influence of Parasitic Modes on Beam Dynamics for the European Spallation Source Linac” Nuclear Instruments and Methods in Physics Research A, vol. 734, pp. 95

[84] A. Farricker “Higher Order Modes and Beam Dynamics at The European Spallation Source” thesis, 2017

[85] Sang-ho Kim, I. E. Campisi, D. Jeon, F. Casagrande, D. Stout, Y. Kang, M. Crofford, M. McCarthy and M. Champion “Study on Fault Scenarios of Coaxial Type HOM Couplers in SRF Cavities” Proceedings of LINAC 2006

[86] S. Kim, M. Doleans, D. Jeon and R. Sundelin “Higher-Order-Mode (HOM) Power in Elliptical Superconducting Cavities for Intense Pulsed Proton Accelerators” Nuclear Instruments and Methods in Physics Research A 492, 2002

[87] M. Schuh, Study of Higher Order Modes in Superconducting Accelerating Structures for Linac Applications, CERN-THESIS-2011-156-22/06/2011

[88] Superfish, https://laacg.lanl.gov/laacg/services/download_sf.phtml

[89] P. Michelato et al., “ESS Medium and High Beta Cavity Prototypes,” in Proc. IPAC2016, Korea, paper WEPMB011

[90] A. Farricker et al., “Implications of Manufacturing Errors on Higher Order Modes and on Beam Dynamics in the ESS LINAC,” in Proc. IPAC 2015

[91] T. P. Wangler, RF Linear Accelerators, Wiley-VCH, 1998

[92] A. Farricker, R.M. Jones and N.Y. Joshi and S. Molloy “Implications of Resonantly Driven Higher Order Modes on the ESS Beam” in Proc. IPAC 2016

[93] S. Molloy "An Empirical Study of HOM Frequencies", ESS-DOCDB, 2011

[94] D. Sertore, et al., “Experience on Design, Fabrication and Testing of a Large Grain ESS Medium Beta Prototype Cavity,” in Proc. IPAC, 2017, Denmark.

[95] The PIP-II Conceptual Design Report, 2017

[96] C. Pagani, et al., “Status of the PIP-II Activities at INFN-LASA” in Proc. IPAC 2019, ISBN: 978-3-95450-208-0

[97] A. Bosotti, et al. “Vertical Tests of ESS Medium Beta Prototype Cavities at LASA” IPAC 2017, Copenhagen, Denmark, MOPVA063

[98] D. Sertore, et al. “ESS Medium Beta Activity at INFN LASA” SRF 2019, Dresden, Germany

[99] M. Bertucci, et al., “Experience on Design, Fabrication and Testing of a Large Grain ESS Medium Beta Prototype Cavity” SRF 2017, China

[100] M. Bertucci et al. “Upgrade on the Experimental Activities for ESS at the LASA Vertical Test Facility” SRF2019, Dresden, Germany

[101] E. Cenni et al. “Field Emission Studies on ESS Elliptical Prototype Cavities at CEA Saclay” SRF2019, Dresden, Germany

[102] G. Wu, https://code.google.com/archive/p/fishpact/

[103] A. Kumar, A. R. Jana, and V. Kumar, “A Study of Dynamic Lorentz Force Detuning of 650 MHz βg = 0.9 Superconducting Radio Frequency Cavity” Nucl. Instrum. Methods Phys. Res. A, Accel. Spectrom. Detect. Assoc. Equip., vol. 750, pp. 69–77, Jun. 2014

[104] D. Sertore, et al. “INFN-LASA Medium Beta Cavity Prototypes for ESS Linac” proceeding SRF2017, TUPB048